이학박사 학위논문

First-principles study of the defect-related electronic structure and properties in the honeycomb lattice systems

벌집모양격자계 내의 결함에 관한 전자구조와 전기적 성질에 관한 제일원리연구

2013년 8월

서울대학교 대학원

물리천문학부

김 영 국

First-principles study of the defect-related electronic structure and properties in the honeycomb lattice systems

벌집모양격자계 내의 결함에 관한 전자구조와 전기적 성질에 관한 제일원리연구

지도교수 임지순

이 논문을 이학박사 학위논문으로 제출함.

2013년 4월

서울대학교 대학원

물리천문학부

김 영 국

김영국의 이학박사 학위논문을 인준함.

2013년 6월

위 원 장 유 재 준 (인)

부위원장 임 지 순 (인)

위 원 최 석 봉 (인)

위 원 박 철 환 (인)

위 원 유 병 덕 (인)

First-principles study of the defect-related electronic structure and properties in the honeycomb lattice systems

Youngkuk Kim

Supervised by

Professor **Jisoon Ihm**

A Dissertation

Submitted to the Faculty of

Seoul National University

in Partial Fulfillment of

the Requirements for the Degree of

Doctor of Philosophy

August 2013

Department of Physics and Astronomy

Graduate School

Seoul National University

Abstract

The last decade has witnessed a tremendous growth in our understanding on electronic properties of honeycomb lattice systems such as carbon nanotubes and graphene. There have been enormous efforts to explore their unique properties and apply them to practical devices. Throughout the unprecedented efforts, it is now considered that they are among the most promising materials for future electronic technology. Considering the precedent progress in the related studies, it is surprising that these systems keep attracting us by revealing unexpected phenomena based on them. Especially when they have crystalline defects, they exhibit more interesting features. Their properties may be significantly affected by the presence of defects, and as a consequence, new phenomena unexpected in pristine systems may emerge. This allows new opportunities for the occurrence rich physical phenomena based on the materials, leading to the extension of the scope of applications of these systems. In this thesis, we present first-principles calculations and analysis for the defect-induced electronic structure and properties in honeycomb lattice systems including carbon nanotube (CNT), graphene, and silicene.

First, after briefly reviewing on the basic electronic properties of graphene and silicene based on a tight-binding analysis as well as computational methods for this

study, we explore transport properties of a metallic carbon nanotube with a Stone-Wales defect. Using first-principles transport calculations based on scattering-state approach methods [1], we show that the introduction of a Stone-Wales defect can give rise to loop currents in its vicinity. The behavior of the loop currents as a function of Fermi energy is investigated, and it is shown that (1) the intensity of the current density shows the maximum at the energy where the conductance becomes $1.5G_0$, (2) its intensity vanishes at conductance dip centers, and (3) the direction of the loop current is reversed as the Fermi energy crosses the dip centers. The origin of these newly found behaviors is discussed, and it is shown that it is a general consequence of the interference between a conducting channel and a defect state. We also consider an experimental signature of the loop current by calculating induced magnetic fields. We expect a dipole field can be generated which can be temporally oscillating via time-modulating gate voltages.

Next, we consider the influence of electronic structures on the atomic structure of graphene with a divacancy. A divacancy is one of the most abundant defects in graphene characterized by various reconstructed structural forms such as triple pentagons-triple heptagon (555-777) and pentagon-octagon-pentagon (5-8-5). From the transmission electron microscope (TEM) images published in Ref. [2] we observed that a divacancy transforms from one reconstructed structure to another reconstructed structure under the electron beams of 80 keV kinetic energy. Motivated by the observation, we have calculated electronic structures of a divacancy in its diverse reconstructed forms based on density functional theory (DFT). Our calculations show that the energy barrier needed to overcome to make transformation from one structure into another is within the range of the maximum kinetic energy

transferred from electron beams to carbon atoms. They also suggest that it is energetically favorable for the microscopic processes of the structural transformations to be consist of a series of Stone-Wales type transformations. Our findings predict that a pentagon-heptagon-heptagon-pentagon (5-7-7-5) defect should appear as an intermediate state playing a role to lower the energy barriers for the structural transformations.

Finally, we consider silicene with a line defect. Silicene is a two-dimensional honeycomb lattice made of silicon atoms. Unlike graphene, silicene is unstable in a planar geometry, and the instability is lifted via buckling. This buckling spontaneously breaks the reflection symmetry with respect to the silicene plane, due to which the ground structure of silicene has doubly degenerate ground states. The last topic of this thesis is the first-principles study on the electronic structure of this interface geometry between these two ground structures. It is shown that the interface geometry gives rise to topologically protected zero modes under an electric field applied perpendicular direction to the plane. We discuss topological origin of the zero mode in the context of the quantum valley Hall effects based on the Berry curvature calculations. We also discuss potential experiments to observe the emergence of the zero modes based on scanning tunneling microscopy experiments simulated via first-principles calculations. Our results may help guide the efforts to observe topological phenomena in silicene.

Keywords : density functional theory, carbon nanotubes, graphene, silicene, loop currents, magnetic dipoles, transprot, Stone-Wales defect, quantum interference, divacancy, structural transformation, Stone-Wales transformation, transmission elec-

tron microscopy, quantum valley Hall effect, valley Hall conductivity, soliton, topological domain wall, zero mode, scanning tunneling microscopy

Student Number : 2006-22901

Contents

List of Acronyms

DFT density functional theory

LDA local density approximation

QMC quantum Monte Carlo

PAW projected augmented wave

GGA generalized gradient approximation

PBE Perdew-Burke-Erenzerhof

PAO pseudo-atomic orbital

LCAO linear combination of atomic orbitals

TI topological insulator

CNT carbon nanotube

SSW symmetric Stone-Wales defect

555-777 triple pentagon-triple heptagon

5-8-5 pentagon-octagon-pentagon

5-7-7-5 pentagon-heptagon-heptagon-pentagon

DV divacancy

TEM transmission electron microscopy

MV monovacancy

SW Stone-Wales

QSH quantum spin Hall

QVH quantum valley Hall

DW domain wall

1D one-dimensional

2D two-dimensional

STM scanning tunneling microscopy

BZ Brillouin zone

LB low buckling

OP order parameter

List of Figures

List of Tables

CHAPTER 1

Introduction

A crystalline defect is generally referred as any region where the microscopic arrangement of ions differs significantly from that of a pristine crystal [4]. A real materials usually has a huge number of defects in a great variety. Electrons in a defected system see these imperfections as new boundaries, and their behaviors may be completely different from those of a pristine system. Therefore, it is of crucial importance to investigate how these imperfections can influence the behaviors of electrons thus changing the electronic properties of the crystals.

Among many other crystals, honeycomb lattice systems such as CNT [5] and graphene [6, 7, 8] have been of exceptional importance. They have shown fascinating and unique properties attracting enormous attentions with immense potential for the applications in future electronic industries. For instance, CNT is considered as a truly nanoscale wire with various quantum effects such as the Aharonov-Bohm effect [9], the quantization of conductance [10], and the application to single effect transistor [11]. Now they are in the stage of application in industry with possible

practical uses in field emission display, micro-electronic devices, battery, and bio-chemical applications [12, 13, 14, 15, 16]. The situation of graphene is similar. Since the first synthesis of graphene [6, 7, 8], graphene has attracted tremendous attention due to its unique properties such as ultrahigh electron mobility [17, 18, 19], high thermal conductivity [20], and extreme mechanical properties [21]. Now it is considered as one of the most promising materials for future electronic devices. More recently, there has been growing interest in the silicon-version of graphene, which is called silicene. Silicene is a two-dimensional (2D) honeycomb lattice made of silicon atoms. Currently, there have been many experimental efforts to synthesis this new honeycomb lattice system, yet it has only been realized on metal and semiconductor surfaces [22, 23, 24, 25, 26] with a severe deterioration of electronic structures due to the interaction with the substrates as well as reconstructions [27]. Despite the current experimental situation, there have been many theoretical efforts to investigate the electronic properties of silicene, and it is expected that it should support many interesting phenomena unexpected in graphene [28, 29, 30, 31].

In this thesis, we present a first-principles study of the defect-related electronic structure and properties of CNTs, graphene, and silicene. For the purpose, we first briefly introduce the basic electronic structure of graphene and silicene based on tight-binding analysis followed by the discussion on the zero gap band structure based on the point group symmetries such as inversion, time-reversal, and C_3 symmetries in Chapter 2. Then we move to the brief review on computational methods which we have employed in our study in Chapter 3. It includes the essence of the density functional theory and modern first-principles computational schemes such as exchange correlation approximation, pseudopotentials, and basis sets. This Chapter

also include the first-principles methods to calculate conductance of nanomaterials based on scattering-states approach [1], and numerical methods to calculate the Berry curvature and Hall conductivity on numerical grids of BZ [32].

In Chapter 4, we consider a Stone-Wales defect embedded in a metallic CNT. Using a state-of-art first-principles scattering-state method, we present that the introduction of a Stone-Wales defect into a metallic CNT can give rise to loop currents in the vicinity of the defect. The behavior of the loop currents under different Fermi energies is investigated, and it is shown that (1) the current density shows the maximum intensity at the energy where the conductance becomes $1.5G_0$, (2) its intensity vanishes at dip centers, and (3) the direction of the loop current is reversed as the Fermi energy crosses the dip centers. We also show that the origin of these behaviors can be attributed to the interference between a metallic channel and a defect state. Then we suggest a potential experimental signature of the loop currents by calculating induced magnetic fields. Our finding suggests that an oscillating dipole-like magnetic field should be generated when one applies a time-modulating gate voltage to the system.

In Chapter 5, we move to graphene hosting a divacancy. A divacancy is a dimer vacancy, which is one of the most abundant defects in graphene having various reconstructed structural forms such as triple pentagons-triple heptagon (555-777) and pentagon-octagon-pentagon (5-8-5). From the transmission electron microscope (TEM) images published in Ref. [2] we found that a divacancy transforms from one reconstructed structure to another reconstructed structure under the electron beams of 80 keV kinetic energy. Motivated by the experiment, we have calculated electronic structures of graphene with a divacancy in different reconstructed forms, and our

calculations show that the kinetic energy of carbon atoms needed to make transformation from one structure to another is within the range of maximum kinetic energy transferred from electron beams to carbon atoms. Our calculations indicate that it is highly likely that the microscopic processes for the structural transformations should be consist of a series of Stone-Wales type transformations. Also they reveal that a pentagon-heptagon-heptagon-pentagon (5-7-7-5) defect should appear during the structural transformations as an intermediate structural state and plays an important role by lowering the energy barriers of the structural transformations.

In Chapter 6, we consider silicene hosting a line defect. Unlike graphene, silicene is expected to be stable only in its low-bucked geometry, due to which diverse phenomena avoided in graphene are likely to appear in silicene. For example, buckling spontaneously breaks the reflection symmetry with respect to the silicene plane and gives rise to two-doubly degenerate structural ground states. Here we consider the interface connecting these two ground structures and show that it supports (**!** ((**!**)1D) conducting states along the interface when one applies an electric field in the perpendicular direction to the plane. The origin of the conducting states can be attributed to topologically protected zero modes. We discuss topological nature of these conducting states in the context of quantum valley Hall (QVH) effects based on the numerical calculations of the Berry curvatures and the valley-specific Hall conductivities. We also discuss the experimental signature of the emergence of topologically protected conducting states along the domain wall based on the simulated scanning tunneling microscopy images. Our results may help guide the experimental efforts to observe topological domain walls based on silicene.

Finally, all the results are summarized in Chapter 7.

CHAPTER 2

Basic properties of graphene and silicene

Electrons in graphene near the neutrality point behave like massless chiral fermions exhibiting linear dispersion relations. Diverse electronic properties are largely originated from this fact. In this Chapter, we present basic electronic properties of graphene and silicene by deriving the band structure based on tight-binding analysis. We also present point group symmetry anlaysis on the band structure to understand the origin of the robustness of the Fermi point at the corner of BZ.

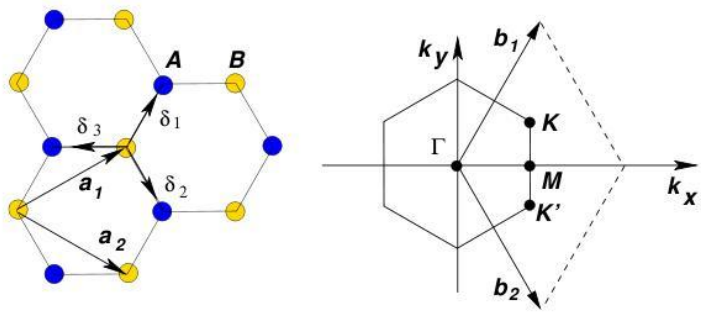

Figure 2.1: The atomic geometry of graphene (left) and the reciprocal lattice space (right) with the first BZ of graphene indicated by solid hexagon. The lattice structure of graphene are shown in the left. $\vec{a}_1$ and $\vec{a}_2$ are the primitive vectors that defines Wigner-Seitz unit cell. In the unit cell, there are two basis carbon atoms indicated as two different colors. The first BZ of associated reciprocal lattice vector are shown in the right. Points of high symmetry Γ, M, and K are indicated together.

2.1 Tight-binding description of the electronic structure of graphene

2.1.1 Preliminaries

Graphene is a two-dimensional (2D) honeycomb lattice made of carbon atoms. As illustrated in in Fig. 2.1, the unit cell of the material has a basis of two atoms, which are denoted by A and B, respectively. The primitive lattice vectors of graphene can be denoted

$$\mathbf{a_1} = \sqrt{3}a\left(\frac{\sqrt{3}}{2}, \frac{1}{2}\right), \quad \mathbf{a_2} = \sqrt{3}a\left(\frac{\sqrt{3}}{2}, \frac{-1}{2}\right),$$

where $a \approx 1.42$ Å is the distance between two neighboring carbon atoms. The three vectors connecting nearest neighbor carbon atoms are

$$\boldsymbol{\tau}_1 = a\left(\frac{1}{2}, \frac{\sqrt{3}}{2}\right), \quad \boldsymbol{\tau}_2 = a\left(\frac{1}{2}, -\frac{\sqrt{3}}{2}\right), \quad \boldsymbol{\tau}_3 = -a\,(1, 0)\,. \tag{2.1}$$

The corresponding reciprocal lattice vectors are

$$\mathbf{b_1} = \frac{4\pi}{3a}\left(\frac{1}{2}, \frac{\sqrt{3}}{2}\right), \quad \mathbf{b_2} = \frac{4\pi}{3a}\left(\frac{1}{2}, -\frac{\sqrt{3}}{2}\right).$$

Two inequivalent points at the zone corners of the 1st BZ are

$$\mathbf{K} = \left(\frac{2\pi}{3a}, \frac{2\pi}{3\sqrt{3}a}\right), \quad \mathbf{K'} = \left(\frac{2\pi}{3a}, -\frac{2\pi}{3\sqrt{3}a}\right).$$

These two inequivalent zone corners, K and K', are of particular importance because they host Dirac bands near the Fermi energy which determine the low-energy electronic properties as well as transport properties of the system. One unit cell has two atoms, each of which atom provides p_z a conducting channel, thus forming two bands near the Fermi level for a given K-point. The upper band and lower band near the Fermi level are as shown in Fig. 2.2. These bands touch each other at the six corners of BZ, and these points will be referred as the Dirac points. Note that due to the translational symmetry, all the other Zone corners are equivalent to either one of K or K' point. Also note that the two p_z orbital provides two electrons per unit cell which fill the lower band (the valance band), thus making the upper band empty (the conduction band). As a consequence, the Dirac points become the Fermi point determining the low-energy electronic and transport properties of graphene.

2.1.2 Tight-binding analysis

The tight-binding model of graphene is constructed on a pair of p_z orbitals originated from two carbon atoms forming a unitcell, $\chi_m(\mathbf{r} - \mathbf{R}_m)$, serves as a basis for the low-energy effective Hamiltonian of graphene. Here, $\chi_m(\mathbf{r} - \mathbf{R}_m)$ are atomic orbitals having its origin being at $\mathbf{R}_m$, where $m = A$ or B, $\mathbf{R}_A = n_1\mathbf{a_1} + n_2\mathbf{a_2}$, and $\mathbf{R}_B =$

$n_1\mathbf{a_1}+n_2\mathbf{a_2}-\boldsymbol{\tau}_3$ with integer n_1 and n_2. The Bloch theorem for atomic wavefunction $\chi_{m\mathbf{k}}$ requires to be

$$\chi_{m\mathbf{k}}(\mathbf{r}) = \sum_{\mathbf{R}_m} e^{i\mathbf{k}\cdot\mathbf{R}_m}\chi_m(\mathbf{r}-\mathbf{R}_m).$$

Since the Hamiltonian preserves $\mathbf{k}$ in BZ, an energy eigenfunction can be labeled as $\psi_{\mathbf{k}}(\mathbf{r})$. Within the tight-binding approach, we expect that the eigenfunction can be expressed as the linear combination of atomic wave functions:

$$\psi_{\mathbf{k}}(\mathbf{r}) = \sum_{m=\{A,B\}} c_m(\mathbf{k})\chi_{m\mathbf{k}}(\mathbf{r}),$$

and the secular equations for wavevector $\mathbf{k}$ becomes

$$\sum_{m'}[H_{mm'}(\mathbf{k}) - \epsilon(\mathbf{k})S_{mm'}(\mathbf{k})]c_{m'}(\mathbf{k}) = 0. \tag{2.2}$$

Here $H_{mm'}$ and $S_{mm'}$ are the matrix elements of the Hamiltonian and the overlap matrix of atomic orbitals respectively, which can be written as

$$H_{mm'}(\mathbf{k}) = \int d\mathbf{r}\chi^*_{m\mathbf{k}}(\mathbf{r})\hat{H}\chi_{m'\mathbf{k}}(\mathbf{r}) = \sum_{\mathbf{R}_m-\mathbf{R}_{m'}} e^{i\mathbf{k}\cdot(\mathbf{R}_{m'}-\mathbf{R}_m)}H(\mathbf{R}_{m'},\mathbf{R}_m),$$

and

$$S_{mm'}(\mathbf{k}) = \int d\mathbf{r}\chi^*_{m\mathbf{k}}(\mathbf{r})\chi_{m'\mathbf{k}}(\mathbf{r}) = \sum_{\mathbf{R}_m-\mathbf{R}_{m'}} e^{i\mathbf{k}\cdot(\mathbf{R}_{m'}-\mathbf{R}_m)}S(\mathbf{R}_{m'},\mathbf{R}_m),$$

with

$$H(\mathbf{R}_{m'},\mathbf{R}_m) \equiv \int d\mathbf{r}\chi^*_m(\mathbf{r}-\mathbf{R}_m)\hat{H}\chi_{m'}(\mathbf{r}-\mathbf{R}_{m'}),$$

and

$$S(\mathbf{R}_{m'},\mathbf{R}_m) \equiv \int d\mathbf{r}\chi^*_m(\mathbf{r}-\mathbf{R}_m)\chi_{m'}(\mathbf{r}-\mathbf{R}_{m'}).$$

For simplicity of the model tight-binding Hamiltonian, we consider only the electron hopping parameters between the nearest neighboring carbon atoms, and

set the on-site energy be zero, i.e.

$$H(\mathbf{R}_{m'}, \mathbf{R}_m) = \begin{cases} t & \text{for } \mathbf{R}_m - \mathbf{R}_{m'} = \boldsymbol{\tau}_i, (i = 1, 2, 3) \\ 0 & \text{otherwise} \end{cases},$$

where t is the nearest neighbor hopping energy. It is a plausible assumption since p_z orbitals of carbon atoms are more or less localized near the host atom, so that the overlap between the orbital wavefunctions from the next neighboring atoms should be negligible. In this case, the overlap matrix becomes an identity matrix, and the secular equation (2.2) reads to

$$\begin{vmatrix} -\epsilon(\mathbf{k}) & H_{AB}(\mathbf{k}) \\ H^*_{AB}(\mathbf{k}) & -\epsilon(\mathbf{k}) \end{vmatrix} = 0,$$

where

$$H_{AB} = t \sum_{i=1}^{3} \exp(i\mathbf{k} \cdot \boldsymbol{\tau}_\mathbf{i}) \tag{2.3}$$

$$= t \left[e^{-iak_x} + 2e^{i\frac{a}{2}k_x} \cos\left(\frac{\sqrt{3}}{2}k_y\right) \right]. \tag{2.4}$$

This equation gives the energy bands of the graphene:

$$E_\pm(\mathbf{k}) = \pm t \left[3 + 2\cos(\sqrt{3}k_y a) + 4\cos\left(\frac{\sqrt{3}}{2}k_y a\right) \cos\left(\frac{3}{2}k_x a\right) \right]^{1/2}, \tag{2.5}$$

where the plus sign applies to the upper(π^*) and the minus sign the lower(π) band. The spectrum for the band (2.5) is shown in Fig. 2.2.

It deserves more attention to the points near the Dirac points, $\mathbf{K}$ and $\mathbf{K}'$. We expand (2.5) as $\mathbf{k} = \mathbf{K} + \mathbf{q}$, with $|\mathbf{q}| \ll |\mathbf{K}|$ to the first order:

$$E_\pm(\mathbf{q}) \approx \pm v_F |\mathbf{q}| + O((q/K)^2),$$

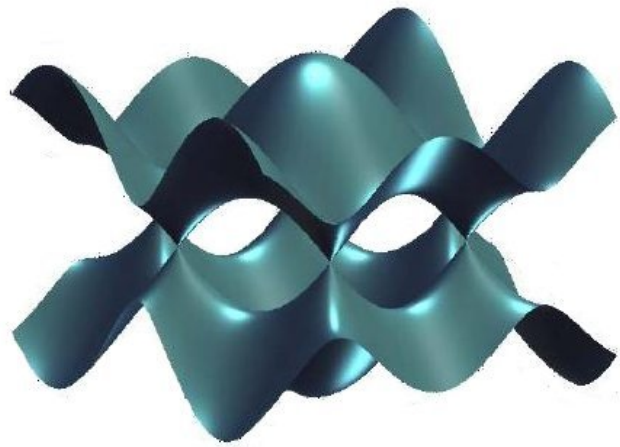

Figure 2.2: Band structure of graphene calculated by the tight-binding model considering only the nearest neighbor interactions. The conduction and valence bands are touching at the K and K' points of BZ.

where v_F is the Fermi velocity given by $v_F = 3ta/2\hbar \approx 1 \times 10^6 m/s$ with $t \approx 2.8$ eV. Notice that near these points, the dispersion relation is linear in the magnitude of the momentum, and the Fermi velocity v_F does not depend on the energy or momentum. This resembles the dispersion relation of a massless particle, hence the effective mass of low-energy excitations of holes and electrons can be considered as zero near those points. This property plays an important role in various electronic and transport properties of graphene.

2.1.3 Massless Dirac fermions

In order to find the effective Hamiltonian governing the electrons and holes around the Fermi energy, which mainly determine the various properties of graphene, let us

consider the Hamiltonian around K:

$$H_{\mathbf{K}}\Psi_{\mathbf{K}} = \begin{pmatrix} 0 & H_{12,\mathbf{K}} \\ H^*_{12,\mathbf{K}} & 0 \end{pmatrix} \begin{pmatrix} c_{A,\mathbf{K}} \\ c_{B,\mathbf{K}} \end{pmatrix} \Psi_{\mathbf{K}} = E(\mathbf{q}) \begin{pmatrix} c_{A,\mathbf{K}} \\ c_{B,\mathbf{K}} \end{pmatrix} \Psi_{\mathbf{K}},$$

and from eqn. (2.3), we can expand $H_{12,\mathbf{K}}$ as,

$$\begin{aligned} H_{12,\mathbf{K}}(\mathbf{k}) = H_{12,\mathbf{K}}(\mathbf{K}+\mathbf{q}) &= t\sum_{i=1}^{3}\exp(i\mathbf{k}\cdot\boldsymbol{\tau_i}) \\ &= t\sum_{i=1}^{3}\exp[i(\mathbf{K}+\mathbf{q})\cdot\boldsymbol{\tau_i}] \\ &= t\sum_{i=1}^{3}\exp(i\mathbf{K}\cdot\boldsymbol{\tau_i})[1+i\boldsymbol{\tau_i}\cdot\mathbf{q}+O(q^2)] \\ &= it\sum_{i=1}^{3}\exp(i\mathbf{K}\cdot\boldsymbol{\tau_i})\boldsymbol{\tau_i}\cdot\mathbf{q}+O(q^2). \end{aligned}$$

We used $\sum_{i=1}^{3}\exp(i\mathbf{K}\cdot\boldsymbol{\tau_i})$ in fourth line. Then we can evaluate the Hamiltonian with (2.1),we arrive at

$$\begin{aligned} H_{\mathbf{K}} &= \frac{i3ta}{2}\left[q_x\begin{pmatrix} 0 & \frac{1}{2}+i\frac{\sqrt{3}}{2} \\ \frac{1}{2}-i\frac{\sqrt{3}}{2} & 0 \end{pmatrix} + q_y\begin{pmatrix} 0 & -\frac{\sqrt{3}}{2}+i\frac{i}{2} \\ -\frac{\sqrt{3}}{2}-i\frac{i}{2} & 0 \end{pmatrix}\right]\begin{pmatrix} c_{A,\mathbf{K}} \\ c_{B,\mathbf{K}} \end{pmatrix} \\ &= \frac{i3ta}{2}\left[q_x\begin{pmatrix} 0 & 1 \\ 1 & 0 \end{pmatrix} + q_y\begin{pmatrix} 0 & i \\ -i & 0 \end{pmatrix}\right]\begin{pmatrix} \tilde{c}_{A,\mathbf{K}} \\ \tilde{c}_{B,\mathbf{K}} \end{pmatrix}. \end{aligned}$$

Note that the effective Hamiltonian can be written as $H_{\mathbf{K}} = i\frac{3}{2}ta\boldsymbol{\sigma}^*\cdot\mathbf{q} = iv_F\boldsymbol{\sigma}^*\cdot\mathbf{q}$. After the same procedures for $\mathbf{q}$ in the vicinity of the other Dirac point, $\mathbf{K}'$, we can also obtain $H_{\mathbf{K}'} = iv_F\boldsymbol{\sigma}\cdot\mathbf{q}$. Notice here that the combined 4×4 matrix of these two forms the massless Dirac-like Hamiltonian:

$$H\begin{bmatrix} \Psi_{\mathbf{K}} \\ \Psi_{\mathbf{K}'} \end{bmatrix} = \begin{bmatrix} \boldsymbol{\sigma}\cdot\mathbf{q}^* & 0 \\ 0 & \boldsymbol{\sigma}\cdot\mathbf{q} \end{bmatrix}\begin{bmatrix} \Psi_{\mathbf{K}} \\ \Psi_{\mathbf{K}'} \end{bmatrix}. \tag{2.6}$$

Then the normalized wavefunctions, in the momentum space, for the momentum around $\mathbf{K}$ and $\mathbf{K}'$ have the form:

$$\Psi_{\pm,\mathbf{K}}(\mathbf{q}) = \frac{1}{\sqrt{2}} \begin{pmatrix} e^{-i\theta_{\mathbf{q}}/2} \\ \pm e^{i\theta_{\mathbf{q}}/2} \end{pmatrix},$$

and

$$\Psi_{\pm,\mathbf{K}'}(\mathbf{q}) = \frac{1}{\sqrt{2}} \begin{pmatrix} e^{i\theta_{\mathbf{q}}/2} \\ \pm e^{-i\theta_{\mathbf{q}}/2} \end{pmatrix},$$

where $\theta_{\mathbf{q}} = \tan^{-1}(q_x/q_y)$. Notice here that the two wavefunctions at $\mathbf{K}$ and $\mathbf{K}'$ are related by time reversal symmetry, which is equivalent to a reflection along the k_x axis. Also, if the phase θ is rotated by 2π, the wavefunction changes sign indicating a phase of π. This change of phase π under rotation is exactly the characteristic of spinors.

There is an another relevant quantity to these eigenfunctions, called helicity, defined as the eigenvalues of the helicity operator, $\hat{h}$, i.e.,

$$\hat{h} = \frac{1}{2}\boldsymbol{\sigma} \cdot \frac{\mathbf{p}}{|\mathbf{p}|}.$$

It is clear from the definition and eqn. (2.6), $\Psi_{\mathbf{K}}$ and $\Psi_{\mathbf{K}'}$ are also eigenstates of $\hat{h}$:

$$\hat{h}\Psi_{\mathbf{K}}(\mathbf{r}) = \pm\frac{1}{2}\Psi_{\mathbf{K}}(\mathbf{r})$$

and the same equation with inverted sign holds for $\Psi_{\mathbf{K}'}$ with inverted sign. Hence the low-energy excitations (electrons and hole around K, and K' points) have well defined *chirality*. Since the magnitude of $|K' - K|$ is significantly large, without a strong scatterer enough to transfer such a large momentum, the helicity is remained to be a good quantum number.

2.1.4 The role of inversion symmetry and time-reversal symmetry in the Dirac Hamiltonian

In this section, we will consider the role of inversion symmetry ($\mathcal{P}$) and time-reversal symmetry ($\mathcal{T}$) in the Dirac Hamiltonian. In general, any 2×2 Hermitian Hamiltonian H can be written as a sum of the Pauli matrices, $H = h_0 I + \sum_{i=1}^{3} h_i \sigma_i$. We have shown that graphene has a low-energy effective Hamiltonian $H(\vec{k}) = h_o(\vec{k})I + h_1(\vec{k})\sigma_1 + h_2(\vec{k})\sigma_2 + h_3(\vec{k})\sigma_3$ with $h_1(\vec{k}) \propto v_{\mathrm{F}} k_x$, $h_2(\vec{k}) \propto v_{\mathrm{F}} k_y$, and $h_3(\vec{k}) = 0$, near the first BZ corners (K and K' points) with v_{F} being the Fermi velocity of $\sim 10^6$ m/s. In this chapter, we will show that the last condition, $h_3(\vec{k}) = 0$ is a consequence of both inversion symmetry, $\mathcal{P}$, and time-reversal symmetry, $\mathcal{T}$, protected by the system.

Bloch Wavefunctions on A(B) site:

$$\langle \vec{r} \, | \vec{k}, A \rangle = \sum_{\vec{R}} \, e^{-i\vec{k}\cdot\vec{R}} \, \phi(\vec{r} - \vec{d}_A - \vec{R})$$

$$\langle \vec{r} \, | \vec{k}, B \rangle = \sum_{\vec{R}} \, e^{-i\vec{k}\cdot\vec{R}} \, \phi(\vec{r} - \vec{d}_B - \vec{R})$$

Inversion ($\mathcal{P}$):

$$\langle \vec{r}\,|\vec{k},A\rangle \xrightarrow{\mathcal{P}} \langle \mathcal{P}^{-1}\vec{r}\,|\vec{k},A\rangle = \langle -\left(\vec{r}-(\frac{\vec{d}_A+\vec{d}_B}{2})\right)+\frac{\vec{d}_A+\vec{d}_B}{2}\;|\vec{k},A\rangle \tag{2.7}$$

$$= \langle -\vec{r}+\vec{d}_A+\vec{d}_B\;|\vec{k},A\rangle \tag{2.8}$$

$$= \sum_{\vec{R}}\; e^{-i\vec{k}\cdot\vec{R}}\;\phi(-\vec{r}+\vec{d}_B-\vec{R}) \tag{2.9}$$

$$= \sum_{\vec{R}}\; e^{-i\vec{k}\cdot\vec{R}}\;\phi\left(-\{\vec{r}-\vec{d}_B-(-\vec{R})\}\right) \tag{2.10}$$

$$= \sum_{\vec{R}'}\; e^{-i(-\vec{k})\cdot\vec{R}'}\;\phi\left(-\{\vec{r}-\vec{d}_B-\vec{R}'\}\right) \tag{2.11}$$

$$= -\sum_{\vec{R}'}\; e^{-i(-\vec{k})\cdot\vec{R}'}\;\phi(\vec{r}-\vec{d}_B-\vec{R}') \tag{2.12}$$

$$\sim \langle \vec{r}\,|-\vec{k},B\rangle. \tag{2.13}$$

Therefore, the inversion flips pseudospin indices (A and B) and the sign of wavevectors. Note that from the the 5th line to the 6th line, we have assumed that the orbital is odd function of $\vec{r}$ as p-orbitals of carbon atoms. It's also o.k. to have even character, but the problem seems to arise when they don't have definite parity. Maybe, there should be different ways to show the consequence.

Time-reversal ($\mathcal{T}$):

$$\langle \vec{r}\,|\vec{k},A\rangle \xrightarrow{\mathcal{T}} \langle \vec{r}\,|\vec{k},A\rangle^* = \sum_{\vec{R}} e^{-i(-\vec{k})\cdot\vec{R}}\,\phi(\vec{r}-\vec{d}_B-\vec{R}) \tag{2.14}$$

$$\sim \langle \vec{r}\,|-\vec{k},A\rangle. \tag{2.15}$$

Time-reversal transformation changes the sign of wavevectors. Spins are all degenerate in our discussion. Using the inversion symmetry $[\mathcal{P},H]=0$ and time-reversal symmetry $[\mathcal{T},H]=0$ of the Hamiltonian H, we can show that the diagonal components of the Hamiltonian are equal to each other, in any given $\vec{k}$, i.e.,

$$H_{AA}(\vec{k}) = \langle \vec{k},A|H|\vec{k},A\rangle \tag{2.16}$$

$$= \langle -\vec{k},B|\mathcal{P}^\dagger H\mathcal{P}|-\vec{k},B\rangle \qquad \text{(Inversion)} \tag{2.17}$$

$$= \langle -\vec{k},B|H|-\vec{k},B\rangle \tag{2.18}$$

$$= \langle \vec{k},B|\mathcal{T}^\dagger H\mathcal{T}|\vec{k},B\rangle \qquad \text{(Time-reversal)} \tag{2.19}$$

$$= \langle \vec{k},B|H|\vec{k},B\rangle \tag{2.20}$$

$$= H_{BB}(\vec{k}). \tag{2.21}$$

Also,

$$
\begin{aligned}
H_{AB}(\vec{k}) &= \langle \vec{k}, A|H|\vec{k}, B\rangle && (2.22)\\
&= \langle -\vec{k}, B|\mathcal{P}^{\dagger}H\mathcal{P}|-\vec{k}, A\rangle \qquad \text{(Inversion)} && (2.23)\\
&= \langle -\vec{k}, B|H|-\vec{k}, A\rangle && (2.24)\\
&= \langle \vec{k}, B|\mathcal{T}^{\dagger}H\mathcal{T}|\vec{k}, A\rangle \qquad \text{(Time-reversal)} && (2.25)\\
&= \langle \vec{k}, B|H|\vec{k}, A\rangle^{*} && (2.26)\\
&= H_{BA}(\vec{k})^{*}, && (2.27)
\end{aligned}
$$

which reconfirms the unitarity of the Hamiltonian. In the fifth line, the antiunitarity of $\mathcal{T}$ is used, which is, $\langle \mathcal{T}x|\mathcal{T}y\rangle = \langle x|y\rangle^{*}$. Again, note that we have assumed that the spin is ignored since are not interested in spin-orbit coupling which conserves both inversion symmetry and time-reversal symmetry.

By denoting $|\vec{k}, A>$ by $\binom{1}{0}$ and $|\vec{k}, B>$ by $\binom{0}{1}$, the Hamiltonian can be written by

$$
H = \begin{pmatrix} H_{AA} & H_{AB} \\ H_{BA} & H_{BB} \end{pmatrix}
$$

and as any 2×2 Hermitian matrix can be written on the basis of $\{I, \vec{\sigma}\}$ the Hamil-

tonian can be written as

$$H(\vec{k}) = h_0(\vec{k})I + \vec{h}(\vec{k}) \cdot \vec{\sigma} \tag{2.28}$$

$$= h_0 I + h_1\sigma_1 + h_2\sigma_2 + h_3\sigma_3, \tag{2.29}$$

where $I = \left(\begin{smallmatrix} 1 & 0 \\ 0 & 1 \end{smallmatrix}\right), \sigma_1 = \left(\begin{smallmatrix} 0 & 1 \\ 1 & 0 \end{smallmatrix}\right), \sigma_2 = \left(\begin{smallmatrix} 0 & -i \\ i & 0 \end{smallmatrix}\right)$, and $\sigma_3 = \left(\begin{smallmatrix} 1 & 0 \\ 0 & -1 \end{smallmatrix}\right)$. Also $\vec{h} = (h_1, h_2, h_3)$, and $\vec{\sigma} = (\sigma_1, \sigma_2, \sigma_3)$. On this basis, the inversion symmetry of the Hamiltonian can be represented by

$$\sigma_2 H(-\vec{k})\sigma_2 = H(\vec{k}) \tag{2.30}$$

and the time-reversal symmetry can be represented by

$$H(-\vec{k})^* = H(\vec{k}). \tag{2.31}$$

Therefore, it is clear that the simultaneous applications of Eqns. (5) and (6) to the Hamiltonian result in $h_3(\vec{k}) = 0$, which is a different way to express of Eqn. (3). One merit of using this basis is that the eigenvalues of the Hamiltonian can readily be identify by the norm of the $\vec{h}$, i.e.,

$$E(\vec{k}) = h_0(\vec{k}) \pm \sqrt{h_1(\vec{k})^2 + h_2(\vec{k})^2 + h_3(\vec{k})^2}. \tag{2.32}$$

2.2 Tight-binding description of the electronic structure of silicene

Silicene is a two-dimensional (2D) honeycomb lattice made of silicon atoms. Different from graphene, silicene in its planar structure develops a phonon mode with

imaginary frequencies, which dictates the planar geometry is unstable. The instability can be lifted via low-buckling with one of the two sublattices being shifted either upward or downward with respect to the other sublattice plane [33]. The buckling makes silicene unique distinct from either single-layered graphene or bilayer graphene. Even after the buckling, the structure still respects the inversion symmetry with respect to the Si-Si bond center, as well as C_3 symmetry with respect to the z-axis, which preserves the Dirac cone-like band structure, which is a similar property with graphene. Also, buckling spatially separates the sublattices thus allowing a perpendicular electric field to open a band gap as in the case of bilayer graphene. In this section, we provide basic electronic properties of silicene based on a tight-binding analysis, which is mostly based on the results of Ref. [3]. We also provide the role of inversion symmetry ($\mathcal{P}$) and time-reversal symmetry ($\mathcal{T}$) in the low-energy bands of silicene, and comment on the possible origin of Dirac points protected even after the buckling.

2.2.1 Tight-binding analysis

As previously mentioned, the band structure of silicene is similar to that of graphene, and hence, the low-energy Hamiltonian governing quasi-particles near the Fermi energy of silicene is also well-described by the massless Dirac Fermion model

$$H_K = \varepsilon_1 I_2 + \begin{pmatrix} 0 & v_F k_+ \\ v_F k_- & 0 \end{pmatrix} \tag{2.33}$$

on the basis of $\{\phi_1, \phi_2\}$ and with the Fermi velocity v_F [3]. Due to the buckling, the character of the Dirac orbitals are significantly changed with the all the four

Parameters (eV)	$V_{ss\sigma}$	$V_{sp\sigma}$	$V_{pp\sigma}$	$V_{pp\pi}$	Δ
Graphene	-6.769	5.580	5.037	-3.033	-8.868
Silicene (sp^3, diamond)	-1.93	2.54	4.47	-1.12	-7.03

Table 2.1: The hopping parameters of various orbitals in graphene and silicene [3]. In silicene case, hopping parameters corresponds to those of diamond, i.e., sp^3 bonds.

orbitals (p_x, p_y, p_z, and s) being involved, i.e.,

$$\phi_1 = u_{11}p_z^A + u_{21}s^A + u_{31}\left[\frac{1}{\sqrt{2}}(p_x^B - ip_y^B)\right] \tag{2.34}$$

$$\phi_2 = u_{11}p_z^B + u_{21}s^B + u_{31}\left[\frac{1}{\sqrt{2}}(p_x^A - ip_y^A)\right]. \tag{2.35}$$

Also, while the Fermi velocity of graphene is a function of only a hopping parameter $V_{pp\pi}$, the Fermi velocity v_F of silicene is a function of various hopping parameters $V_{pp\pi}, V_{pp\sigma}, V_{ss\sigma}$, and $V_{sp\sigma}$, i.e.,

$$\begin{aligned} v_F = \tfrac{-\sqrt{3}a}{2}\big[u_{11}^2(V_{pp\pi}\sin^2\theta + V_{pp\sigma}\cos^2\theta) - u_{21}^2 V_{ss\sigma} + 2u_{11}u_{21}\cos\theta\ V_{sp\sigma} \\ -\tfrac{1}{2}|u_{31}|^2\sin^2\theta(V_{pp\sigma} - V_{pp\pi})\big], \end{aligned} \tag{2.36}$$

where u_{ij} (i =1, 2, and 3) is defined by

$$[u_{ij}] = \begin{pmatrix} \frac{1}{\alpha_1} & \frac{1}{\alpha_2} & \frac{1}{\alpha_3} \\ \frac{V_2\varepsilon_1}{\alpha_1(\Delta-\varepsilon_1)V_3} & \frac{V_2\varepsilon_2}{\alpha_2(\Delta-\varepsilon_2)V_3} & \frac{V_2\varepsilon_3}{\alpha_3(\Delta-\varepsilon_3)V_3} \\ \frac{i\varepsilon_1}{\alpha_1 V_3} & \frac{i\varepsilon_2}{\alpha_2 V_3} & \frac{i\varepsilon_3}{\alpha_3 V_3} \end{pmatrix} \tag{2.37}$$

with the normalization factors

$$\alpha_i = \sqrt{1 + \left[\frac{V_2\varepsilon_i}{(\Delta-\varepsilon_i)V_3}\right]^2 + \left(\frac{\varepsilon_i}{V_3}\right)^2}, \tag{2.38}$$

and ε_i are eigenvalues of

$$\begin{pmatrix} 0 & 0 & -iV_3 \\ 0 & \Delta & iV_2 \\ iV_3 & -iV_2 & 0 \end{pmatrix} \text{ and } \begin{pmatrix} 0 & 0 & -iV_3 \\ 0 & \Delta & -iV_2 \\ iV_3 & iV_2 & 0 \end{pmatrix}. \tag{2.39}$$

Finding ε_i:

Eigenvlues ε_1, ε_2, and ε_3 are roots of the eigenvalue equation

$$E^3 - \Delta E^2 - (V_2^2 + V_3^2)E + \Delta V_3^2 = 0. \tag{2.40}$$

The discriminant $\mathcal{D}_3$ of this cubic equation ($\mathcal{D}_3 = 18abcd - 4b^3d + b^2c^2 - 4ac^3 - 27a^2d^2$) is

$$\begin{aligned} \mathcal{D}_3 &= 4V_3^2\Delta^4 + \left(V_2^4 + 20V_2^2V_3^2 - 8V_3^4\right)\Delta^2 + 4(V_2^2 + V_3^2)^3, \qquad (2.41) \\ &= 4V_3^2\left(\Delta^2 + \frac{V_2^4 + 20V_2^2V_3^2 - 8V_3^2}{8V_3^4}\right)^2 - \frac{V_2^2(V_2^2 - 8V_3^2)^3}{16V_3^2} \qquad (2.42) \end{aligned}$$

which is always greater than zero ($\mathcal{D}_3 \geq 0$), because the last term $-\frac{V_2^2(V_2^2-8V_3^2)^3}{16V_3^2}$ is always greater than zero whenever $\frac{V_2^4+20V_2^2V_3^2-8V_3^2}{8V_3^4} > 0$. This means that there always exist real eigenvalues, which is also guaranteed by the Hamiltonian being Hermitian operator. The three eigenvalues can be directly found via the general

formula of roots of a cubic equation $ax^3 + bx^2 + cx + d = 0$, i.e.,

$$
\begin{aligned}
x_1 &= -\frac{b}{3a} \\
&\quad -\frac{1}{3a}\sqrt[3]{\frac{1}{2}\left[2b^3 - 9abc + 27a^2d + \sqrt{-27a^2\mathcal{D}_3}\right]} && (2.43)\\
&\quad -\frac{1}{3a}\sqrt[3]{\frac{1}{2}\left[2b^3 - 9abc + 27a^2d - \sqrt{-27a^2\mathcal{D}_3}\right]} && (2.44)\\
x_2 &= -\frac{b}{3a} && (2.45)\\
&\quad +\frac{1+i\sqrt{3}}{6a}\sqrt[3]{\frac{1}{2}\left[2b^3 - 9abc + 27a^2d + \sqrt{-27a^2\mathcal{D}_3}\right]} && (2.46)\\
&\quad +\frac{1-i\sqrt{3}}{6a}\sqrt[3]{\frac{1}{2}\left[2b^3 - 9abc + 27a^2d - \sqrt{-27a^2\mathcal{D}_3}\right]} && (2.47)\\
x_3 &= -\frac{b}{3a} && (2.48)\\
&\quad +\frac{1-i\sqrt{3}}{6a}\sqrt[3]{\frac{1}{2}\left[2b^3 - 9abc + 27a^2d + \sqrt{-27a^2\mathcal{D}_3}\right]} && (2.49)\\
&\quad +\frac{1+i\sqrt{3}}{6a}\sqrt[3]{\frac{1}{2}\left[2b^3 - 9abc + 27a^2d - \sqrt{-27a^2\mathcal{D}_3}\right]}, && (2.50)(2.51)
\end{aligned}
$$

where $\mathcal{D}$ is the above-mentioned discriminant. Note that when $\mathcal{D}$ is greater than zero, the expression under the square root sign is always negative, the square root is pure imaginary, and thus, last two terms of each root are their complex conjugates.

Therefore, the roots are all real values and can be expressed as

$$x_1 = -\frac{b}{3a} - \frac{2}{3a}\mathrm{Re}\left\{\sqrt[3]{\frac{1}{2}\left[2b^3 - 9abc + 27a^2d + \sqrt{-27a^2\mathcal{D}_3}\right]}\right\} \tag{2.52}$$

$$= -\frac{b}{3a} + \frac{2}{3a}\sqrt[3]{R}\cos\left(\frac{\Theta}{3} + \pi\right) \tag{2.53}$$

$$x_2 = -\frac{b}{3a} + \frac{2}{3a}\mathrm{Re}\left\{\left(\frac{1}{2} + i\frac{\sqrt{3}}{2}\right)\sqrt[3]{\frac{1}{2}\left[2b^3 - 9abc + 27a^2d + \sqrt{-27a^2\mathcal{D}_3}\right]}\right\} \tag{2.54}$$

$$= -\frac{b}{3a} + \frac{2}{3a}\sqrt[3]{R}\cos\left(\frac{\Theta}{3} + \frac{\pi}{3}\right) \tag{2.55}$$

$$x_3 = -\frac{b}{3a} + \frac{2}{3a}\mathrm{Re}\left\{\left(\frac{1}{2} - i\frac{\sqrt{3}}{2}\right)\sqrt[3]{\frac{1}{2}\left[2b^3 - 9abc + 27a^2d + \sqrt{-27a^2\mathcal{D}_3}\right]}\right\} \tag{2.56}$$

$$= -\frac{b}{3a} + \frac{2}{3a}\sqrt[3]{R}\cos\left(\frac{\Theta}{3} - \frac{\pi}{3}\right), \tag{2.57}$$

where $\sqrt[3]{R} = \left(b^2 - 3ac\right)^{\frac{1}{2}}$, and $\Theta = \tan^{-1}\left(\frac{\sqrt{27a^2\mathcal{D}}}{2b^3 - 9abc + 27a^2d}\right)$. In applying these general formulae to our eigenvalue problem, we may set $a = 1$, $b = -\Delta$, $c = -(V_2^2 + V_3^2)$, and $d = \Delta V_3^2$. Then we can obtain

$$\sqrt[3]{R} = \left[\Delta^2 + 3(V_2^2 + V_3^2)\right]^{\frac{1}{2}}, \tag{2.58}$$

and

$$\Theta = \tan^{-1}\left(\frac{3\sqrt{3\mathcal{D}_3}}{-\Delta(2\Delta^2 + 9V_2^2 - 18V_3^2)}\right). \tag{2.59}$$

Here, $\mathcal{D}_3$ is the previously obtained discriminant.

2.2.2 The role of the point-group symmetries

Suppose graphene is perturbed by buckling with one sublattice being shifted along the perpendicular direction to the other sublattice plane, or by strains applied either

uniaxially or biaxially. Here, what we would like to show is that the band structure still retains the zero-gap if the following conditions are satisfied.

1. Two-band model is still valid near the Hamiltonian.

2. The perturbed Hamiltonian still respects $\mathcal{P}$ and $\mathcal{T}$.

Remember that we have assumed that the orbitals consist of the Dirac bands have well-defined parities when proving the inversion symmetry exchanges the A and B sublattice indices. This can cause a problem when dealing with the buckling since it can mix s and p orbitals. Nonetheless, since the buckling cannot open a gap while the Dirac bands present decent amount of s-orbital character due to the buckling as we will discuss later, we believe this condition is not necessary. Anyway, the orbitals localized at B-sites ϕ_B should be constructed by $\phi_A(\mathcal{P}^{-1}\vec{r})$ where $\phi_A(\vec{r})$ is the participating orbital localized at A-sites

The fist condition ensures that the perturbed Hamiltonian $H(\vec{k})$ can be expressed by $\vec{h}(\vec{k})$, i.e.,

$$H(\vec{k}) = h_0(\vec{k})I + h_1(\vec{k})\sigma_1 + h_2(\vec{k})\sigma_2 + h_3(\vec{k})\sigma_3. \tag{2.60}$$

The second Condition enforces $h_3(\vec{k}) = 0$ regardless of $\vec{k}$ as previously discussed, i.e.

$$H(\vec{k}) = h_0(\vec{k})I + h_1(\vec{k})\sigma_1 + h_2(\vec{k})\sigma_2. \tag{2.61}$$

Since the lattice might lose C_3 symmetry as in the case of graphene under a uniaxial strain, we expect that $h_1(\vec{k})$ and $h_2(\vec{k})$ may not vanish at K-point or even linear in $\vec{k}$. Rather, in general, we are supposed to consider a non-vanishing constant

at $\vec{k} = 0$ (K-point), i.e.

$$\langle \vec{k}, A|H|\vec{k}, B\rangle = \alpha_0 + \vec{\alpha}_1 \cdot \vec{k} + \mathcal{O}(k^2) \tag{2.62}$$

near the K and K' points, where α_0 is a complex constant and $\vec{\alpha}_1 = (\alpha_{1x}, \alpha_{1y})$ is a complex vector composed of coefficents of k_x and k_y. Since we only consider the band structure near the K-point, we ignore higher order-terms of k, i.e. $\mathcal{O}(k^2)$. Then, in terms of the Pauli matrices, the Hamiltonian can be write by

$$\begin{aligned} H(\vec{k}) &= h_0(\vec{k})I + h_1(\vec{k})\sigma_1 + h_2(\vec{k})\sigma_2. & (2.63)\\ &= h_0(\vec{k})I + (\alpha_0^r + \alpha_{1x}^r k_x + \alpha_{1y}^r k_y)\sigma_1 - (\alpha_0^i + \alpha_{1x}^i k_x + \alpha_{1y}^i k_y)\sigma_2, & (2.64) \end{aligned}$$

where i and r denote the real part and imaginary part of the corresponding coefficients. Therefore, the eigenvalues are calculated as

$$E(\vec{k}) = h_0(\vec{k}) \pm \sqrt{|\alpha_0^r + \alpha_{1x}^r k_x + \alpha_{1y}^r k_y|^2 + |\alpha_0^i + \alpha_{1x}^i k_x + \alpha_{1y}^i k_y|^2}, \tag{2.65}$$

and the question is reduced to the finding of the root of the algebraic equations

$$\begin{aligned} \alpha_0^r + \alpha_{1x}^r k_x + \alpha_{1y}^r k_y &= 0 & (2.66)\\ \alpha_0^i + \alpha_{1x}^i k_x + \alpha_{1y}^i k_y &= 0, & (2.67) \end{aligned}$$

which have a single root at $\vec{k} = (\tilde{k}_x, \tilde{k}_y)$ where

$$\begin{pmatrix} \tilde{k}_x \\ \tilde{k}_y \end{pmatrix} = \frac{-1}{\alpha_{1x}^r \alpha_{1y}^i - \alpha_{1x}^r \alpha_{1y}^r} \begin{pmatrix} \alpha_{1y}^i & -\alpha_{1y}^r \\ -\alpha_{1x}^i & \alpha_{1x}^r \end{pmatrix} \begin{pmatrix} \alpha_0^r \\ \alpha_0^i \end{pmatrix}, \tag{2.68}$$

if the following condition is satisfied.

$$\alpha_{1x}^r \alpha_{1y}^i - \alpha_{1x}^r \alpha_{1y}^r \neq 0. \tag{2.69}$$

The possibility for the determinant $\alpha^r_{1x}\alpha^i_{1y} - \alpha^r_{1x}\alpha^r_{1y}$ to vanish can be an interesting question since it can allow a gap totally different origin, or more interestingly the Fermi arc. We should come back to this question but at present, we presume that Eqn. (18) is satisfied. The existence of the root means gap in not opened by the perturbation. In this case, we may conclude that $\mathcal{P}$ and $\mathcal{T}$ protect the Fermi loci.

CHAPTER 3

Computational methods

3.1 Introduction

Diverse properties of a condensed matter system can be understood by manifesting their electronic structures. Precise prediction of electronic structures has been always the most important goal of the condensed matter physics. In this respect, density functional theory (DFT) has been successful and now became the most wide spread and popular method to predict the electronic structures of a many-body system.

In principle, the properties of any (non-relativistic) time-independent quantum system can be determined by solving the Schrödinger equation,

$$\mathcal{H}\Psi(\mathbf{r}_1, \mathbf{r}_2, \ldots, \mathbf{r}_N) = E\Psi(\mathbf{r}_1, \mathbf{r}_2, \ldots, \mathbf{r}_N), \tag{3.1}$$

where, $\mathcal{H}$, Ψ and E are the Hamiltonian, many-body wavefunction and total energy of the system. Matter consists of electrons and nuclei interacting with each other via the Coulomb interaction, consequently the Hamiltonian for any such system is

given by,

$$\mathcal{H} = -\sum_i \frac{\hbar^2}{2m_e}\nabla_i^2 - \sum_I \frac{\hbar^2}{2M_I}\nabla_I^2 + \frac{1}{2}\sum_{I\neq J}\frac{Z_I Z_J e^2}{|\mathbf{R}_I - \mathbf{R}_J|} + \sum_{i,I}\frac{Z_I e^2}{|\mathbf{r}_i - \mathbf{R}_I|} + \frac{1}{2}\sum_{i\neq j}\frac{e^2}{|\mathbf{r}_i - \mathbf{r}_j|} \tag{3.2}$$

The first two terms in (3.2) are the kinetic energy contributions from the nuclei and the electrons respectively, and the rest are Coulomb potential energy terms arising from the ion-ion repulsion, ion-electron attraction and the electron-electron repulsion respectively. However, the Schrödinger equation (3.1) is a many-body equation and difficult to solve directly. Density functional theory provides *a*d hoc. for this problem with great success. In this Chapter, The essence of density functional theory will be briefly reviewed. Readers who want more extensive and complete review can refer to the literatures [34, 35, 36], based on which this review is written.

3.2 Density Functional Theory

DFT is developed based on the fundamental tenet that the ground state properties of a given system can be determined by the ground state charge density [37, 38],

$$\rho(\mathbf{r}_1) = \int \Psi^*(\mathbf{r}_1, \mathbf{r}_2, \ldots, \mathbf{r}_n)\Psi(\mathbf{r}_1, \mathbf{r}_2, \ldots, \mathbf{r}_n)d\mathbf{r}_2 \cdots d\mathbf{r}_n, \tag{3.3}$$

where $\Psi(\mathbf{r}_1, \mathbf{r}_2, \ldots, \mathbf{r}_n)$ a many-body wavefunctions for the ground state. Any properties of a system of many interacting particles is considered to be a functional of the ground state density $\rho(\mathbf{r}_1)$, It is important to find the ground state density as well as a potential that generates the charge density. Solving the many-body problem in terms of charge density is advantageous over solving the problem based on wave function since a charge density is a scalar function of three spatial variable ($\vee r$)

while a wavefunction of a function of $3N$ variables describing the positions of N electrons. The idea to treat the problem using a charge density goes back the early work of Thomas and Fermi [39]. They treated the energy as a functional of a charge density and energy is expected to be the summation of the kinetic energy of a uniform electron gas and the classical electrostatic interaction between the electrons and nuclei for an electron gas of a given energy. The idea of Thomas and Fermi is later extended by adding the exchange energy of the electrons from the work of Dirac. However, it is turns out that the Thomas-Fermi theory generates poor results due to the inappropriate approximations in kinetic energy [39]. Later, Kohn, Hohenberg, and Sham [37, 38] described the kinetic energy in terms of wavefunctions instead of a charge density, as described below, and this treatment is turned out to be successful.

3.2.1 Hohenberg-Kohn theorem

According to the Hohenberg-Kohn theorem, the ground state properties of a many-electron system under an external potential v_{ext} can be uniquely determined by the electron density. The Hohenberg-Kohn theorem states:

Theorem 1. *The external potential v_{ext} is a unique functional of the electron density $n(\mathbf{r})$. Thus the Hamiltonian, and hence all ground state properties, are determined solely by the electron density.*

The many-body Hamiltonian $\mathcal{H}$ describes the ground state properties of a many-electron system by determining the ground state many-body wavefunction Ψ. This means that the Hohenberg-Kohn theorem guarantees that the kinetic energy and

electron-electron interaction energy should also be functionals of the electron density $n(\mathbf{r})$. Therefore, one may define the energy functional

$$F[n(\mathbf{r})] = \langle\Psi|(T + V_{ee})|\Psi\rangle. \tag{3.4}$$

Here T and V_{ee} are the kinetic energy operator and the electron-electron interaction operator, respectively. This functional F should be universal in the sense that it is independent of the external potential concerned. Although the explicit form of the functional in terms of electron density is unknown, one may then define using this functional, for a given external potential $v_{\text{ext}}(\mathbf{r})$ as

$$E\left[n(\mathbf{r})\right] = \int d\mathbf{r} n(\mathbf{r}) v_{\text{ext}}(\mathbf{r}) + F\left[n(\mathbf{r})\right]. \tag{3.5}$$

Then, we may be able to write the energy (for a non-degenerate ground state) in terms of the ground state many-body wavefunction Ψ as

$$E\left[n(\mathbf{r})\right] = \langle\Psi\left|\mathcal{H}\right|\Psi\rangle \tag{3.6}$$

with the Hamiltonian given by

$$\mathcal{H} = F + V \tag{3.7}$$

where V is the operator corresponding to the external potential, and F is the electronic Hamiltonian

$$F = T + V_{ee}. \tag{3.8}$$

Proof. Suppose that there are two potentials $v_1(\mathbf{r})$ and $v_2(\mathbf{r})$, which differ each other by more than an additive constant, and these two potentials produce different ground state wavefunctions $\Psi_1(\mathbf{r})$ and $\Psi_2(\mathbf{r})$. Also suppose that these both potential give

rise to the same ground state density, $n(\mathbf{r})$. The variational principle then dictates that

$$\begin{aligned} E_1 \leq \langle \Psi_2 | H_1 | \Psi_2 \rangle &= \langle \Psi_2 | H_2 | \Psi_2 \rangle + \langle \Psi_2 | H_1 - H_2 | \Psi_2 \rangle \\ &= E_2 + \int n(\mathbf{r}) \left[v_1(\mathbf{r}) - v_2(\mathbf{r}) \right] d\mathbf{r} \end{aligned} \tag{3.9}$$

Note that by interchanging the indices 1 and 2, one may obtain a similar expression, and by adding the two inequalities, we may draw a contradiction,

$$E_1 + E_2 \leq E_1 + E_2. \tag{3.10}$$

Hence the theorem 1 is proved. □

Theorem 2. *The ground state energy may be variationally obtained; the density that minimizes the total energy is the exact ground state density.*

Proof. In order to prove the theorem, let us first introduce the concept of "N-*representability*". One may say a density is N-representable whenever it can be obtained from an antisymmetric wavefunction $\psi(\mathbf{r}_1, \mathbf{r}_2, \ldots, \mathbf{r}_N)$, from which we may define the functional

$$F[n] = \min_{\psi \to n} \langle \psi | T + V_{\text{ee}} | \psi \rangle. \tag{3.11}$$

Here the minimum is taken over all the possible wave functions ψ which can generate the density n. Then if one introduces $\psi^n_{min}(\mathbf{r})$ for a wavefunction that minimizes (3.11) such that

$$F[n] = \langle \psi^n_{\text{min}} | T + V | \psi^n_{\text{min}} \rangle \tag{3.12}$$

then

$$\int V_{\text{ext}}(\mathbf{r})n(\mathbf{r})d\mathbf{r} + F\left[n\right] = \langle \psi^n_{\text{min}} \left| V + T + V_{\text{ee}} \right| \psi^n_{\text{min}} \rangle$$
$$\geq E_{\text{GS}} \tag{3.13}$$

with equality at the minimum, which proves the second theorem. □

3.2.2 Kohn-Sham equation

Although the Hohenberg-Kohn theorem guarantees the existence of the ground state density determining the ground state properties of a many-body system, it does not provide a specific method to find the ground state density of the system. Walter Kohn and Lu Jeu Sham [38] tackled this problem and provided a route toward a practical way to obtain the ground state density by constructing the Kohn-Sham equation. Suppose that the ground state energy is given as a functional of the charge density

$$E\left[\rho(\mathbf{r})\right] = T\left[\rho(\mathbf{r})\right] + \int \rho(\mathbf{r})v(\mathbf{r})\ d\mathbf{r} + E_{ee}. \tag{3.14}$$

Here the first term $T\left[\rho(\mathbf{r})\right]$ is the kinetic energy functional, the second term is the interaction with the external potential, including the electron-nuclei interaction, and the last term is the electron-electron interaction which can be written as

$$E_{ee}\left[\rho(\mathbf{r})\right] = \frac{1}{2}\int \frac{\rho(\mathbf{r})\rho(\mathbf{r}')}{|\mathbf{r}-\mathbf{r}'|}\ d\mathbf{r}d\mathbf{r}' + E_{xc}\left[\rho(\mathbf{r})\right]. \tag{3.15}$$

The first term on the right hand side of (3.15) describes the electron-electron electrostatic interaction, while the second term describes the non-classical exchange-correlation energy.

Kohn and Sham derived a set of single-particle Schrödinger eqnarray by introducing auxiliary wavefunctions ψ_i, with

$$\rho(\mathbf{r}) = \sum_{i=1}^{n} \psi_i^*(\mathbf{r})\psi_i(\mathbf{r}) \tag{3.16}$$

where "n" represents the number of electrons. The kinetic energy is then given by

$$T\left[\rho(\mathbf{r})\right] = -\frac{\hbar^2}{2m}\sum_{i}^{n}\langle\psi_i|\nabla^2|\psi_i\rangle. \tag{3.17}$$

If the wavefunctions are orthonormal, i.e.,

$$\int \psi_i^*(\mathbf{r})\psi_j(\mathbf{r})d\mathbf{r} = \delta_{ij}, \tag{3.18}$$

we can define a functional of the wavefunctions

$$\Omega\left[\psi_i\right] = E\left[\rho(\mathbf{r})\right] - \sum_i\sum_j \epsilon_{ij}\int \psi_i^*(\mathbf{r})\psi_j(\mathbf{r})d\mathbf{r}. \tag{3.19}$$

Here ϵ_{ij} are Lagrange multipliers constraining the wavefunctions to be orthonormal. Minimization of $\Omega\left[\psi_i\right]$ with respect to $\psi_i^*(\mathbf{r})$ gives rise to the Kohn-Sham equation,

$$\left[-\frac{\hbar^2}{2m}\nabla^2 + v_{\text{eff}}(\mathbf{r})\right]\psi_i(\mathbf{r}) = \epsilon_i\psi_i(\mathbf{r}) \tag{3.20}$$

with v_{eff} being

$$v_{\text{eff}}(\mathbf{r}) = v(\mathbf{r}) + \int \frac{\rho(\mathbf{r}')}{|\mathbf{r}-\mathbf{r}'|}d\mathbf{r}' + v_{\text{xc}}(\mathbf{r}), \tag{3.21}$$

and $v_{\text{xc}}(\mathbf{r})$ being the exchange-correlation potential given by

$$v_{\text{xc}}(\mathbf{r}) = \frac{\delta E_{\text{xc}}}{\delta\rho(\mathbf{r})}. \tag{3.22}$$

Deriving from (3.19) to (3.20), a unitary transform is applied to make it sure that the wavefunctions $\phi_i(\mathbf{r})$ are orthonormal. A many-body problem is now reduced to solving a single-particle Schrödinger equation (3.20) with an effective local potential v_{eff} defined in (3.21).

3.2.3 Exchange-correlation functional

Although Kohn-Sham theory makes a problem much easier, it is still extremely hard to solve the problem in practice because we do not know explict form of energy functionals. So, it is unavoidable to introduce an approximation to further simplify the problem. For this purpose, we implicitly define the exchange-correlation functional $E_{\mathrm{XC}}[n(\mathbf{r})]$ as below.

$$E_{\mathrm{XC}}[n(\mathbf{r})] = T[n(\mathbf{r})] - T_{\mathrm{s}}[n(\mathbf{r})] + E_{\mathrm{ee}}[n(\mathbf{r})] - E_{\mathrm{H}}[n(\mathbf{r})] \tag{3.23}$$

where $T[n(\mathbf{r})]$ and $E_{\mathrm{ee}}[n(\mathbf{r})]$ are the exact kinetic and electron-electron interaction energies, respectively. The intention for doing this is to make the unknown contribution to the total energy of the non-interacting system as local as possible. Although E_{XC} makes local contributions, it is turned out that its contribution is still significant being amount to the binding energy of many systems. Therefore, an accurate treatment of exchange and correlation is highly desirable for better predictions of material properties. Recently, there are diverse approximations describing the exchange-correlation potential. Here we will quickly review local density approximation (LDA) and generalized gradient approximation (GGA), which are employed in this thesis.

3.2.4 Local density approximation

LDA is the simplest approximation, yet still having powerful predicting applications in many solids, within which the density can be treated locally as an uniform electron gas. More specifically, it treats the exchange correlation energy at a given point as that of a uniform electron gas having the same density. LDA was originally

introduced by Kohn and Sham [38]. It is widely accepted that LDA is a decent approximation soundly working in a slowly varying density. This approximation assumes the exchange-correlation energy for a density $\rho(\mathbf{r})$ to be given by

$$E_{\mathrm{xc}}^{\mathrm{LDA}} = \int \rho(\mathbf{r}) \epsilon_{\mathrm{xc}}^{\mathrm{LDA}}(\rho) d\mathbf{r}. \tag{3.24}$$

Here $\epsilon_{\mathrm{xc}}(\rho)$ is the exchange-correlation energy per particle for an uniform electron gas of density. The exchange-correlation potential is then given by

$$v_{\mathrm{xc}}^{\mathrm{LDA}}[\rho(\mathbf{r})] = \frac{\delta E_{\mathrm{xc}}^{\mathrm{LDA}}}{\delta \rho(\mathbf{r})} = \epsilon_{\mathrm{xc}}^{\mathrm{LDA}}(\rho) + \rho(\mathbf{r}) \frac{\partial \epsilon_{\mathrm{xc}}(\rho)}{\partial \rho}. \tag{3.25}$$

This can then be employed in (3.21) for practical calculations, with the exchange-correlation energy of an uniform electron gas of a given density

$$\epsilon_{\mathrm{xc}}^{\mathrm{LDA}}(\rho) = \epsilon_{\mathrm{x}}^{\mathrm{LDA}}(\rho) + \epsilon_{\mathrm{c}}^{\mathrm{LDA}}(\rho), \tag{3.26}$$

where the exchange potential is given by the Dirac functional [34, 36]

$$\epsilon_{x}^{\mathrm{LDA}}[\rho(\mathbf{r})] = -\frac{3}{4} \left(\frac{3}{\pi} \right)^{\frac{1}{3}} \rho(\mathbf{r})^{\frac{1}{3}}. \tag{3.27}$$

Accurate estimations for $\epsilon_{\mathrm{c}}(\rho)$ can be obtained from more accurate level of calculations such as quantum Monte Carlo (QMC) calculations. These estimations are then interpolated to provide an analytic form for $\epsilon_{\mathrm{c}}(\rho)$. In particular, Perdew and Zunger [40] parameterized the correlation energy based on QMC simulation of Ceperley and Alder [41] as

$$\epsilon_{c}^{\mathrm{PZ}}(\rho) = \begin{cases} A \ln r_s + B + C r_s \ln r_s + D r_s, & r_s < 1, \\ \gamma / (1 + \beta_1 \sqrt{r_s} + \beta_2 r_s), & r_s > 1, \end{cases} \tag{3.28}$$

where $A = 0.0311$, $B = -0.048$, $C = 0.002$, $D = -0.0116$, $\gamma = -0.1423$, $\beta_1 = 1.0529$, $\beta_2 = 0.334$, and $r_x = (3/4\pi\rho)^{1/3}$ is the average distance between electrons in uniform electron gas.

3.2.5 Generalized-gradient approximations

Success in LDA has lead to the search for better description of the exchange-correlations potential via the modification of LDA. The first step for this modification is to introduce the gradient of the density $|\nabla\rho(\mathbf{r})|$, i.e.,

$$E_{\mathrm{xc}}^{\mathrm{GGA}} = \int \rho(\mathbf{r})\epsilon_{\mathrm{xc}}^{\mathrm{LDA}}(\rho)F_{\mathrm{xc}}(\rho, \nabla\rho, \nabla^2\rho, \cdots)d\mathbf{r}. \tag{3.29}$$

where F_{XC} is an enhancement factor introduced to modify the LDA expression, so that the inhomogeniety in the electron density may be accounted for. Among many other GGAs, Perdew-Burke-Erenzerhof (PBE)-GGA [42] is one of the most popular choices due to its satisfactory conditions for the exchange-correlation hole and single fitting parameter which is not sensitive to the accuracy of the result. The detailed form of the correlation term within PBE-GGA is given by

$$\epsilon_{\mathrm{c}}^{\mathrm{PBE}}(\rho) = \int \rho(\mathrm{r}) \left[\epsilon_{\mathrm{c}}^{\mathrm{hom}}(\rho) + H(\rho, t)\right], \tag{3.30}$$

where $\epsilon_{\mathrm{c}}^{\mathrm{hom}}(\rho)$ is the correlation energy of homogeneous electron gas, and t is a dimensionless variable of $\rho(\mathbf{r})$ defined by $t = |\nabla\rho|/2\phi k_s\rho$, with $\phi = [(1+\zeta)^{2/3} + (1-\zeta^{2/3}]/2$ and $k_s = \sqrt{4k_F/\pi a_0}$ (the Thomas-Fermi screening wavenumber, $a_0 = \hbar^2/me^2$). The function H is given by

$$H = \frac{e^2}{a_0}\gamma\pi^3 \ln\left[1 + \frac{\beta}{\gamma}t^2\left(\frac{1+At^2}{1+At^2+A^2t^4}\right)\right], \tag{3.31}$$

where

$$A = \frac{\beta}{\gamma}\left[\exp\left(\frac{-\epsilon_{\mathrm{c}}^{\mathrm{hom}}}{\gamma\pi^3 e^2/a_0}\right) - 1\right]^{-1} \tag{3.32}$$

The detailed form of the exchange term within PBE-GGA is given by

$$E_{\mathrm{x}}^{\mathrm{PBE}} = \int \rho(\mathbf{r})\epsilon_{\mathrm{xc}}^{\mathrm{hom}}(\rho)F_{\mathrm{x}}(\rho, \nabla\rho, \nabla^2\rho, \cdots)d\mathbf{r}. \tag{3.33}$$

The enhancement factor of F_{x} is given by

$$F_{\mathrm{x}} = 1 + \kappa - \frac{\kappa}{(1 + \mu s^2/\kappa)}, \tag{3.34}$$

where s is a dimensionless function of $\rho(\mathbf{r})$ defined by $s = |\nabla\rho|/2k_{\mathrm{F}}\rho$, and numerical values, κ and μ are 0.804 and 0.21951, respectively.

3.3 Pseudopotential

Electrons in solids can be crudely divided into two kinds, one of which is core electrons and the other is valence electrons. Core electrons are characterized by strong localization near the closed inner atomic shells, and valence electrons are characterized by living outside the core. Core electrons have a trend to have a large kinetic energy which means large plane waves are required to describe the oscillatory behavior of their wave functions, and it demands a large number of set of plane waves. This means that describing core electrons asks high cost computing power in practice. Therefore, all-electron plane-wave calculations, which describe both core and valence electrons, demand a huge computational expense that is simply not practical. Fortunately, it is found that variations of the electronic structure of the core-electrons in different chemical environments is negligible, thus allowing problems relating to the core-electrons to be overcome by using an alternative ways such as the introduction of pseudopotential approximation [43].

The current pseudopotential approaches can be traced back to the famous paper written by Phillips and Kleinman [44]. They have shown that it is possible to construct a smooth valence wave function $\tilde{\varphi}_v$ which is not orthogonal to the core states φ_c, by combining the core and the true valance wavefunctions φ_v in the following

way:

$$|\tilde{\varphi}_v\rangle = |\varphi_v\rangle + \sum_c \alpha_{cv}|\varphi_c\rangle. \tag{3.35}$$

Here $\alpha_{cv} = \langle\varphi_c|\tilde{\varphi}_v\rangle \neq 0$. The wave functions satisfying the modified Schrödinger equation

$$\left[\mathcal{H} + \sum_c (\varepsilon_v - \varepsilon_c)|\varphi_c\rangle\langle\varphi_c|\right]|\tilde{\varphi}_v\rangle = \varepsilon_v|\tilde{\varphi}_v\rangle \tag{3.36}$$

are called pseudo-wave functions, where $\mathcal{H} = \hat{\mathcal{T}} + \hat{\mathcal{V}}$, $\hat{\mathcal{V}} = (Z_c/r)\hat{I}$ is the bare nuclear potential, and $\hat{\mathcal{I}}$ is the identity operator. This indicates that one can construct a pseudo-Hamiltonian

$$\mathcal{H}_{\rm PS} = \mathcal{H} + \sum_c (\varepsilon_v - \varepsilon_c)|\varphi_c\rangle\langle\varphi_c| \tag{3.37}$$

with the same eigenvalues of the original Hamiltonian, yet wht much smoother, nodeless wavefunctions near the core of the atoms. The corresponding potential

$$V_{\rm PS} = \frac{Z_c}{r}\hat{\mathcal{I}} + \sum_c (\varepsilon_v - \varepsilon_c)|\varphi_c\rangle\langle\varphi_c| \tag{3.38}$$

is named as a *pseudopotential*. This pseudopotential acts in different ways on wavefunctions when angular momentum is different. Therefore, the form of a pseudopotential should be angular-momentum dependent, and one of the most general forms is as below.

$$V_{\rm PS}(\mathbf{r}) = \sum_{l=0}^{\infty}\sum_{m=-l}^{l} v_{\rm PS}^l(r)|lm\rangle\langle lm| = \sum_{l=0}^{\infty} v_{\rm PS}^l(r)P_l. \tag{3.39}$$

where $\langle\mathbf{r}|lm\rangle = Y_{lm}(\theta,\phi)$ are spherical harmonics, $v_{\rm PS}^l(r)$ is the pseudopotential corresponding to the angular component l, and the operator

$$P_l = \sum_{m=-l}^{l} |lm\rangle\langle lm| \tag{3.40}$$

is a projection operator onto the lth angular momentum subspace.

3.3.1 Norm-conserving pseudopotentials

If the all-electron potential and the pseudopotential are the same outside some radius r_c, which is usually called the *cutoff radius*, then the all-electron and pseudo-wavefunctions are proportional if the corresponding logarithmic derivatives are the same

$$\frac{1}{R^l_{\rm AE}}\left[\frac{dR^l_{\rm AE}(\varepsilon,r)}{dr}\right]_{r_c} = \frac{1}{R^l_{\rm PS}}\left[\frac{dR^l_{\rm PS}(\varepsilon,r)}{dr}\right]_{r_c} \tag{3.41}$$

The proportionality becomes an equality only when the pseudo-wavefunctions is further required to preserve the norm inside the cutoff radius

$$\int_0^{r_c} r^2[R^l_{\rm PS}(\varepsilon,r)]^2 dr = \int_0^{r_c} r^2[R^l_{\rm AE}(\varepsilon,r)]^2 dr \tag{3.42}$$

This property is called *norm-conservation*, and it was first introduced pseudopotentials by Hamann, Schlüter, and Chaing (HSC) [45].

A key result of HSC was to realize that the norm of the wavefunction also appears in a very important identity related to the Friedel sum rule:

$$-\frac{1}{2}\left\{[rR^l(\varepsilon,r)]^2\frac{d}{d\varepsilon}\frac{d}{dr}\ln R^l(\varepsilon,r)\right\}_{r_c} = \int_0^{r_c} r^2[R^l(\varepsilon,r)]^2 dr. \tag{3.43}$$

Therefore, the norm-conservation condition, i.e. the equality of the RHS above for all-electron and pseudo wavefunctions, imposes that, to first-order in the eigenvalue, the logarithmic derivatives of the all-electron and pseudo wavefunctions vary in the same way.

Recently some of the smoothest norm-conserving pseudopotentials are obtained using the recipe by Troullier and Martins [46], who thoroughly studied the convergence properties of the plane wave expansion of the pseudopotential. They generalized Kerker's scheme by proposing the following analytic form of the wavefunction

inside the cutoff radius:

$$R^l_{\rm TM}(r) = r^l \exp(p(r)), \tag{3.44}$$

with $p(r) = c_0 + \sum_{i=2}^{n} c_i r^i$. The r^l behavior for small r is included to avoid a hard-core pseudopotential with a singularity at the origin, which would translate into a large number of plane waves, but it is also physically correct.

3.3.2 Kleinman-Bylander separable form

In 1982, Kleinman and Bylander (KB) developed a fully non-local, separable form of the pseudopotential, $\Delta V^l_{\rm sep}$ [47], by requesting that its action on the reference pseudo wavefunctions be the same as that of the original, HSC semi-local form $\Delta V^l_{\rm PS}$. To this end, they proposed

$$|\zeta^{lm}_{\rm KB}\rangle = |\Delta V^l_{\rm PS}. \tag{3.45}$$

By applying the operator $\Delta V^l_{\rm sep}$ to the reference pseudo wavefunction $\Delta V^l_{\rm PS}$, it is straightforward to prove the requested property, i.e.

$$\Delta V^l_{\rm KB}|\Phi^{lm}_{\rm PS}\rangle = \left[\frac{|\Delta V^l_{\rm PS}\Phi^{lm}_{\rm PS}\rangle\langle\Phi^{lm}_{\rm PS}\Delta V^l_{\rm PS}|}{\langle\Phi^{lm}_{\rm PS}|\Delta V^l_{\rm PS}|\Phi^{lm}_{\rm PS}\rangle}\right]|\Phi^{lm}_{\rm PS}\rangle = \Delta V^l_{\rm PS}|\Phi^{lm}_{\rm PS}\rangle. \tag{3.46}$$

The Kleinman-Bylander projector is then written as

$$\Delta V^l_{\rm KB} = \sum_{m=-l}^{l} E^{lm}_{\rm KB}|\xi^{lm}_{\rm KB}\rangle\langle\xi^{lm}_{\rm KB}|, \tag{3.47}$$

where

$$|\xi^{lm}_{\rm KB}\rangle = \frac{\zeta^{lm}_{\rm KB}}{\langle\zeta^{lm}_{\rm KB}|\zeta^{lm}_{\rm KB}\rangle} \tag{3.48}$$

are normalized projection functions. The strength of the non-locality is determined by the energies E^{lm}_{KB}, which are given by

$$E^{lm}_{\mathrm{KB}} = \alpha_{lm}\langle\Phi^{lm}_{\mathrm{PS}}|(\Delta V^{l}_{\mathrm{PS}})^2|\Phi^{lm}_{\mathrm{PS}}\rangle \tag{3.49}$$

with

$$\alpha_{lm} = \langle\Phi^{lm}_{\mathrm{PS}}|\Delta V^{l}_{\mathrm{PS}}|\Phi^{lm}_{\mathrm{PS}}\rangle^{-1}. \tag{3.50}$$

3.3.3 Projector augmented waves (PAWs) method

The projector augmented wave method is analogous to pseudopotentials in that it introduces projectors acting on smooth valence functions that are the primary objects in the calculation [48, 49]. It also introduces auxiliary localized functions like the "ultrasoft" pseudopotential method. However, the localized functions actually keep all the information on the core states like the orthogonalized plane wave and augmented plane wave methods. Thus many aspects of the calculations are identical to pseudopotential calculations; e.g. all the operations on smooth functions with fast Fourier transforms, generation of the smooth density, *etc.*, are the same.

The linear transformation to the all-electron valence functions $\psi^v = \mathcal{T}\tilde{\psi}^v$ is assumed to be a sum of non-overlapping atom-centered contributions $\mathcal{T} = \mathcal{I} + \sum_{\mathbf{R}} \mathcal{T}_{\mathbf{R}}$, each localized to a sphere denoted Ω_{vecr}. If the smooth wavefunction is expanded in spherical harmonics inside each sphere,

$$|\tilde{\psi}\rangle = \sum_m c_m|\tilde{\psi}_m\rangle, \tag{3.51}$$

with the corresponding all-electron function,

$$|\psi\rangle = \mathcal{T}|\tilde{\psi}\rangle = \sum_m c_m|\psi_m\rangle. \tag{3.52}$$

Hence the full wavefunction in all space can be written

$$|\psi\rangle = |\tilde{\psi}\rangle + \sum_{\mathbf{R}m} c_{\mathbf{R}m}\{|\psi_{\mathbf{R}m}\rangle - |\tilde{\psi}_{\mathbf{R}m}\rangle\}. \tag{3.53}$$

The energy can be written as a sum of three terms,

$$E_{\text{total}} = \tilde{E}_{\text{total}} + E^1_{\text{total}} + \tilde{E}^1_{\text{total}}, \tag{3.54}$$

where $\tilde{E}$ denotes the energy due to the smooth functions evaluated in Fourier space, $\tilde{E}^1$ denotes the same terms evaluated only in the spheres on radial grids, and E^1 the energy in the spheres with the full functions.

3.4 Basis sets

Both wavefunction and density functional methods aim to compute properties of interest without recourse to experimental data. Doing this requires finding the wavefunction. As this is generally unknown, it is usual to expand it in terms of a set of known functions. A single electron wavefunction can be written as

$$\psi_i(\mathbf{r}) = \sum_{j=1}^{\infty} c_j \phi_j(\mathbf{r}), \tag{3.55}$$

where $\phi_j(\mathbf{r})$ are members of a complete set of functions. Obviously it is impossible to use an infinite number of basis functions so the sum in (3.55) is taken over a finite number of functions. This introduces another source of error into the calculations as it is not then possible to describe components of Ψ along the missing functions.

Any family of functions could, in principle, be used as basis functions. Ideally the basis functions should have the same limiting behavior as the real wavefunction, for an isolated atom or molecules they should decay to zero, and they should be computationally inexpensive.

3.4.1 Plane waves

For solids Bloch's theorem prescribes that the wavefunctions must be composed of a phase factor and a periodic part that verifies $u_{\mathbf{k}}(\mathbf{r}) = u_{\mathbf{k}}(\langle + \mathbf{a}_i)$, with $\mathbf{a}_i$ any lattice vector. This can be used to introduce naturally the basis set of plane waves. Plane waves are solutions of the Schrödinger equation in the presence of a constant external potential, as is approximately verified in interstitial regions in solids.

In general, any function in real space can be written as the Fourier transform of a function in reciprocal space,

$$u_{\mathbf{k}}(\mathbf{r}) = \int e^{i\mathbf{g}\cdot\mathbf{r}} \tilde{u}_{\mathbf{k}}(\mathbf{g}) d\mathbf{g}, \tag{3.56}$$

but due to the periodicity of $u_{\mathbf{k}}(\mathbf{r})$, the only allowed values of $\mathbf{g}$ are those that verify $e^{i\mathbf{g}\cdot\mathbf{a}_j} = 1$, i.e. $\mathbf{g}\cdot\mathbf{a}_j = 2n\pi$ for $j = 1, 2, 3$ - three lattice vectors. This implies that $\mathbf{g} = n_1\mathbf{b}_1 + n_2\mathbf{b}_2 + n_3\mathbf{b}_3$, where

$$\mathbf{b}_i = 2\pi \frac{\mathbf{a}_j \times \mathbf{a}_k}{\Omega} \tag{3.57}$$

and $\mathbf{n} = (n_1, n_2, n_3)$ is a vector of integer numbers. Therefore, the $\mathbf{g}$ vectors in the Fourier transform (3.56) are restricted precisely to the reciprocal lattice vectors $\mathbf{G}$, and the general expression for the wavefunction is:

$$\varphi^{(\mathbf{k})}(\mathbf{r}) = \frac{e^{i\mathbf{k}\cdot\mathbf{r}}}{\sqrt{\Omega}} \sum_{\mathbf{G}=0}^{\infty} C_{\mathbf{k}}(\mathbf{G}) e^{i\mathbf{G}\cdot\mathbf{r}}. \tag{3.58}$$

Hence, due to the periodicity, the Fourier transform (3.56) becomes a Fourier series, where the Fourier coefficients are $C_{\mathbf{k}}(\mathbf{G})$. This restriction of the possible values of $\mathbf{g}$ to the reciprocal lattice vectors ensures that periodic boundary conditions are automatically verified. We now define the plane wave basis functions

$$\phi_{\mathbf{G}}(\mathbf{r}) = \frac{1}{\sqrt{\Omega}} e^{i\mathbf{k}\cdot\mathbf{r}}, \tag{3.59}$$

which are suitably normalized in the supercell

$$\langle \phi_{\mathbf{G}} | \phi'_{\mathbf{G}} \rangle = \frac{1}{\Omega} \int_{\Omega} e^{i(\mathbf{G}-\mathbf{G}')\cdot\mathbf{r}} d\mathbf{r} = \frac{1}{\Omega}(\Omega \delta_{\mathbf{G},\mathbf{G}'}) = \delta_{\mathbf{G},\mathbf{G}'} \tag{3.60}$$

so that plane waves corresponding to different wave vectors, $\mathbf{G} \neq \mathbf{G}'$, are orthogonal. With this definition, the wavefunctions for the different eigenstates j can be written as

$$\varphi^{(\mathbf{k})}(\mathbf{r}) = e^{i\mathbf{k}\cdot\mathbf{r}} \sum_{\mathbf{G}=0}^{\infty} C_{j\mathbf{k}}(\mathbf{G}) \varphi_{\mathbf{G}}(\mathbf{r}). \tag{3.61}$$

For the plane wave calculations, we used Vienna *Ab-initio* Simulation Package (VASP) code [50] and Quantum ESPRESSO package [51].

3.4.2 Pseudo-atomic orbital

The use of plane wave basis set has been more general in the solid state physics community. Recently, however, pseudo-atomic orbital (PAO) based method has attracted lots of attention due to its computational efficiency especially combined with the $O(N)$ method algorithm.

Numerical atomic orbitals was designed to represent localized atomic orbitals on numerical grids. These orbitals are obtained from solving radial Schrödinger equation on numerical grids with a confinement boundary condition. This boundary condition enforce a radial cutoff to the real-space extension of numerical orbitals, which guarantees good localization of a basis set. Also numerical optimization scheme on a basis set, which makes small number of basis orbitals from a larger basis set in maintaining the same accuracy, is possible to reduce a computational cost. These properties combined with the pseudopotential scheme lead to high-performance PAO method. For the PAO calculations, we used the SIESTA code [52].

Kohn-Sham orbital ψ_μ is given by the linear combination of atomic orbitals $\phi_{i\alpha}$:

$$\psi_\mu(\mathbf{r}) = \sum_{i\alpha} c_{\mu,i\alpha}\phi_{i\alpha}(\mathbf{r} - \mathbf{r}_i), \tag{3.62}$$

where i is a site index, $\alpha \equiv (plm)$ an collective orbital index, and $\phi_{i\alpha} \equiv Y_{lm}R_{ipl}$. The basis orbitals are eigenstates of the atomic Kohn-Sham equation with a confinement pseudopotential in a semilocal form for each angular momentum quantum number l.

3.5 Computational methods for transport calculations

Understanding transport properties of a solid is one of the most important problems of modern condensed matter physics. In particular, when the system size is smaller than the mean free path of an electron, quantum mechanical analysis for the behaviors of the electron becomes indispensable. There have been diverse methods tackling the problem, and here we briefly introduce *ab initio* transport methods, especially that we have employed in this thesis. In this chapter, we will first briefly introduce the Landauer formalism for conductance. Then we we also briefly introduce the scattering wavefunction matching methods which is one of the early *ab initio* transport methods to calculate scattering probability and scattering wavefunctions.

3.5.1 Landauer formalism

The conductance G of a metallic wire in macroscopic scale is expected to be proportional to the cross-sectional area of the wire A, and inversely proportional to the length L, with the proportional constant being a unique property of the metal,

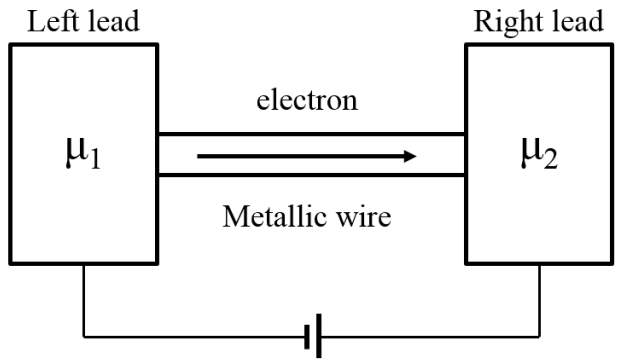

Figure 3.1: Schematic diagram for the two-probe conductance.

called conductivity σ;

$$G = \frac{A}{L}\sigma. \tag{3.63}$$

However, this formula is not valid when the system size becomes smaller so that the length of the wire L becomes much smaller than the mean free path of an electron of the wire. What happens actually is that the conductance becomes quantized in the unit of $2e^2/h$. This phenomenon has been observed in semiconductor [53] , metal nanowires [54], and carbon nanotubes [10]. Here we will provide heuristic argument for the explanation of the phenomena based on the discussion in Ref [55].

Suppose a metallic wire of a mesoscopic size is contacted by left and right leads with the electron chemical potentials μ_1 and μ_2 as shown in Fig. 3.1. Also suppose that there is a small bias applied between two leads, so that $eV = \mu_1 - \mu_2 > 0$. Then the number of electrons moving from the left lead to the right lead through the wire should be greater than those moving in the opposite direction, and the excess left

moving electrons should contributes to the non-vanishing net currents,

$$\begin{aligned} I &= \sum_{i=1}^{M} 2e \frac{(\text{number of states of } i\text{-th band})}{L} \times (\text{velocity of } i\text{-th band}) \\ &= \sum_{i=1}^{M} 2e \int_{\mu_2}^{\mu_1} dE \frac{\mathrm{DOS}_i(E)}{L} \cdot \frac{hk}{m_i} \\ &= \sum_{i=1}^{M} 2e \int_{\mu_2}^{\mu_1} dE \frac{1}{L} \frac{L}{2\pi} \frac{m_i}{\hbar^2 k} \cdot \frac{hk}{m_i} \\ &= \frac{Me}{\pi\hbar}(\mu_1 - \mu_2) = \left(\frac{2e^2}{h} M\right) \frac{\mu_1 - \mu_2}{e} = \left(\frac{2e^2}{h}\right) V = G_0 M V, \end{aligned} \tag{3.64}$$

where M is the number of transverse modes supporting the left to right transport of electrons along the wire direction, and m_i is the effective masses for the i-th transverse mode.

Above argument is all based on the assumption that the wire is not defected. When introduced an defect, an electron moving along the wire can be scattered by the defect and wavefunction describing the quantum state of the electron should be changed from $|\phi_j\rangle$ to $|\psi_j\rangle$ defined in [55].

$$|\psi_j\rangle = |\phi_j\rangle + \frac{\mathcal{H}_1}{E - \mathcal{H}_0} |\phi_j\rangle. \tag{3.65}$$

Here, $\mathcal{H}_0$ and $\mathcal{H}_1$ are pristine (without scatterer) Hamiltonian and perturbation due to the defect, respectively. Suppose z-direction is along the wide direction and the scatterer resides at $z = 0$. In the regions far from the scatterer ($|z| >> \infty$), the wavefunction $\psi_j(\mathbf{r})$ becomes

$$\psi_j(\mathbf{r}) \longrightarrow \sum_i a_{ji} \psi_i^{\mathrm{tr}}(\mathbf{r}) \qquad \text{for } z \to \infty, \tag{3.66}$$

$$\longrightarrow \phi_j^{\mathrm{in}}(\mathbf{r}) + \sum_i b_{ji} \psi_i^{\mathrm{re}}(\mathbf{r}) \qquad \text{for } z \to -\infty. \tag{3.67}$$

Here, $\phi_j^{\rm tr}$ is the transmitted wavefunction and $\phi_j^{\rm re}$ is the reflected wavefunction. The transmission amplitide t_{ij} and the reflection amplitude r_{ij} can be calculated from

$$t_{ij} = \sqrt{\frac{v_i}{v_j}} a_{ij}, \qquad r_{ij} = \sqrt{\frac{v_i}{v_j}} b_{ij}. \tag{3.68}$$

The net current:

$$I_j = \sum_{i=1}^{M} e v_i |a_{ij}|^2 = e v_j \sum_{i=1}^{M} |t_{ij}|^2. \tag{3.69}$$

These lead to the multichannel Landauer-Büttiker formula [56, 57, 58, 59]:

$$G = \frac{I}{V} = \sum_{j=1}^{M} 2 n_j \frac{I_j}{V} = \sum_{j=1}^{M} 2 \left(\frac{e}{\hbar v_j} \right) e v_j \sum_{i=1}^{M} |t_{ij}|^2 \tag{3.70}$$

$$= \frac{2e^2}{h} \mathrm{Tr}[\mathbf{t}^\dagger \mathbf{t}] = G_0 \mathrm{Tr}[\mathbf{t}^\dagger \mathbf{t}]. \tag{3.71}$$

3.5.2 Scattering-state approach for conductance calculation in nanostructures

According to the Landauer formalism, conductance of a nano-meter scale material can be determined by solving a scattering problem and obtaining the associated transmission matrix. In this Section, we present methods to numerically calculate transmission matrix by obtaining self-consistent Hamiltonian matrix element based on *ab initio* scattering-state approach developed in Ref. [1]. Major part of this section is following the analysis presented in Ref. [60]. Before presenting the details, let us first illustrate the geometry that we consider to calculate conductance. Fig. 3.2 shows the schematic geometry for the conductance calculations. The geometry is composed of reservoir, lead, and resistive regions. The reservoirs in the left and right are not actually included in our calculations. They are assumed to supply electrons to the leads attached to them and conceptually maintain chemical potentials of the

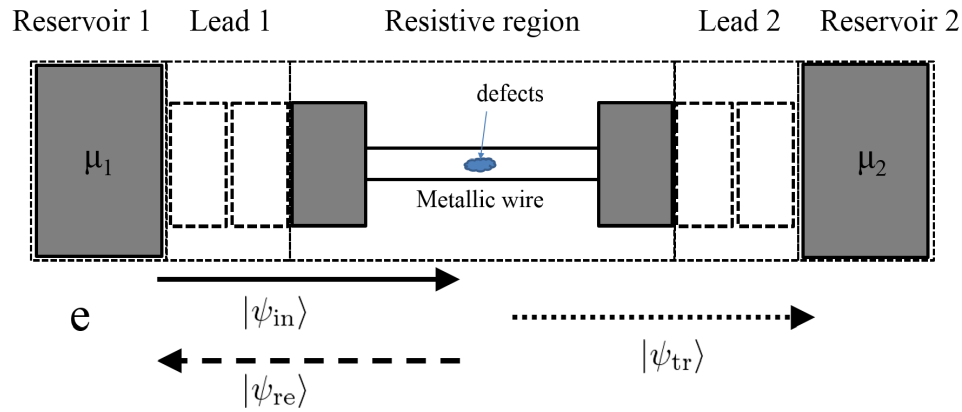

Figure 3.2: Schematic geometry for the two-probe conductance calculation.

leads via thermal equilibrium. The leads regions, described by dotted line in Fig. 3.2, are considered to be periodic, so that they are semi-infinte toward the adjacent reservoir. The resistive region in the middle of the Fig. 3.2 is the region where electrons are actually scattered by defects in the nanomaterial.

Having introduced the geometry for the conductance calculations, now let us discuss how to obtain the complex band structure of the lead regions. In order to calculate conductance of a defected metallic wire, like CNT with a Stone-Wales defect, we first solve the electronic structure of the lead regions imposing periodic boundary condition. Unlike usual electronic structure calculations, we calculate complex band structure so that we can achieve both propagating states and evanescent states, which can be the basis for the scattering wave functions. The complex band structure is calculated in the following manners. Suppose the unit cell of a lead contains $N_{\rm orb}$ and atoms in a unit cell of length L are represented by $\alpha(\beta) = 1, 2, 3, \cdots, N_{\rm orb}$.

From *ab initio* calculations, one may obtain the following Hamiltonian matrix,

$$H^0_{\alpha\beta} \equiv \int \varphi^\dagger_\alpha(\mathbf{r}-m\mathbf{L})\mathcal{H}\varphi_\beta(\mathbf{r}-m\mathbf{L})d\mathbf{r} \tag{3.72}$$

$$H^+_{\alpha\beta} \equiv \int \varphi^\dagger_\alpha(\mathbf{r}-m\mathbf{L})\mathcal{H}\varphi_\beta(\mathbf{r}-(m+1)\mathbf{L})d\mathbf{r} \tag{3.73}$$

$$H^-_{\alpha\beta} \equiv \int \varphi^\dagger_\alpha(\mathbf{r}-m\mathbf{L})\mathcal{H}\varphi_\beta(\mathbf{r}-(m-1)\mathbf{L})d\mathbf{r}, \tag{3.74}$$

and the overlap matrix needed for a nonorthogonal basis set,

$$S^0_{\alpha\beta} \equiv \int \varphi^\dagger_\alpha(\mathbf{r}-m\mathbf{L})\varphi_\beta(\mathbf{r}-m\mathbf{L})d\mathbf{r} \tag{3.75}$$

$$S^+_{\alpha\beta} \equiv \int \varphi^\dagger_\alpha(\mathbf{r}-m\mathbf{L})\varphi_\beta(\mathbf{r}-(m+1)\mathbf{L})d\mathbf{r} \tag{3.76}$$

$$S^-_{\alpha\beta} \equiv \int \varphi^\dagger_\alpha(\mathbf{r}-m\mathbf{L})\varphi_\beta(\mathbf{r}-(m-1)\mathbf{L})d\mathbf{r}. \tag{3.77}$$

Here, $H^0_{\alpha\beta}$ and $S^0_{\alpha\beta}$ represent the Hamiltonian matrix elements and overlap matrix elements between the orbitals in the unit cell, respectively. Also, $H^\pm_{\alpha\beta}$ and $S^\pm_{\alpha\beta}$ represents the matrix elements associated with the adjacent orbitals. If c_α is the coefficient of the scattering wavefunctions defined by

$$\langle\mathbf{r}|\Psi\rangle = \sum_{m=-\infty}^{\infty}\sum_{\beta=1}^{N_{\text{orb}}} c_\beta \mathrm{e}^{i\mathbf{k}\cdot m\mathbf{L}}\varphi_\beta(\mathbf{r}-m\mathbf{L}). \tag{3.78}$$

Then the complex bands can be obtained by solving the Schödinger equation, $\langle\alpha|\mathcal{H}|\Psi\rangle = \langle\alpha|E|\Psi\rangle$ on the basis of Eq. 3.78, i.e.,

$$\sum_{\beta=1}^{N_{\text{ort}}} c_\beta \left[H^0_{\alpha\beta} - ES^0_{\alpha\beta} + \left(H^+_{\alpha\beta} - ES^+_{\alpha\beta}\right)\lambda_E + \left(H^-_{\alpha\beta} - ES^-_{\alpha\beta}\right)\lambda_E^{-1}\right] = 0, \tag{3.79}$$

where $\lambda \equiv \mathrm{e}^{i\mathbf{r}\cdot\mathbf{L}}$. In general the overlap elements between adjacent orbitals $H^\pm_{\alpha\beta}(S^\pm_{\alpha\beta} = 0$, thus making Eq. 3.79 a function of both λ_E and λ_E^{-1}. In order to make the equation linear in λ_E, we define an additional variable

$$c_{N_{\text{orb}}+\gamma} \equiv \lambda_E \sum_{\beta=1}^{N_{\text{orb}}} c_\beta \left(H^+_{\gamma\beta} - ES^+_{\gamma\beta}\right), \tag{3.80}$$

and multiply λ_E in Eq. 3.79. Then, we may arrive the equation

$$\sum_{\beta=1}^{N_{\rm orb}} c_\beta \left[\lambda_E \left(H^0_{\alpha\beta} - ES^0_{\alpha\beta}\right) + H^-_{\alpha\beta} - ES^-_{\alpha\beta}\right] + \sum_{\gamma=1}^{N'} \lambda_E c_{N_{\rm orb}+\gamma} = 0 \tag{3.81}$$

with N' defined by the number of nonzero elements of $H^{\pm}_{\alpha\beta}(S^{\pm}_{\alpha\beta})$. In this way we may have a secular equation which is linear in λ_E, which describes both propagating and evanescent modes.

Having introduced the equation for complex band structure of the leads, we now turn to the scattering-state approach to calculate conductance using localized basis [1]. Suppose $\varphi^1_\alpha(\mathbf{r})$ and $\varphi^2_\beta(\mathbf{r})$ represent the orbitals in the left lead (lead 1 in Fig. 3.2) and the right lead (lead 2 in Fig. 3.2), respectively where $\alpha = 1, \cdots, N_1$ and $\beta = 1, \cdots N_2$. Also assume that $\varphi^0_l(\mathbf{r})$ with $l = 1, \cdots, N_0$. If the resistive region includes enough number of lead unitcells, the Hamiltonian matrix for both leads can be written as

$$H^0_{1(2);\alpha\beta} \equiv \int \varphi^{1(2)\dagger}_\alpha(\mathbf{r} - m\mathbf{L})\mathcal{H}\varphi^{1(2)}_\beta(\mathbf{r} - m\mathbf{L})d\mathbf{r} \qquad (m = 1, 2, \cdots) \tag{3.82}$$

$$H^+_{1(2);\alpha\beta} \equiv \int \varphi^{1(2)\dagger}_\alpha(\mathbf{r} - m\mathbf{L})\mathcal{H}\varphi^{1(2)}_\beta(\mathbf{r} - (m+1)\mathbf{L})d\mathbf{r} \qquad (m = 0, 1, \cdots) \tag{3.83}$$

$$H^-_{1(2);\alpha\beta} \equiv \int \varphi^{1(2)\dagger}_\alpha(\mathbf{r} - m\mathbf{L})\mathcal{H}\varphi^{1(2)}_\beta(\mathbf{r} - (m-1)\mathbf{L})d\mathbf{r} \qquad (m = 1, 2, \cdots) \tag{3.84}$$

where $\mathcal{H}$ is the Hamiltonian for the lead part as defined previously. Also, the overlap matrix can be written as

$$S^0_{1(2);\alpha\beta} \equiv \int \varphi^{1(2)\dagger}_\alpha(\mathbf{r} - m\mathbf{L})\varphi^{1(2)}_\beta(\mathbf{r} - m\mathbf{L})d\mathbf{r} \qquad (m = 1, 2, \cdots) \tag{3.85}$$

$$S^+_{1(2);\alpha\beta} \equiv \int \varphi^{1(2)\dagger}_\alpha(\mathbf{r} - m\mathbf{L})\varphi^{1(2)}_\beta(\mathbf{r} - (m+1)\mathbf{L})d\mathbf{r} \qquad (m = 0, 1, \cdots) \tag{3.86}$$

$$S^-_{1(2);\alpha\beta} \equiv \int \varphi^{1(2)\dagger}_\alpha(\mathbf{r} - m\mathbf{L})\varphi^{1(2)}_\beta(\mathbf{r} - (m-1)\mathbf{L})d\mathbf{r} \qquad (m = 1, 2, \cdots) \tag{3.87}$$

A scattering wavefunction in the resistive region with proper boundary condition for incoming channels can be written as

$$\begin{aligned}
\langle \mathbf{r}|\Psi\rangle &= \sum_{n=0}^{\infty}\sum_{\alpha=1}^{N_1} c^1_{n\alpha} \mathrm{e}^{i\mathbf{k}\cdot n\mathbf{L}_1}\varphi^1_\alpha(\mathbf{r}-n\mathbf{L}_1) && (3.88)\\
&+ \sum_{m=1}^{\infty}\sum_{\beta=1}^{N_2} c^2_{m\beta} \mathrm{e}^{i\mathbf{k}\cdot m\mathbf{L}_2}\varphi^2_\beta(\mathbf{r}-m\mathbf{L}_2) + \sum_{l=1}^{N_0} c^0_l\varphi^0_l(\mathbf{r}) && (3.89)\\
&= \langle \mathbf{r}|\psi_{\mathrm{in}}\rangle + \sum_{p=1}^{N_1^{\mathrm{b}}} r_p\langle \mathbf{r}|\psi^p_{\mathrm{re}}\rangle + \sum_{q=1}^{N_2^{\mathrm{b}}} t_q\langle \mathbf{r}|\psi^q_{\mathrm{tr}}\rangle + \langle \mathbf{r}|\psi_{\mathrm{sc}}\rangle, && (3.90)
\end{aligned}$$

where

$$\begin{aligned}
\langle \mathbf{r}|\psi_{\mathrm{in}}\rangle &= \sum_{n=1}^{\infty}\sum_{\alpha=1}^{N_1} c^{\mathrm{in}}_\alpha \mathrm{e}^{i\mathbf{k}\cdot n\mathbf{L}_1}\varphi^1_\alpha(\mathbf{r}-n\mathbf{L}_1) + \sum_{\alpha'\in\mathbb{B}_1} c^{\mathrm{in}}_{\alpha'}\varphi^1_{\alpha'}(\mathbf{r}) && (3.91)\\
\langle \mathbf{r}|\psi^p_{\mathrm{re}}\rangle &= \sum_{n=1}^{\infty}\sum_{\alpha=1}^{N_1} c^{\mathrm{re}}_{p,\alpha} \mathrm{e}^{i\mathbf{k}_p\cdot n\mathbf{L}_1}\varphi^1_\alpha(\mathbf{r}-n\mathbf{L}_1) + \sum_{\alpha'\in\mathbb{B}_1} c^{\mathrm{re}}_{p,\alpha'}\varphi^1_{\alpha'}(\mathbf{r}) && (3.92)\\
\langle \mathbf{r}|\psi^q_{\mathrm{tr}}\rangle &= \sum_{n=1}^{\infty}\sum_{\beta=1}^{N_2} c^{\mathrm{tr}}_{q,\beta} \mathrm{e}^{i\mathbf{k}_q\cdot m\mathbf{L}_2}\varphi^2_\beta(\mathbf{r}-m\mathbf{L}_2) + \sum_{\beta'\in\mathbb{B}_2} c^{\mathrm{tr}}_{q,\beta'}\varphi^2_{\beta'}(\mathbf{r}) && (3.93)\\
\langle \mathbf{r}|\psi_{\mathrm{sc}}\rangle &= \sum_{\alpha\in\mathbb{B}_1^c} c^1_\alpha\varphi^1_\alpha(\mathbf{r}) + \sum_{\beta\in\mathbb{B}_1^c} c^2_\beta\varphi^2_\beta(\mathbf{r}) + \sum_{l=1}^{N_0} c^0_l\varphi^0_l(\mathbf{r}), && (3.94)
\end{aligned}$$

where $\mathbf{k}_{\mathrm{in}}$ is real, $\mathbf{k}_{\mathrm{in}}\cdot\mathbf{L}_1$ is negative, $\Re\mathbf{k}_p\cdot\mathbf{L}_1$ and $\Im\mathbf{k}_p\cdot\mathbf{L}_1$ are positive, and $\Re\mathbf{k}_p\cdot\mathbf{L}_2$ and $\Im\mathbf{k}_p\cdot\mathbf{L}_2$ are also positive. In the above formula, we chose only a single right-moving incident channel for simplicity. N_1^b and N_2^b represent the number of boundary orbitals of the repeating unit in the left and right leads, respectively. $N_{1(2)}$ represents the number of whole orbitals in lead 1 (2). $\mathbb{B}_{1(2)}$ denotes the set of boundary orbitals in the lead 1 (2). Note that $n(\mathbb{B}_{1(2)}) = N^b_{1(2)}$. Then, we may have the following

$N_0 + N_1 + N_2$ equations

$$\int \varphi_\alpha^1(\mathrm{r}) \left(\mathcal{H}_{\mathrm{tot}} - E(\mathbf{k})\right) \langle \mathbf{r}|\Phi\rangle d\mathbf{r} = 0, \tag{3.95}$$

$$\int \varphi_\alpha^2(\mathrm{r}) \left(\mathcal{H}_{\mathrm{tot}} - E(\mathbf{k})\right) \langle \mathbf{r}|\Phi\rangle d\mathbf{r} = 0, \tag{3.96}$$

$$\int \varphi_l^0(\mathrm{r}) \left(\mathcal{H}_{\mathrm{tot}} - E(\mathbf{k})\right) \langle \mathbf{r}|\Phi\rangle d\mathbf{r} = 0, \tag{3.97}$$

where $\mathcal{H}_{\mathrm{tot}}$ is the Hamiltonian for the whole system. Now, we left to determine $N_0 + (N - N_1^b) + N - N_2^b)$ coefficients for the orbitals and $N_1^b + N_2^b$ coefficients for outgoing propagating or evanescent states, which can be done by standard matrix algebra. In this way, we can calculate the trace of transmission matrix and by dint of the Landauer's formula, thus conductance of manomaterials in *ab initio* level.

3.6 Berry curvature and Hall conductivity calculations on numerical grids

In 2005, C. Kane and E. Mele published a seminal paper proposing an new quantum phase named quantum spin Hall (QSH) [61]. A QSH insulator is characterized by spin-polarized conducting states localized at the sample edges without an applied magnetic field in an otherwise insulating bulk. This exotic phase can be rigorously identified by calculating spin Hall conductivities which is non-vanishing when the system is QSH insulator. Later, there have been great interest in classifying materials into diverse quantum topological phases, and numerical methods to calculate topological invariants, such as quantum spin Hall conductivity, has become an important task. In this Chapter, we will briefly review a numerical method to calculate the Berry curvature and (spin) Hall conductivity on discretized BZ. Our discussion

is based on Ref. [32], which is widely used due to its efficiency.

The Berry curvature for Bloch states is defined by

$$\Omega_n(\mathrm{k}) \equiv i\langle\nabla_{\mathbf{k}} u_{n\mathbf{k}}| \times |\nabla_{\mathbf{k}} u_{n\mathbf{k}}\rangle, \tag{3.98}$$

where $u_{n\mathbf{k}}$ is the Bloch cell function in n-th band. Then the Hall conductivity in a 2D system is an integration over the BZ [62],

$$\sigma_{xy}^{H} = -\frac{e^2}{\hbar}\int_{\mathrm{BZ}} \frac{d^2k}{(2\pi)^2}\Omega^z(\mathbf{k}). \tag{3.99}$$

In the presence of degenerate bands, the definition of the Berry curvature needs to be extended to the non-Abelian Berry curvature tensor [63],

$$\begin{aligned}\Omega_{ij}(\mathbf{k}) &= i\langle\nabla_{\mathbf{k}} u_i(\mathbf{k})| \times |\nabla_{\mathbf{k}} u_j(\mathbf{k})\rangle \\ &- i\sum_{l\in\Sigma}\langle\, u_i(\mathbf{k})|\nabla_{\mathbf{k}} u_j(\mathbf{k})\rangle \times \langle\, \nabla_{\mathbf{k}} u_l(\mathbf{k})|u_j(\mathbf{k})\rangle,\end{aligned} \tag{3.100}$$

where $\Sigma = \{1, \cdots, N\}$ contains all indices of the degenerate bands. In this non-Abelian case (degenerate multibands case), the Hall conductivity can be obtained by

$$\sigma_{xy}^{H} = -\frac{e^2}{\hbar}\int_{\mathrm{BZ}} \frac{d^2k}{(2\pi)^2}\mathrm{tr}d\boldsymbol{\Omega}(\mathbf{k}). \tag{3.101}$$

The previously introduced first-principles methods can generate Bloch wavefunctions and, in principle, the Hall conductivities can be calculated from those Bloch wavefunctions. However, in practical calculations, due to the numerical random phases generated at different $\mathbf{k}$-point, serious problems may arise associated with convergence with respect to the number of $\mathbf{k}$-grids on BZ. One may tackle this problem by fixing gauge condition, but according to our experience it did not improve the situation that much. The most important point to overcome this problem is to

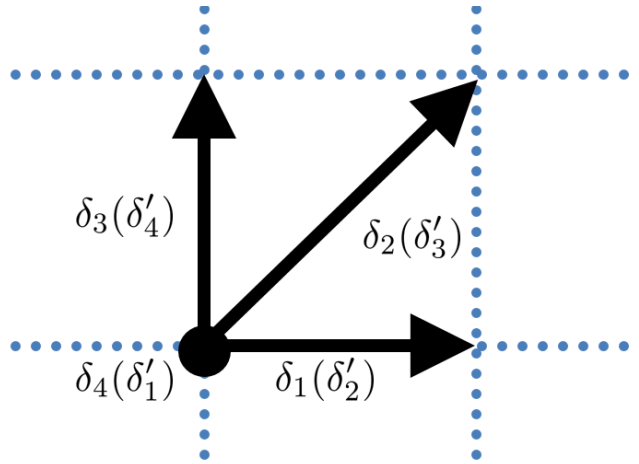

Figure 3.3: Schematic view of numerical grid. $\delta_4 = \delta'_1 = 0$, $\delta_1 = \delta'_2$, $\delta_2 = \delta'_3$, and $\delta_3 = \delta'_4$

calculate the curl by actually circling around a single grid. This is the heart of the prescription of Ref. [32]. In the literature, the Hall conductivity is obtained by

$$\sigma_{xy}^{H} = \frac{1}{2\pi} \sum_{\mathbf{k}} \Im \ln \prod_{i=1}^{4} \det \langle u_i(\mathbf{k} + \delta_{\mathbf{i}}) | u_j(\mathbf{k} + \delta'_{\mathbf{i}}) \rangle, \tag{3.102}$$

where δ_i and δ'_i are vectors connecting adjacent grid points enclosing a single mesh as defined in Fig. 3.3 The adjacent vectors make it sure that the curl is circling around a mesh so that the numerical random phases cancel in a mesh. In Fig 3.4 we present the Berry curvature $\Omega(\mathbf{k})$ defined by

$$\Omega(\mathbf{k}) = \Im \ln \prod_{i=1}^{4} \det \langle u_i(\mathbf{k} + \delta_{\mathbf{i}}) | u_j(\mathbf{k} + \delta'_{\mathbf{i}}) \rangle \tag{3.103}$$

for silicene under an applied perpendicular electric field near a K point.

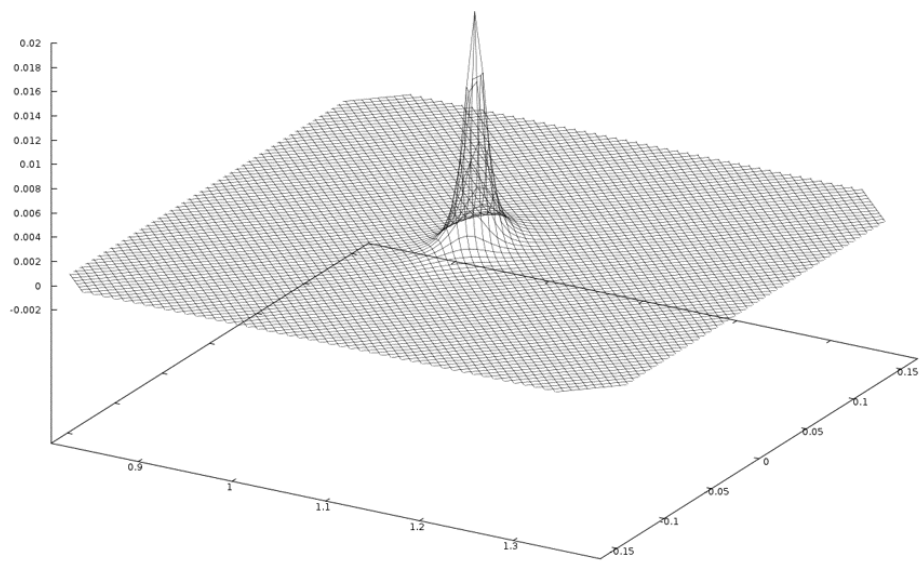

Figure 3.4: Example of berry curvature obtained from first-principles calculations performed in silicene under an applied perpendicular electric field of 0.5 eV near a zone corner.

CHAPTER 4

Carbon nanotube with a Stone-Wales defect: emergence of loop currents

In metallic carbon nanotubes with defects, the electric current flow is expected to have characteristic spatial patterns depending on the nature of the defects. By performing first-principles transport calculations, we find that current-density loops occur around the defects in carbon nanotubes at energies near conductance dips caused by the resonant backscatterings. The loops have opposite directions above and below the dip centers and disappear exactly at the dip centers, originating from the interference of conducting states and quasibound states. Induced magnetic fields penetrate the tube surface in the near-field region and decay in the far-field region like a magnetic dipole. We show that, with a time-modulated gate-voltage,

the system behaves as a nano-scale antenna and produces oscillating magnetic fields, thereby making experimental detections of the defects feasible.

4.1 Introduction

The transport of electrons in nanostructures is essentially a quantum mechanical phenomenon. In a defect-free nanometer-scale system at low temperatures, electrons can flow ballistically as matter waves [64]. Since electronic wavefunctions have three-dimensional (3D) extent in nature, the spatial distribution of currents even in quasi 1D nanostructures may have various 3D features potentially useful for novel electronic devices. Recently, 3D current densities and their induced phenomena have been investigated in nanoscale systems such as C_{60} molecular bridges [65], carbon nanotubes (CNTs) [66, 67], and graphene nanoribbons [68, 69].

In C_{60} molecular bridges, local rotations in the current density are predicted theoretically, being related to degenerate molecular levels, and the direction of the induced magnetic moment is found to be reversed as the electron energy is swept across the molecular levels [65]. In graphene nanoribbons, loop currents occur around nonlocal topological defects or local adatom defects, and they are suggested to originate from the interference among transport channels [68, 69]. In these studies [65, 68, 69], loop currents and induced magnetic moments are found to appear; however, their generation mechanism and energy dependence are yet to be understood.

In the case of CNTs, local currents are studied with B and N impurities [67], and induced magnetic moments are studied with Stone-Wales defects [66], but these studies are not focused on defect-induced loop currents. Since CNTs are a prototypical quasi-1D nanostructure and an important candidate for nano-electronic de-

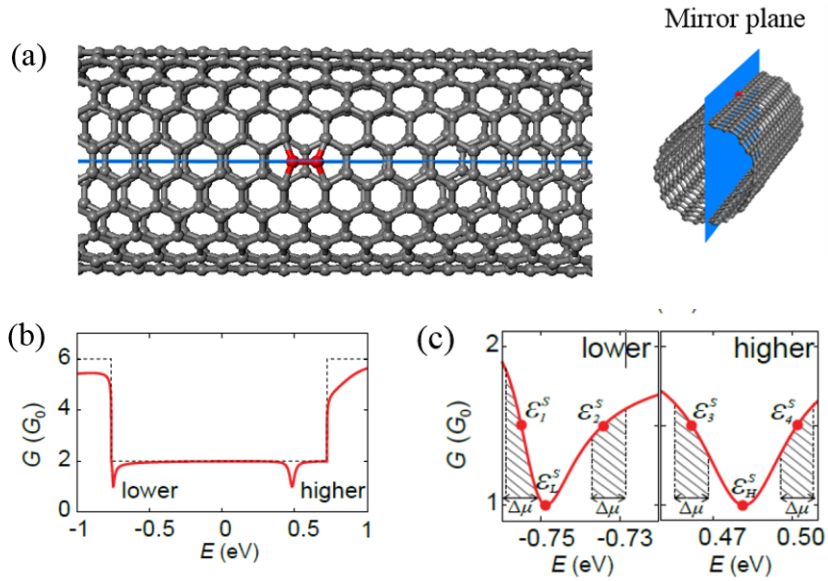

Figure 4.1: Atomic geometries (a) and quantum conductance G (b) of (10, 10) CNTs with a symmetric Stone-Wales defect (SSW), respectively. (c) shows an enlarged view of the conductance dips in (b). The dip positions -0.75 and 0.48 are marked with ε_L^S and ε_H^S, respectively. The energies of -0.755, -0.734, 0.462, and 0.502, where $G = 1.5G_0$, are marked with ε_1^S, ε_2^S, ε_3^S, ε_4^S, respectively. In (c), $\Delta\mu$'s indicate energy windows for calculating current-induced magnetic fields shown in Fig. 4.6.

vices, first-principles study on defect-induced loop currents in CNTs will provide fundamental understanding on locally rotating current densities potentially useful for novel material characterizations or device applications.

In this Chapter, we consider metallic (10,10) CNTs with a symmetric Stone-Wales defect (SSW) respecting the mirror symmetry with respect to the mirror symmetry with respect to the plane intersecting the defect and the tubular axis, and perform first-principles transport calculations. It is shown below that current-density loops emerge around the defects, with their maximum magnitudes much greater than the axial current densities. The loop directions are found to be reversed

at defect-induced conductance dips, revealing that the loop currents are generated by the interference of conducting states and quasibound defect states. Induced dipole-like magnetic fields depend sensitively on the Fermi level.

4.2 Computational details

Figure 4.1 (a) shows a defective CNT studied in the present work. We introduce a SSW to a (10,10) metallic CNT in a supercell of 15.0 Å long to isolate the defect and we relax the positions of all 240 atoms in the supercell using the density functional theory (DFT) with the local density approximation. Then, infinitely-long defect-free CNTs are seamlessly attached to the left and right sides of the defective region [1]. In DFT calculations, non-local norm-conserving pseudopotentials [70, 71] are employed and electronic wavefunctions are expanded with pseudo-atomic orbitals (double-zeta polarization basis set) [72].

Figure 4.1 (b) shows the electronic conductance spectra $G(E)$ in units of the conductance quantum $G_0 = 2e^2/h \approx (12.9k\Omega)^{-1}$ through a single defect in CNTs obtained by the first-principles scattering-state method for quantum conductance [1]. The conductance $G(E)$ shows two dips at 0.75 eV below and 0.48 eV above the Fermi energy, respectively. The dips are arise due to the scattering of an electron in a conducting channel to a quasibound state in the corresponding energy [1, 73, 74, 75]. Only the π^* (π) states are scattered and completely blocked at the lower (higher) dip due to the mirror symmetry [75].

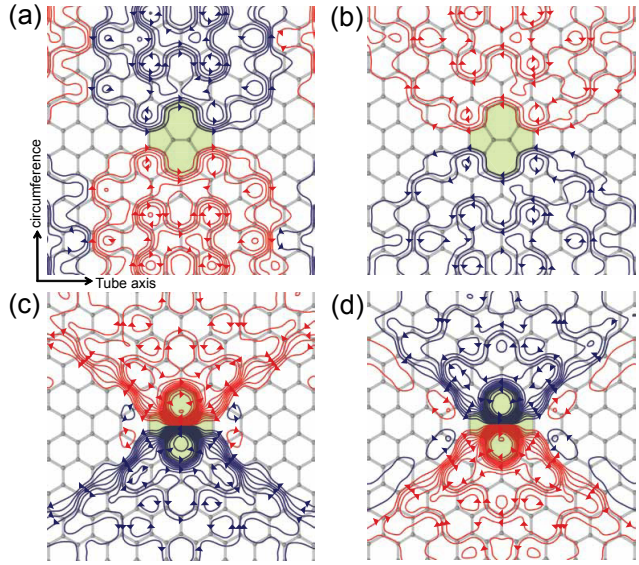

Figure 4.2: Electrical current distributions $\mathbf{J}_n(\mathbf{r};E)$ in the (10, 10) CNT with SSW at energies E of (a) ε_1^S, (b) ε_2^S, (c) ε_3^S, and (d) ε_4^S marked in Fig. 1(e) for $G = 1.5G_0$. (a) and (b) are for the π^* band incident from the left, and (c) and (d) are for the π band. In (a)-(d), $\mathbf{J}_n(\mathbf{r};E)$ is integrated radially from 0.4 to 1.0 nm, and then plotted in an arbitrary unit. The arrows indicate the direction of the current. Color scheme is introduced to represent the intensity.

4.3 Results and Discussion

4.3.1 Current-density distribution

We calculate the current-density distribution using

$$\mathbf{J}_{nk}(\mathbf{r}) = \frac{-|e|\,\hbar}{m_e}\mathrm{I}m[\psi^*_{nk}(\mathbf{r})\nabla\psi_{nk}(\mathbf{r})] + \mathbf{J}_{\mathrm{N}L,nk}(\mathbf{r}) \tag{4.1}$$

for a scattering state $\psi_{nk}(\mathbf{r})$ of an incident electron of wavevector $\mathbf{k}$ in the nth band. Because of the nonlocal pseudopotentials used here, we need an additional term, $\mathbf{J}_{\mathrm{N}L,nk}(\mathbf{r})$ which satisfies a Poisson-like equation inside each cut-off radius of pseudopotentials and is zero elsewhere as previously described [76]. We define the

current density per energy of the nth band at the energy E as

$$\mathbf{J}_n(\mathbf{r}; E) = 2\sum_k \mathbf{J}_{nk}(\mathbf{r})\delta(E - E_{nk}), \tag{4.2}$$

where the factor of 2 counts spin degeneracy, E_{nk} is the band structure in the perfect CNT, and the summation includes incident states from the *left* only. If a small bias voltage is applied to make the chemical potentials on the left and the right of the defect (μ_L and μ_R) different by $\Delta\mu = \mu_L - \mu_R > 0$, the net current density $\mathbf{J}(\mathbf{r})$ is

$$\mathbf{J}(\mathbf{r}) = \sum_n \int_{\mu_\mathrm{R}}^{\mu_\mathrm{L}} \mathbf{J}_n(\mathbf{r}; E)dE. \tag{4.3}$$

We find that current-density loops appear near the SSW at the energy near the conductance dips (Fig. 4.2). The loops are generated by the scattering state of the π^* (π) band near the lower (higher) dip, which are most pronounced when $G(E) = 1.5G_0$, i.e., at ε_1^S, ε_2^S, ε_3^S, and ε_4^S marked in Fig. 4.1(e). The maximum amplitudes of $\mathbf{J}_n(\mathbf{r}; E)$ near the defect are 2.0 mA/nm^2/eV at ε_1^S and 12.0 mA/nm^2/eV at ε_3^S. These are significantly large values corresponding to 5 and 30 times the maximum value of 0.4 mA/nm^2/eV in the pristine CNT, respectively. Near the lower dip, the loop currents are rather broad around the defect [Figs. 4.2(a) and (b)], but they are more concentrated close to the defect near the higher dip [Figs. 4.2(c) and (d)]. This is consistent with the fact that quasibound states are more localized at the higher dip [75]. Meanwhile, scattering of the π band near the lower dip and the π^* band near the higher dip are negligible, thus producing no loop current.

4.3.2 Energy dependence of the loop-current

Loop-current directions are found to be reversed as the energy E passes through the conductance dips at ε_L^S and ε_H^S (Fig. 4.2). When an electron in the π^* band

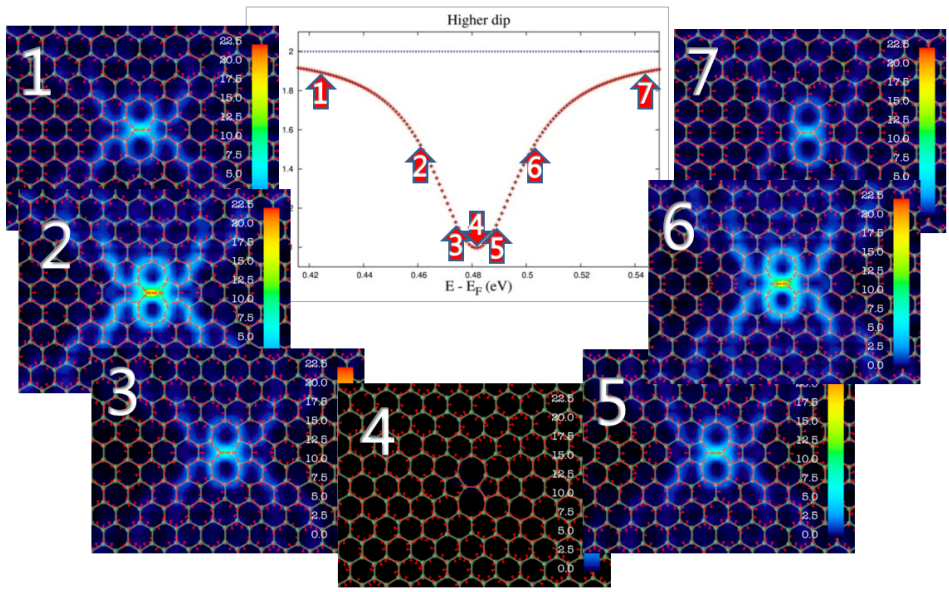

Figure 4.3: Energy dependence of the intensities of the current densities $|\mathbf{J}_n(\mathbf{r}; E)|$ in the (10, 10) CNT with SSW at energies E. Brighter color indicates higher intensity of current densities. The current densities are drawn at the energies indicated by arrows with the corresponding number in the conductance plot (middle panel). The intensity of the current densities are maximized at the half transmissions for the scattered channel at 2 and 6, ($G(E) = 1.5G_0$) and gradually disappears as the energy of the incident electrons approaches to 4 ($G(E) = 1.0G_0$). The energies indicated by 1, 3, 5, and 7 correspond to (E) $= 1.9G_0$, $G(E) = 1.9G_0$, $G(E) = 1.9G_0$, and $G(E) = 1.9G_0$, respectively.

is incident from the left at ε_1^S, the current loops are clockwise in the lower half-plane and counter-clockwise in the upper half-plane [Fig. 4.2(a)], and they have the opposite sense at ε_2^S [Fig. 4.2(b)]. This reversal is also clear near ε_H^S [Figs. 4.2(c) and (d)]. As the reversal occurs continuously in energy, loop currents disappear exactly at the dips (ε_L^S and ε_H^S). As shown in Fig. 4.3 we also find the energy dependence of the intensities of the current densities $|\mathbf{J}_n(\mathbf{r}; E)|$. It is found that the intensity becomes maximized at $G(E) = 1.5G_0$ (2 and 6 in Fig. 4.3), and gradually dimmed

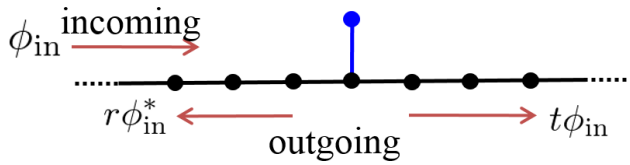

Figure 4.4: Schematic diagram of a 1D conducting channel interacting with a defect state.

as the energy E approaches to E_0 where $G(E_0)=1.0G_0$ (4 in Fig. 4.3).

The loop-current reversal at the conductance dips can be understood as an abrupt phase change of the transmission coefficient by 180° as the energy passes to the resonance energy [77, 78] (Fig. 4.5. When an incident state ϕ_i in a single-channel system couples to a non-degenerate defect state ϕ_b, the scattering state ψ_{sc} is $\psi_{sc} = \phi_i + r\phi_i^* + c_b\phi_b$ in the reflected region and $\psi_{sc} = t\phi_i + c_b\phi_b$ in the transmitted region (Fig. 4.5). Here, ϕ_i^* is the complex conjugate of ϕ_i, r and t are reflection and transmission coefficients, respectively, and c_b is the coefficient of ϕ_b. Near a resonance energy E_0, t and c_b can be described by the Breit-Wigner formula [79],

$$t \cong \frac{E - E_0}{(E - E_0) + i\Gamma/2}, \; c_b \propto \frac{1}{(E - E_0) + i\Gamma/2}, \tag{4.4}$$

where Γ is the half-width of the resonance dip, proportional to the coupling between ϕ_i and ϕ_b. Using that ϕ_b can be represented with a real function and that $|r|^2+|t|^2 = 1$, the current density of ψ_{sc} is given by

$$\mathbf{J}_{sc} = \frac{-|e|\hbar}{m_e}\text{Im}\left\{|t|^2\phi_i^*\nabla\phi_i + tc_b^*(\phi_b\nabla\phi_i - \phi_i\nabla\phi_b)\right\}, \tag{4.5}$$

where the first term is simply an axial current while the interference term of ϕ_i and ϕ_b may have current-density loops. As a complete backscattering ($t = 0$) occurs at E_0, the sign of t changes but c_b remains almost the same, changing the sign of the

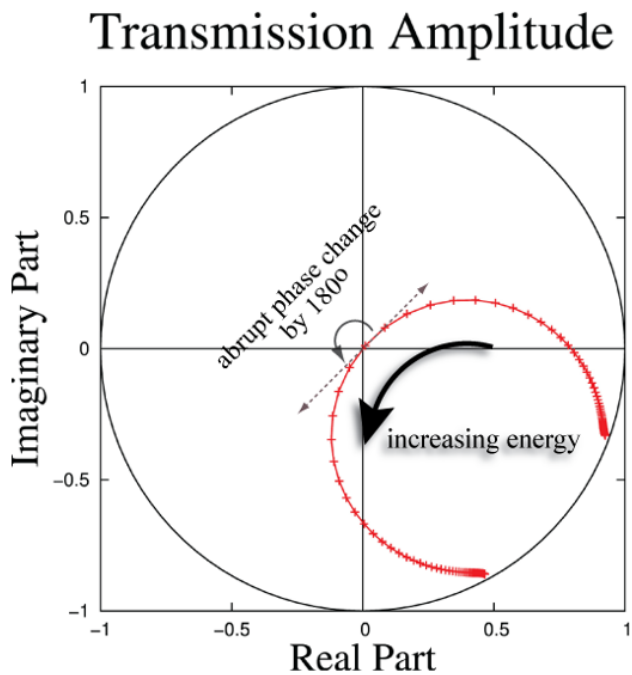

Figure 4.5: Transmission amplitude as a function of the Fermi energy $t(E)$ obtained from *ab initio* calculations (lower dip). As the Fermi energy approaches to that of zero-transmission transmission amplitude approached to the origin, i.e., zero. By passing through the zero-transmission energy, the phase of the transmission amplitude is abruptly changed by 180°, indicating that the defect state becomes an occupied state.

interference term. This explains the loop-current reversal at the conductance dips in the defective CNT as well as in other systems such as C_{60} and graphene [65, 68, 69] where the current-density reversal has been reported computationally but the origin of the reversal has not been recognized clearly. Such a directional reversal is generally expected in systems showing zero transmission due to a resonance [80, 81].

The occurrence of the maximum loop current at $G(E) = 1.5G_0$ in the CNT with the SSW can also be explained from above argument. Since the function $\phi_b \nabla\phi_i - \phi_i \nabla\phi_b$ in Eq. (5) varies slowly in E, the factor tc_b^* determines the loop-current

amplitude. As $|tc_b^*| \propto |E-E_0|/[(E-E_0)^2+\Gamma^2/4]$, the maximum occurs at $E=E_0\pm\Gamma/2$ where the transmission $|t|^2=0.5$. This corresponds to $G=1.5G_0$ in the CNT with the SSW because there exists another band which is not reflected and contributes $1G_0$ to the conductance.

4.3.3 Induced magnetic fields

From the electrical current density around the defect, we can calculate induced magnetic fields using the Biot-Savart law. The resulting magnetic field has two parts: a coaxial part surrounding the CNT induced by the axial current along the tube and a dipole-like part from the local loop currents. Since loop currents of opposite directions are formed on the upper and lower half-planes from the SSW (Fig. 2), one might expect a quadruple field rather than a dipole field. However, due to the tubular curvature, the magnetic dipole moments on the upper and the lower half-planes are not exactly antiparallel; thus, a nonzero net dipole moment persists which is larger for a smaller-diameter CNT.

The induced dipole-like magnetic field is obtained by subtracting the coaxial magnetic field from the total field. As shown in Figs. 3(c) and (d), the dipole-like feature in the field is more pronounced near ε_H^S, where the maximum strength at the near field is about 30 gauss in the vicinity of the defect. We note that a finite magnetic field ($\sim$10 gauss) is also present inside the tube. The directions of the magnetic fields in Figs. 3(a) and (c) are opposite to those in Figs. 3(b) and (d), respectively, because of the loop-current reversal at each conductance dip. The direction of the coaxial part of the magnetic field remains unchanged as a function of energy.

For further analysis, we estimate the magnetic dipole moment ($\frac{1}{2}\int \mathbf{r}\times\mathbf{J}(\mathbf{r})dr^3$) as a function of energy near the two conductance dips [Fig. 3(e)]. The resulting dipole moment is along the circumference at the defect, and its direction is reversed at the energies of the two conductance dips, with the maximum magnitude of $0.05\mu_B$ and $0.08\mu_B$ near the lower and higher dips, respectively. From these results, we also expect that an oscillating magnetic dipole moment can be generated by applying a time-modulated gate voltage near one of the two dips, and the system effectively behaves as a dipole antenna. It may be regarded as a signature of a defect in a CNT and used to identify the defect. In the present case, a direct measurement requires at least a sensitivity of about 0.5×10^{-9} of the flux quantum ($\Phi_0 = hc/e$) with spatial resolution of 0.3 nm^2, corresponding to the sensitivity of measuring a tenth of a single-electron spin [Fig. 3(e)]. It is somewhat beyond the capability of the current nano-scale magnetometer techniques [82], such as superconducting quantum interference device [83, 84], magnetic resonance force microscopy [85], and magnetic sensing techniques based on diamond spins [86]; however, since rapid progress is being made in measuring weak magnetic fields with high spatial resolutions, detecting the defect-induced magnetic dipole may be possible in the near future. Alternatively, one may as well use the defected CNT as a probing tip of the magnetic force microscopy.

4.4 Summary and Concluding Remark

In summary, we have presented local current densities and induced magnetic fields in CNTs with SSW using the first-principles calculations. In the defected CNT, electrical current-density loops appear near the SSW at energies close to the conduc-

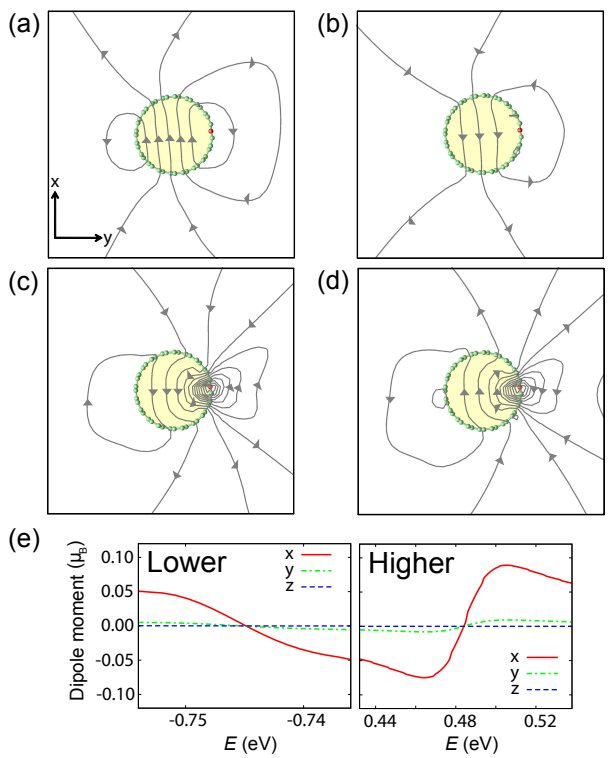

Figure 4.6: Dipole-like part of the magnetic field around the CNT with SSW induced by the current density $\mathbf{J}(\mathbf{r})$ of Eq. (3) when its energy windows are centered at (a) ε_1^S, (b) ε_2^S, (c) ε_3^S, and (d) ε_4^S as marked in Fig. 1(e) and its width $\Delta\mu$ is 10 meV. (a)-(d) are drawn on the plane normal to the tube axis at the defect denoted in red. Each flux line represents 6 gauss·Å^2. (e) shows the Cartesian components of the induced magnetic dipole moment when the energy window for $\mathbf{J}(\mathbf{r})$ is from $E - \frac{1}{2}\Delta\mu$ to $E + \frac{1}{2}\Delta\mu$. In the left (right) panel, E is near the lower (higher) conductance dip. The x and y axes are shown in (a) while the z axis is along the tube.

tance dips, and the reversal of loop-current directions appears as the electron energy passes through the defect levels. We found that the loop currents are generated due to the interference between propagating states and quasibound states, and these loop currents can be used to generate dipole-like magnetic fields. We expect that the energy-dependent reversal of the loop currents can be experimentally exploited by time-modulated gate voltage generating oscillating magnetic dipole moments. We alos found that these features are expected not only in the CNT with the SSW but also in any system supporting a single transport channel interacting with a defect state. For example, we have found that similar features in a CNT with a asymmetric Stone-Wales defect except that the loop currents are distributed asymmetrically which is due to the absence of the mirror symmetry.

CHAPTER 5

Graphene with a divacancy: dynamics and stability

A Divacancy (DV) is one of the most abundant and important defects in graphene, which modifies the electronic and chemical properties of graphene. In this chapter, we present ab initio calculations to study the dynamics and stability of DVs in graphene. DVs in graphene have various reconstructed structures, such as triple pentagon-triple heptagon (555-777) and pentagon-octagon-pentagon (5-8-5) patterns. A direct observation of the structural transformations between these reconstructions was recorded in transmission electron microscope (TEM) images reported by Girit et al. [2]. We clarify the atomic structures of DVs observed in the experiment and investigate the atomic processes and energetics for the observed dynamical motions in great detail. It is found that a series of Stone-Wales type transformations are responsible for the migration and structural transformations of DVs,

and that a pentagon-heptagon-heptagon-pentagon (5-7-7-5) defect appearing as an intermediate structure during the dynamical process plays an important role in the transformations of DVs.

5.1 Introduction

Since the first realization of graphene [6, 7, 8], tremendous efforts have been made to explore its physical properties as well as the potential applications in industries. Unique properties of graphene such as ultrahigh electron mobility [7, 17, 18], high thermal conductivity [19], and extreme mechanical properties [20] have been examined, and it is now widely accepted that graphene is one of the most promising materials for future electronic devices. Another exciting aspect of graphene-based materials is that their exotic properties can be enriched by atomic-scale defects engineering [87, 21, 88, 89, 90]. Defects engineering of graphene can enormously extend the scope of applications making graphene-based industry more plausible and promising. Indeed, chemical modifications, for example, by molecular doping [91, 92, 93] or functionalization [94, 95] are popularly suggested, and producing atomic vacancies by ionic irradiations [96, 97] is also a promising way to modify properties of graphene. In particular, recently developed high resolution transmission electron microscopy (TEM) is very useful to prove carbon-based materials. Since electron irradiation is a highly effective method to introduce various types of structural defects in graphene, many TEM studies are reported on defective graphene systems [98, 99]. For example, a recent TEM study by Cretu et al. [100] has shown that the graphene properties can be tailored by reconstructed point defects. They have pointed out the importance of divacancies (DVs) due to their abundance at room temperature. The existence of

DVs has also been predicted by other theoretical calculations showing the formation energy is lower than that of two isolated monovacancies (MVs) [101, 102] and the MVs have a tendency to coalesce to a DV [102, 103].

Recently, Girit et al. has reported the real-time dynamics of carbon atoms in defected graphene using the aberration-corrected TEM technique [2]. The subatomic resolution of the TEM images allows the direct observation of carbon atoms in graphene and provided clear images depicting the edge structure of graphene. Furthermore, the TEM images from the supplementary movie S1 ("the TEM images" from now on) in the report happen to show various structural forms of DVs and their dynamics. These contain crucial clues to understanding the structural change of DVs. Since the dynamics of DVs and their possible control are critical issues for graphene applications, we perform first-principles calculations in the present study to provide plausible explanations for the stability and dynamics of the DV.

We first inspect the movie S1 and choose eight consecutive frames in which we presume that important information for the dynamics of DVs is recorded. Then we analyze those frames manifesting their atomic structures. Using ab initio computational methods, we investigate energetically favorable diffusion pathways corresponding to the dynamics observed in the frames, and provide associated energy barriers. The microscopic mechanism is also provided for various types of migrations of triple pentagon-triple heptagon (555-777) and pentagon-octagon-pentagon (5-8-5) defects. Our results show 555-777 and 5-8-5 defects can migrate and rotate in graphene plane through a sequence of Stone-Wales (SW) type transformations. Since a specific motion of DVs has its own mechanism with distinct energy barriers, there exist a possibility to control the types of DVs produced depending on the

energy of incident electrons in a TEM experiment [104].

5.2 Computational details

The ab initio total energy calculations are performed with the plane-wave-basis-set VASP code [105] using a rectangular periodic supercell containing 126 carbon atoms with a single DV. The plane wave basis is used with a kinetic energy cutoff of 400 eV. We use projector augmented wave (PAW) potentials [106] for describing the core electrons and generalized gradient approximation (GGA) Perdew-Burke-Erenzerhof (PBE) [42] functional for the exchange-correlation. In order to search the energy barrier for the SW type transformation, which is essentially the 90 ° rotation of a single dimer, the orientation of the dimer is divided into small angles and fixed for one total energy calculation while the rest atoms are fully relaxed until the force on each atom is less than 0.02 eV/Å.

The TEM images in the early part of the movie [2] show the time evolution of a single DV within a suspended graphene sheet. Each frame of the TEM images is taken for 1 s of exposure with 4 s of a break. Through close inspection, we find that, starting from the 5th frame, eight sequential image frames [Figs. 5.1(b)-(i)] contain meaningful evidence for the structural change of DVs, and therefore we focus on these frames in this study. In the literature [2], it has been reported that DVs can be reconstructed and move around in the graphene plane owing to the kinetic energy transfer from the incident elections of 80 keV to carbon atoms [2]. The maximum energy transfer to a carbon atom has been reported to be 15.8 eV [107], which is large enough for a DV to diffuse and change its structure in graphene as we examine in this study.

5.3 Results and discussions

5.3.1 Interpretation of the TEM images

Figure 5.1 shows structural changes of DVs in a single layer graphene from aberration corrected TEM images. A DV is found in the region enclosed by the small (red) rectangle in Fig. 5.1(a). The Figures 5.1(b)-(i) show the magnified images of the region in the 5th-12th frames, respectively. Each of the 5th, 7th, and 9th frames [Figs. 5.1(b), (d), and (f), respectively] contains a 555-777 defect, and the 10th and 12th frames [Figs. 5.1(g) and (i)] contain a single 5-8-5 defect. The 5-8-5 defect observed in the 10th frame is different from that of the 12th frame in that the former has dangling bonds while the latter does not. The two adjacent carbon atoms of each vacancy in the latter 5-8-5 defect make bonding and leave no dangling bonds. Since the structures depicted in Figs. 5.1(c), (e), and (h) do not correspond to any known form of meta-stable DV atomic structures, they can be considered to be either transient unstable structures or superposed records of meta-stable ones.

Atomic assignments and corresponding total charge densities, obtained by ab initio calculations, are presented in Fig. 5.2. The fully relaxed atomic structures are assigned in Figs. 5.2(a) and (b) with the corresponding TEM frames and the simulated total charge densities. For unstable structures in Figs. 5.2(c) and (d), we choose the atomic positions from the TEM images by assigning carbon atoms to the bright points of the image. The simulated total charge density plots show that the atomic assignments can reproduce the TEM images very well. Fig. 5.2(h) shows the total charge density plot for the atomic structure presented in Fig. 5.2(d). The atomic structure is constructed from the TEM image [Fig. 5.1(c)] with the assump-

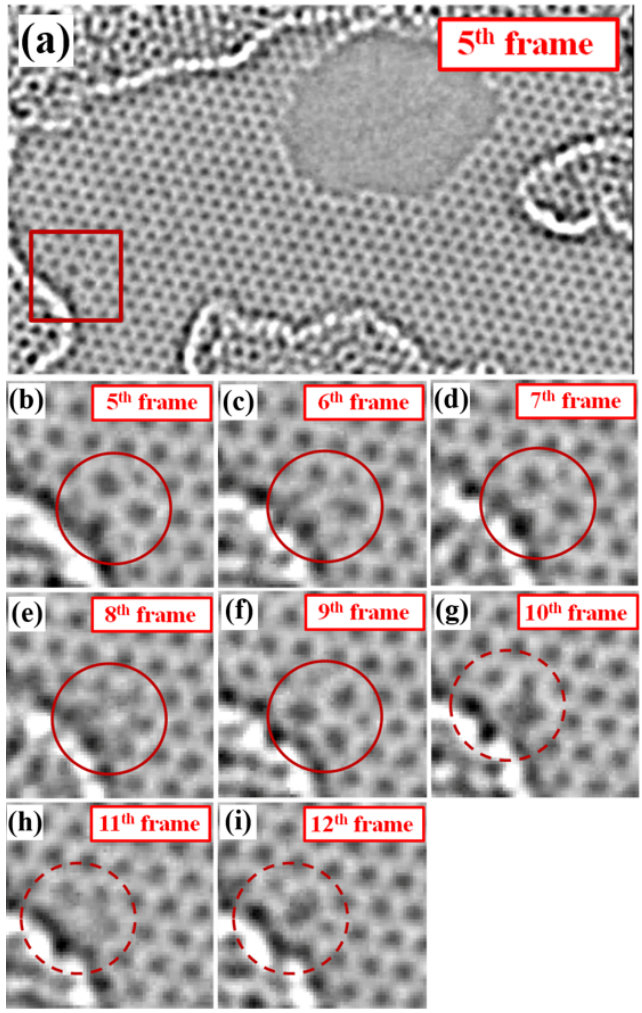

Figure 5.1: Aberration-corrected TEM images of DVs in a single layer graphene reported in supplementary movie S1 of Ref. [2]. (a) 5th frame of the movie S1. The rectangular (red) region contains a single DV and shows various DV reconstructions. The magnified images in this region for eight consecutive frames are drawn in (b)-(i). (b) The rectangular region in the 5th frame. This frame contains a triple pentagon and triple heptagon (555-777) defect. (c) The same rectangular region of the 6th frame. (d) The 7th frame in which the 555-777 defect structure is restored. (e) The 8th frame which captures an intermediate stage between two 555-777 defects in (d) and (f). (f) A 555-777 defect rotated by 60 ° with respect to the 555-777 defect in (d). (g)-(i) The 10th-12th frames. Theses frames contain a record of a single pentagon-octagon-pentagon defect (5-8-5) migration. Dashed circles in (g)-(i) are shifted one hexagon unit to the left compared to solid circles in (b)-(f) to highlight the migration of the 5-8-5 defect. Printed with the kind permission of authors of Ref. [2].

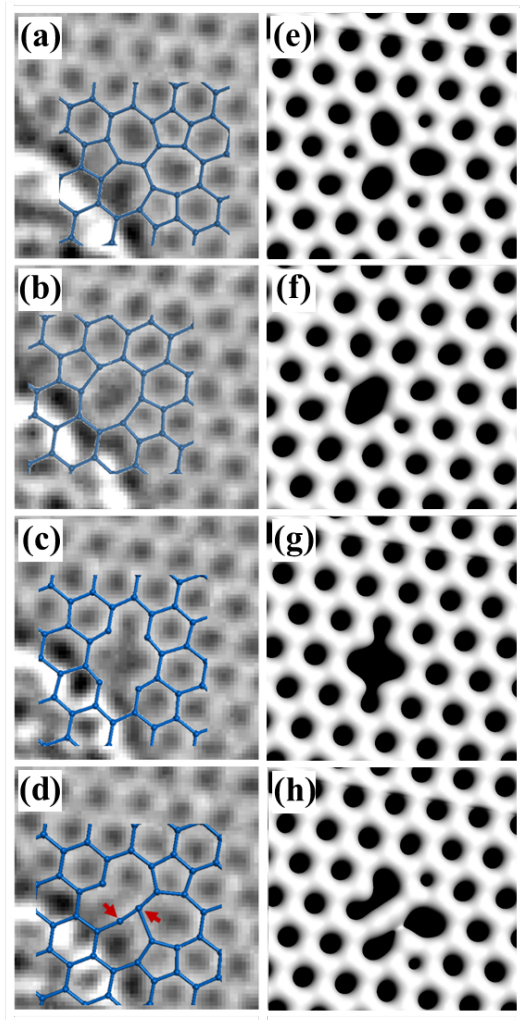

Figure 5.2: Atomic structures of DV reconstructions (a)-(d) and the corresponding simulated total charge density plots (e)-(h). (a) 555-777 defect corresponding to Figs. 5.1(b), (b) 5-8-5 defect corresponding to Figs. 5.1(i), (c) 5-8-5 defect with dangling bonds corresponding to Figs. 5.1(g), (d) 555-777 defect with the tilted carbon dimer [corresponding to Fig. 5.1(c)] indicated by the two (red) arrows compared to (a). Solid (blue) bars and dots indicate their structural models. (e)-(h) Simulated total charge density plots from ab initio calculations for structural models of (a)-(d), respectively.

tion that it has a 555-777 defect with a carbon dimer tilted by about 17 ° [indicated by two (red) arrows in Fig. 5.2(d)] with respect to that of the pristine 555-777 defect [Fig. 5.1(b)]. The resemblance of the simulated charge density [Fig. 5.2(h)] to the corresponding TEM image [Fig. 5.1(c)] provides strong evidence for our assumption on the TEM image [Fig. 5.1(c)]. The three consecutive images [Figs. 5.1(b)-(d)] are considered to be a record that a carbon dimer fails to achieve a SW type transformation. As mentioned in the supplemental material of a previous literature [108], if a SW type transformation were successful, the structural transformation between a 555-777 and a 5-8-5 defect would be observed just as shown in Figs. 5.1(f) and (g). The 555-777 defect is the most frequently observed DV structure in the TEM images (5th, 7th, and 9th frames). With the random transfer of the kinetic energy from ejected electrons to carbon atoms during the experiment, it is natural that more stable structures, the more frequently they are found. Abundant appearance of 555-777 defects in the experiment is, therefore, consistent with the fact that the 555-777 defects are the most stable structures among the known DV defects [102].

5.3.2 Rotation of 555-777 defect

Here, we clarify the structural changes during the rotation of a 555-777 defect recorded in 7th-9th frames of the TEM images [Figs. 5.1(d)-(f)]. The 555-777 defect presented in the 7th frame [Fig. 5.1(d)] is recovered in the 9th frame [Fig. 5.1(f)] with the position of pentagons switched to that of heptagons. Therefore, it appears that the 555-777 defect experiences a rotational motion during the time span taking the three frames (7th-9th frames). Hence, the atomic structure captured in the 8th frame [Fig. 5.1(e)] should record the intermediate stages of the rotation. How-

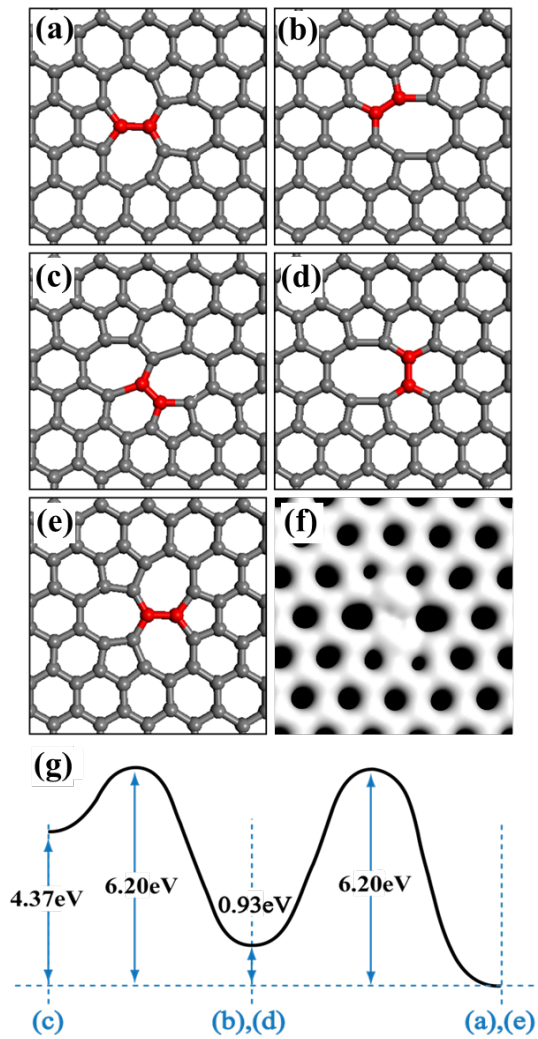

Figure 5.3: Microscopic atomic process for the rotational motion of a 555-777 defect. (a) 555-777 defect. (b) 5-8-5 defect. (c) 5-7-7-5 defect. (d) 5-8-5 defect. (e) 555-777 defect. (f) The charge-density plot obtained by averaging the three intermediate structures, (b)-(d). (g) Energy barriers for this process and formation energies relative to the 555-777 defect. Atomic structures shown in (b)-(e) can be obtained by a SW transformation of the dark (red) dimer shown in (a)-(d), respectively.

ever, since the atomic structure recorded in the frame is not matched to any known form of DVs, it is considered to be a superposition of several meta-stable intermediate structures. In analogy to a SW type transformation, we propose a pathway for the rotational motion of the 555-777 defect consisting of three intermediate meta-stable structures: 5-8-5, pentagon-heptagon-heptagon-pentagon (5-7-7-5), and 5-8-5 defects [Figs. 5.3(b)-(d)]. The 555-777 defect [Fig. 5.3(a)] can be transformed into a 5-8-5 defect [Fig. 5.3(b)] by a SW type transformation of a carbon dimer [indicated by a dark(red) dimer in Fig. 5.3(a)] [102]. The energy barrier for this process is found to be 6.20 eV in our ab initio GGA calculations, which is in good agreement with the local density approximation result (6.10 eV) [102]. The formation energy of the 5-8-5 defect is found to be 0.93 eV higher than that of the 555-777 defect. The structural change of the 5-8-5 defect to a 5-7-7-5 defect becomes possible by the 90 ° rotation of the dimer (SW type transformation) as shown in Fig. 5.3(b). The energy barrier for this process is 5.27 eV as shown in Fig. 5.3(g). The formation energy of the 5-7-7-5 defect in Fig. 5.3(c) is calculated to be 4.37 eV higher than that of a 555-777 defect and 3.44 eV higher than that of a 5-8-5 defect. The 5-7-7-5 defect is not found in the original TEM images due to the high formation energy relative to the 555-777 and 5-8-5 defect structures, but it has been observed in an aberration corrected TEM images for reduced graphene oxides [109]. The 5-7-7-5 defect structure is reconstructed into the 555-777 defect through the 5-8-5 defect by two sequential SW type transformations as shown in Figs. 5.3(c)-(e). In Fig. 5.3(f), we plot the average charge density of the three intermediate meta-stable structures (5-8-5, 5-7-7-5, and 5-8-5 defects). In the charge density plot, a white spot area appears at the position of the center of two 555-777 defects and it is surrounded by

six dark spots which are located with an angular interval of 60 ° each. The figure shows a quite good agreement with the TEM image in the 8th frame [Fig. 5.1(e)]. Especially, the position of the darker spot on the right hand side among those six dark spots is in excellent agreement with the position of the larger dark spot in Fig. 5.3(f). The resemblance of the charge density to the TEM image in the 8th frame provides a reasonable evidence for our interpretation. Although we consider another pathway of direct transformation from Fig. 5.3(a) to Fig. 5.3(e) by the simultaneous 60 ° rotation of three carbon atoms around the center atom of the 555-777 defect structure, the energy barrier is found to be higher than that of our favorable pathway by 1.7 eV.

5.3.3 Migration of 5-8-5 defect

We also investigate the migration of a 5-8-5 defect recorded in 10th-12th frames of the original TEM images [Figs. 5.1(g)-(i)]. As previously mentioned, the DV defects appearing in the 10th and 12th frames are different kinds of 5-8-5 defects; the 5-8-5 defect in the 10th frame [Fig. 5.1(g)] has dangling bonds, while the other does not [Fig. 5.1(i)]. For the present discussion on the migration of a 5-8-5 defect, however, we only consider 5-8-5 defects without dangling bonds because the dangling bonds disappear easily in the structural relaxation of 5-8-5 defects according to our ab initio calculations. The intermediate 11th frame shows an unclear atomic configuration and it is also conjectured to be a superposition of intermediate metastable structures. As shown in Figs. 5.4(a)-(d), the 5-8-5 defect structure undergoes the migration and the 60 ° rotation via 5-7-7-5 defects twice by three sequential SW type transformations. The corresponding energy barriers for the pathway are shown

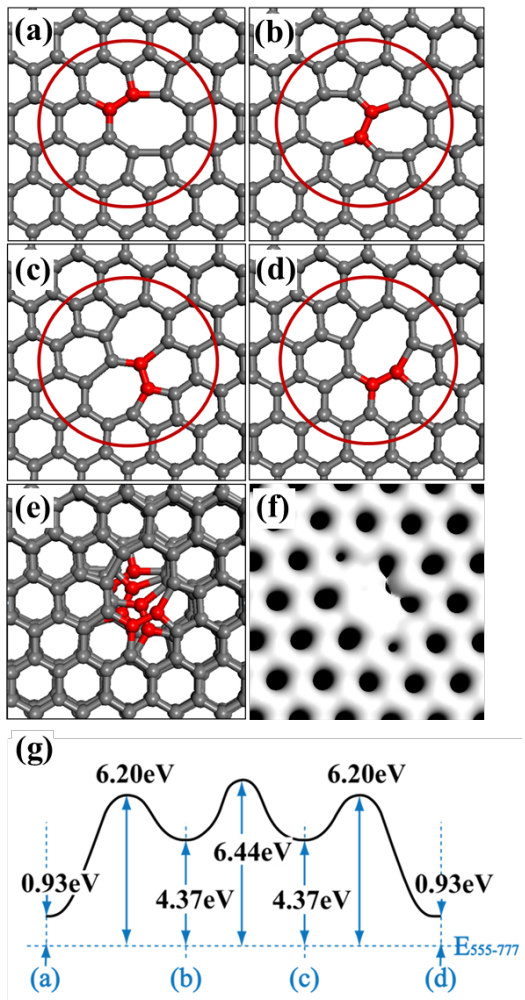

Figure 5.4: Microscopic atomic process for the migration of a 5-8-5 defect. (a) 5-8-5 defect corresponding to the TEM image in Fig. 5.1 (g). (b) 5-7-7-5 defect. (c) 5-7-7-5 defect. (d) 5-8-5 defect. The atomic structure in (d) corresponds to the atomic assignment of Fig. 5.1(i). Dark (red) dimer in each figure is the part which undergoes a SW type transformation. (e) Superposition of the atomic structures, (a)-(d). (f) The simulated total charge density plot obtained by averaging the four structures, (a)-(d). (g) Schematic diagram representing energy barriers for the 5-8-5 migration from (a) to (d) and formation energies relative to the 555-777 defect.

in Fig. 5.4(f) and such a process is possible due to the transfer of kinetic energy from incident electrons to the carbon atoms during the experiment. The superposition of the two 5-8-5 defects [Figs. 5.4(a) and (d)] and two 5-7-7-5 defects [Figs. 5.4(b) and (c)] structures and the average of their simulated total charge densities are shown in Figs. 5.4(e) and (f), respectively. The average charge density plot shows charge deficiency between two black spots on the upper right hand direction from the center of the defects. This is in quite good agreement with the TEM image in the 11th frame [Fig. 5.1(h)]. Therefore, the 11th frame is considered to be a superposition of those meta-stable structures. Our analysis again indicates that the rotation of the 5-8-5 defect found in the TEM images may be achieved by a series of SW type transformations.

5.4 Summary and Concluding Remarks

In summary, we have investigated the dynamics and stabilities of DVs in graphene observed in the TEM experiment by ab initio total energy calculations. The TEM images reported in the literature [2] contain various DV reconstruction structures, such as 555-777 and 5-8-5 defects, providing evidence for the structural transformations among those DVs. We have calculated detailed microscopic process of the 555-777 rotation as well as the 5-8-5 migration and corresponding energy landscapes. In the structural transformation of DVs, the 5-7-7-5 defect is found to play an important role as a meta-stable structure. Our simulated images are in good agreement with the observed TEM pictures and these results provide a deep insight into the dynamics of DVs in graphene.

CHAPTER 6

Silicene with a line defect: topological domain walls and quantum valley Hall effects

Silicene is a two-dimensional honeycomb lattice made of silicon atoms, which is considered to be a new Dirac fermion system. Based on first-principles calculations, we examine the possibility of the formation of soliton-like topological domain walls (DWs) in silicene. We show that the DWs between regions of distinct ground states of the buckled geometry should bind electrons when a uniform electric field is applied in the perpendicular direction to the sheet. The topological origin of the electron confinement is demonstrated based on numerical calculations of the valley-specific Hall conductivities, and possible experimental signatures of the quantum valley Hall effects are discussed using simulated scanning tunneling microscopy images. Our

results strongly suggest that silicene could be an ideal host for the quantum valley Hall effect, thus providing a pathway to the valleytronics in silicon-based technology.

6.1 Introduction

Recently, silicene, a silicon-version of graphene, is successfully synthesized on metal and semiconductor substrates [22, 23, 24, 25, 26]. Sharing many intriguing electronic properties with graphene such as Dirac cone-like low-energy band structures, silicene has attracted much attention both theoretically and experimentally [28, 110, 111, 112]. Moreover, due to its intrinsic buckled geometry [33], diverse phenomena unexpected in graphene have also been suggested. Examples include band gap engineering by an external electric field [28], the quantum spin Hall (QSH) effect [61, 113] at experimentally accessible temperature [114], the phase transition from a QSH insulator to a quantum valley Hall (QVH) insulator [115, 116, 117, 118] via an external electric field [119, 120, 121], and still other exotic topological effects [29, 122, 30].

Motivated by the recent synthesis of silicene, here we suggest another interesting topological phenomenon associated with a QVH insulator. A QVH insulator is a topological phase characterized by valley-specific Hall conductivities $\sigma_{\mathrm{H}}^{\mathrm{K}\,(K')}$ and valley-polarized chiral modes emerging on specific sample boundaries [31, 123, 124] or domain walls (DWs) [125, 126, 127, 128, 129, 130, 131]. In this intriguing topological phase, DWs between regions of different valley Hall conductivities are of particular interest because they may seamlessly glue the momentum space belonging to the same valley, so the DW modes may survive within the midgap region regardless of the crystallographic details of the DWs [132]. Also, it is an exciting idea to host

robust conducting channels inside the bulk rather than on edges because they can serve as 1D conducting wires of circuits integrated in 2D insulators [126, 128, 129]. The material realization of the topological DWs has been theoretically suggested in bilayer graphene under an inhomogeneous electric field [125, 128], in graphene nanoribbon gluing boron nitride sheets [129], and in a AB-BA graphene bilayer tilt boundary under a homogeneous electric field [130, 131].

In this Section, we examine a new type of topological DWs based on silicene. We consider the zigzag line interfaces across which the buckling height switches between the two sublattices (Fig. 6.1), and show that they serve as topological DWs associated with a QVH insulator under a uniform perpendicular electric field. Distinct from the previously suggested topological DWs, the formation of the DWs suggested in this study is assisted by a symmetry breaking process originated from an intrinsic instability residing in the honeycomb lattice made of silicon atoms. In this respect, the underlying mechanism of the DW formation is more similar to that of solitons in polyacetylene, of which the formation is assisted by the Peierls instability in the 1D metallic chain [133]. Our results based on first-principles calculations confirm that electrons are confined to the DWs when a uniform perpendicular electric field is applied, forming one-dimensional (1D) conducting states along the DWs in the otherwise insulating material. The topological origin of the confinement is numerically demonstrated by the direct calculation of the topological invariant associated with the valley-specific Hall conductivities. We also present simulated scanning tunneling microscopy (STM) images to help guide experimental efforts to identify the topological DWs and the QVH effects. Our results suggest that, by introducing the DW in silicene, its electronic and transport properties may be electrically controlled, and

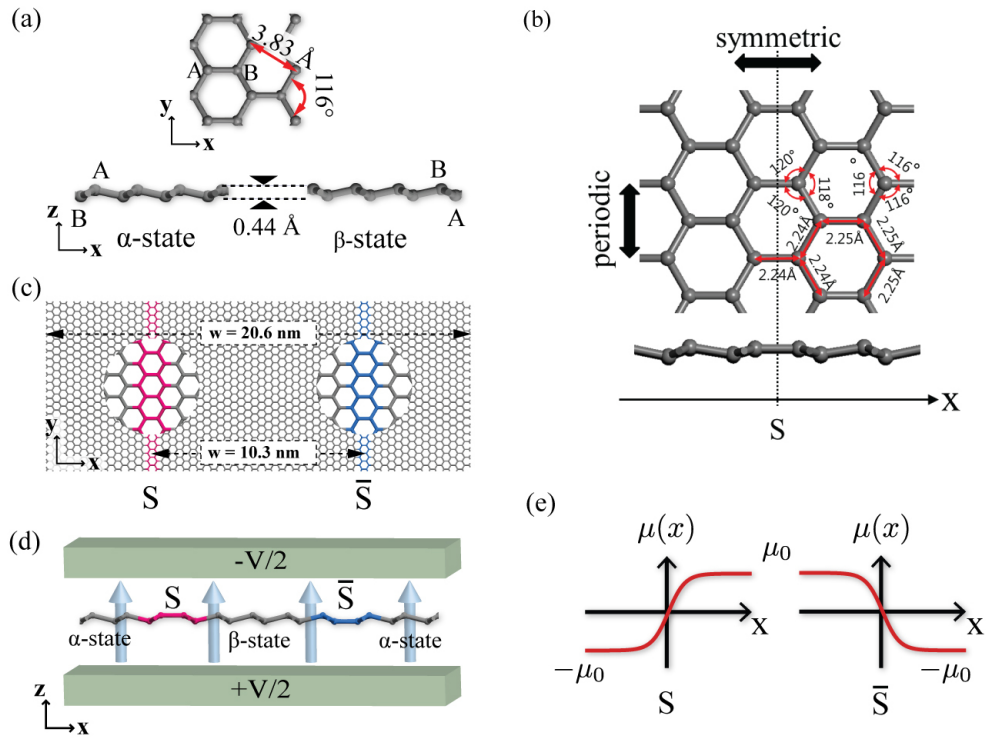

Figure 6.1: (a) The geometry of the low-buckled silicene. (b) A domain wall (DW) geometry between α and β low-buckled states. (c) Top view of a supercell geometry with zigzag DWs. A pair of soliton- and antisoliton-like domain walls (S and $\bar{\text{S}}$) are separated by 10.3 nm in the supercell. The magnified views of the detailed atomic structure of the S and $\bar{\text{S}}$ regions are also illustrated. (d) Schematic configuration of the junction geometry under applied electric fields. The arrows indicate the direction of the applied electric field. (e) The position-dependent buckling order parameter $\mu(x)$ for soliton (S) and antisoliton ($\bar{\text{S}}$).

therefore, the scope of its applications in the future silicon-based technology can be extended.

6.2 Computational details

Our first-principles calculations were based on the density-function theory (DFT). We constructed a supercell geometry composed of two degenerate buckled geometries [Fig. 6.1 (a)], and their interfaces were modeled by zigzag lines across which the heights of sublattices were interchanged as shown in Fig. 6.1 (b). In order to fulfill the periodic boundary condition imposed on the supercell, we introduced a pair of DWs denoted by S (soliton) and $\bar{\text{S}}$ (antisoliton) in Figs. 6.1(c) and 6.1(d). The electronic structure calculation and the structure optimization were performed using the SIESTA package [52] and the VASP code [134], respectively. Exchange and correlation potentials were employed within the local density approximation (LDA) as described by Ceperley and Alder [135]. Periodic sawtooth potentials were introduced to describe the external electric fields. Berry curvatures were calculated on 300×300 numerical grids of the first BZ. To circumvent the problems associated with numerical random phases and slow convergence, we adopted the prescription of computing the Berry curvatures on discretized BZ [32]. Throughout this study we safely ignored the spin degree-of-freedom because the effect of spin-orbit coupling was negligibly small in the present situation [121, 120]. The calculated bond length and the buckling distance were 2.26 Å and 0.44 Å, respectively, as presented in Fig. 6.1(a). The DWs remained stable upon the full relaxation maintaining the planar geometry under the force criterion of 0.01 eV/Å. The existence of the DWs does not make the junction elbowed or bent during the relaxation. Our calculations

show that it costs extra energy to elbow the relaxed planar junction due to the misalignment of perpendicular (p_z) orbitals in forming π or π^* bonding, as in the case of graphene [136]. Another interesting feature of the relaxed geometry is that the structural modifications by the presence of the DWs are confined to a narrow (atomic scale) region near the DWs. As shown in Fig. 6.1(b), bond lengths and bond angles are 2.24 Å and 120° at the junction, while they are recovered immediately to the bulk values of 2.25 Å and 116° only $\sim$ 3 Å away from the DW.

6.3 A continuum model

Before we present our numerical results, we briefly explain how the buckled geometry of silicene can allow the formation of the topological DWs based on a continuum model. Unlike graphene, free-standing silicene in its perfect planar geometry develops structural instability, which is lifted via so-called low buckling (LB) [33] with one of two sublattices of the honeycomb lattice being shifted (0.44 Å) in the perpendicular direction to the silicene plane. From the LB, the followings are expected. (1) The LB spontaneously breaks the reflection symmetry with respect to the silicene sheet (σ_h) developing non-vanishing buckling order parameter (OP), which is defined by the vertical displacement between the two sublattice planes. The symmetry breaking leads to doubly degenerate ground states of the buckled geometry, one of which transforms to the other by reflection [See Fig. 6.1(a)]. Hereafter, we call them as α- and β-states, respectively. (2) Due to the degeneracy, we expect a structural excitation to exist in the form of one-dimensional (1D) interfaces separating two vacua ground states, which can be represented by a position-dependent OP $\mu(x)$

asymptotically behaving like a topological soliton (or antisoliton):

$$\lim_{x\to\pm\infty}\mu\left(x\right)=\begin{cases}\pm\mu_0 & (soliton)\\ \mp\mu_0 & (antisoliton)\end{cases}, \tag{6.1}$$

where μ_0 (defined to be positive) and $-\mu_0$ represent the OPs of the two ground buckled geometries [See Fig. 6.1(e)]. In the presence of the electric field E_z, the LB (OP) $\mu(x)$ couples to the field, and gives rise to a position-dependent mass potential $g\mu(x)E_z/{v_F}^2$ for the Dirac fermions, governed by the effective model Hamiltonian

$$H=\hbar v_{\mathrm{F}}\left(-i\frac{d}{dx}\tau_z\sigma_x+q_y\sigma_y\right)+g\mu(x)E_z\sigma_z. \tag{6.2}$$

Here v_{F} is the Fermi velocity near the Dirac point, and $\boldsymbol{\sigma}$ is the Pauli matrices according to the sublattice index, and $\tau_z=\pm1$ labels the valley index. $\mathbf{q}$ is the lattice momentum along the parallel direction to the DW and measured from the valley centers at K and K$'$ points. g is introduced to represent the coupling strength (effective charge) between the external field and $\mu(x)$. As noted in the previous work [126], the Hamiltonian supports gapless chiral modes confined to the 1D DW (hereafter, we will call them as kink states)

$$\psi_{s,\tau_z}(x,y)\sim e^{iq_y y-s\frac{gE_z}{\hbar v_{\mathrm{F}}}\int_0^x\mu(x')dx'}\left(1-\tau_z i,\right) \tag{6.3}$$

with linear energy spectrum $E=-s\tau_z\hbar v_{\mathrm{F}}q_y$ along the DWs. Here $s=\pm1$ labels a soliton $(+1)$ or an antisoliton (-1). This continuum model explains how the LB allows the formation of the topological DWs. Having established the underlying mechanism, we move to the ab initio results confirming the above argument.

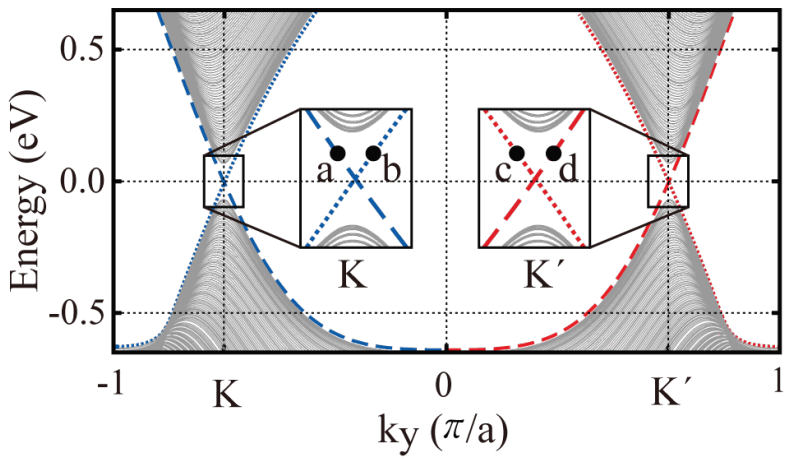

Figure 6.2: Band structure of the supercell geometry. The solid grey lines in the inset correspond to bulk states, and the dotted and dashed lines indicate the kink states at S and $\bar{\text{S}}$, respectively. The blue and red color schemes are used to represent K and K′, respectively. The dots (a to d) correspond to the states at 10 meV above the Fermi level.

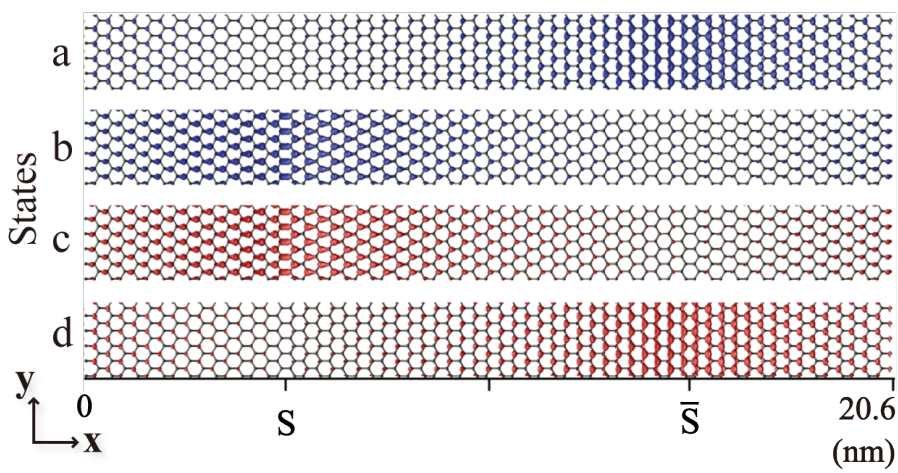

Figure 6.3: Probability distributions of the QVH kink states at a-d in Fig. 6.2.

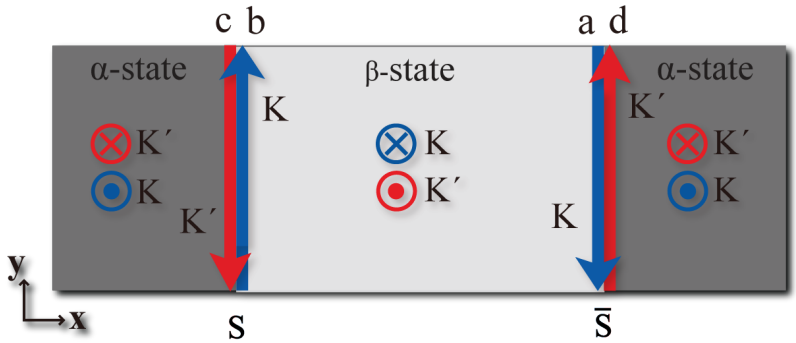

Figure 6.4: Schematic illustration of kink states. Electrons at different valleys propagate in opposite directions on the DWs. S supports an upward K current and a downward K′ current and vice versa for $\bar{\text{S}}$. The senses of the arrows perpendicular to the page represent the sign of the valley Hall conductivities associated with each valley.

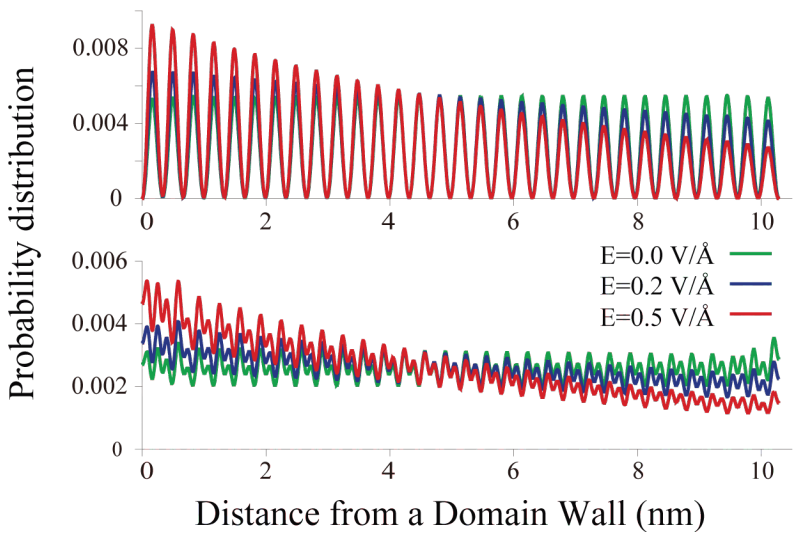

Figure 6.5: Probability distributions of the wavefunctions at $E = 10$ meV from the Fermi energy. The top panel corresponds to a (or equally to d) state , and the bottom panel corresponds to b (or equally to c) state in in Fig. 6.2. By increasing the applied electric field, states become more concentrated on the DW.

6.4 Results and Discussion

6.4.1 Electronic structures of a DW geometry

Figure 6.2 shows the calculated band structure from the supercell geometry by applying the electric field of 0.5 V/Å. The bulk continuum is represented by the grey shaded area. A bulk band gap of $\sim$ 0.1 eV is induced and four branches (ignoring spins) of gapless modes appear in the midgap region. The real-space representation of these states presented in Fig. 6.3 shows that they are localized on DWs and propagating along the parallel direction to the DWs. More specifically, two branches of different valleys and different group velocities are localized one DW, as schematically summarized in Fig. 6.4. Therefore, one branch per spin and per valley emerges on a single DW. This result shows that backscattering is only allowed by changing the valley indices, which guarantees the robustness of valley polarized currents [128] flowing along the 1D metallic DW channels.

Upon varying the strength of the electric field, we find that the degree of localization of electrons to the DWs can be controlled; the electrons are more (less) concentrated on the DWs by increasing (decreasing) the strength of the perpendicular field, as shown in Fig. 6.5. This is a natural consequence of the gap size, which determines the decay strength of the kink states [126], being proportional to the applied field here [110]. We also find that, in the absence of the electric field, the bulk gap indeed vanishes and the kink states return to extended bulk states with a slight modification near the DWs as described by green curves in Fig. 6.5. This result indicates that the introduction of the DWs cannot open the band gap without an applied electric field.

6.4.2 Topological origin of the kink states

Although we only present the results obtained from a particular atomic configuration of DWs as a representative example, we have tested different atomic configurations of DWs, and always found two midgap branches per spin on a single DW. Depending on the crystallographic details, the DWs may produce an interaction mixing two valleys, thus leading to the opening a subgap in kink-states band. We actually have found several configurations inducing the armchair DWs that open a subgap, and its size has been typically ~ 1 meV. Since the subgap size is much smaller than the bulk gap (~ 0.1 eV), the kink states remain in the bulk gap region, determining the low-energy transport properties. In fact, this result has a topological origin; the number of kink states emerging on the DW is determined by the topological invariant, defined to be the difference between the valley Hall conductivities in the adjacent bulk (i.e., infinitely extended in two dimensions) domains [137, 132, 127]. To further discuss this point, we numerically calculate Berry curvatures and valley Hall conductivities [115]. The left panel of Fig. 6.6 shows the Berry curvature obtained from the α-state of the buckled geometry under the electric field of 0.5 V/Å. Note that Berry curvatures are highly concentrated on the K and K$'$ points having opposite signs in different valleys. The valley Hall conductivities are obtained by integrating the Berry curvatures on the BZ [118]. We note that two valley indices share the same BZ, and therefore, in general, there exists intrinsic ambiguity in assigning the portions of the BZ to calculate a specific valley Hall conductivities [132]. Therefore, in some largely gapped system, numerical calculations beyond the $\mathbf{k}\cdot\mathbf{p}$ description may result in unquantized valley Hall conductivities. Nonetheless, in the present system, the valley Hall conductivities are accurately defined because the Berry curvatures are

well-concentrated in the vicinity of valley-centers (K and K′) points. Our numerical results show that, upon the integration of the Berry curvature up to ~ 0.5 Å^{-1} from the K (K′) point, the valley Hall conductivity is fully converged to 1/2 (−1/2) in unit of $2e^2/\mathrm{h}$ (the factor 2 accounts for spins), resulting in $\sigma_{\mathrm{H}}^{\mathrm{K}\,(K')} = +(-)1/2$. This result confirms the QVH insulating state introduced in the low-buckled silicene by an applied electric field. Also, the integration of the Berry curvature over the whole BZ gives zero, which reconfirms the fact that the (charge) Hall conductivity should vanish in a time-reversal invariant band insulator.

The α-state of the buckled geometry is obtained by the C_2 rotation of the β-state around z-axis, which exchanges the valley indices between K and K′. Therefore, the K (K′) point of the α-state plays the role of the K′ (K) point in the β-state. This feature is reflected in our numerical calculations of the Berry curvatures as shown in Fig. 6.6, i.e., $\sigma_{\mathrm{H},\alpha}^{\mathrm{K}(K')} = -\sigma_{\mathrm{H},\beta}^{\mathrm{K}(K')}$, where $\sigma_{\mathrm{H},\alpha(\beta)}^{\mathrm{K}(K')}$ is the valley Hall conductivity calculated in the α (β)-state for a given valley index K (K′). The two buckled ground states host different QVH states under a uniform electric field characterized by different valley Hall conductivities. The result is consistent with the chiral asymmetric index theorem [137] which dictates that the number of the kink states emerging on a single DW is determined by a topological invariant defined to be the difference of the valley Hall conductivities (in unit of $2e^2/h$) between adjacent domains, $\sigma_{\mathrm{H},\,\alpha}^{\mathrm{K}\,(K')} - \sigma_{\mathrm{H},\,\beta}^{\mathrm{K}\,(K')}$. Note that we have obtained the valley Hall conductivities of $\pm 1/2$ for two buckled states, thus $\sigma_{\mathrm{H};\alpha}^{\mathrm{K}\,(K')} - \sigma_{\mathrm{H};\beta}^{\mathrm{K}\,(K')} = 1(-1)$ in good agreement with the number of kink states emerging on a DW per valley. The sign indicates the propagating direction of the chiral kink states. This result explains the topological origin of the kink states, which can protect the number of DW modes regardless of the

crystallographic configuration of the DW [132]. In practice, however, we may have to pay more attention to zigzag line-like DWs than others, not only because because they are more easily produced according to our formation energy calculations. We find that the formation energy of the zigzag DWs is $\sim$ 25 meV/Å, which is smaller than that of other tested configurations such as armchair DWs with the formation energy of $\sim$ 39 meV/Å.

6.4.3 Possible experimental signature: STM simulations

Finally, we propose a way of detecting the formation of DWs as well as the QVH effects in silicene by using STM. Figures 6.7(a) and 6.7(b) simulate the STM images under the sample bias V_{bias} of -20 mV, and Figs. 6.7(c) and 6.7 (d) simulate $V_{bias} = -1.4$ V. Figures 6.7(a) and 6.7(c) correspond to the states localized at S, while Figs. 6.7(b) and 6.7(d) correspond to those at $\bar{S}$. Bright protrusions in the STM images show the upper-buckled silicon atoms forming the triangular lattice in each domain. The DWs can readily be identified as the lines shifting the locations of protrusions from one sublattice to the other as shown in the middle of the images. The simulated images in Figs. 6.7(c) and 6.7(d) represent the filled states in the energy window from the Fermi energy to -1.4 eV, where extended bulk states make major contributions and thus exhibit almost no change as the applied electric field varies. However, the simulated STM images under a sample bias of -20 mV and applied external field of 0.5 V/Å [Figs. 6.7(a) and 6.7(b)] show a noticeable change by the applied field. These figures represent the filled kink states residing in the bulk gap. Comparing with the simulated STM images at $V_{bias} = -1.4$ V [Figs. 6.7(c) and 6.7(d)], the brightness of the protrusion is attenuated away from the DWs in Figs. 6.7(a) and 6.7(b), which

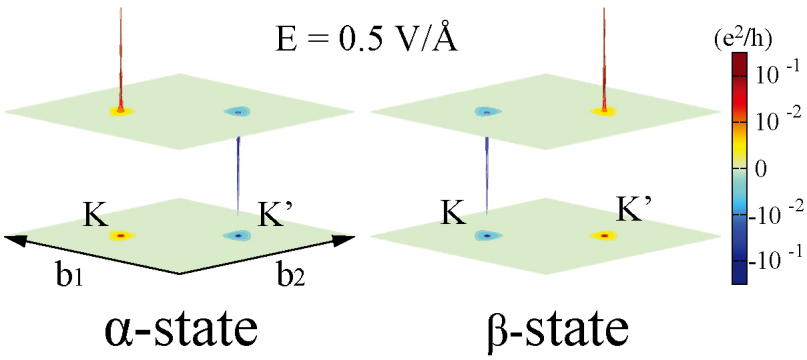

Figure 6.6: The Berry curvatures for the α-state (left panel) and the β-state (right panel) under the applied electric field of 0.5V/Åusing the color code scale in units of e^2/h.

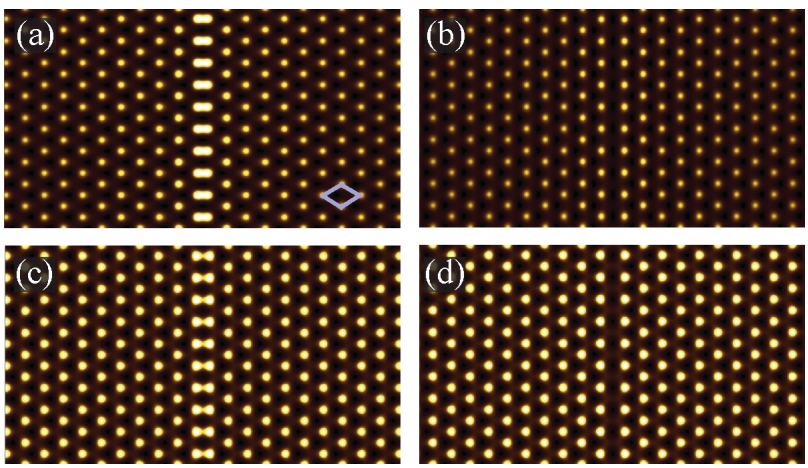

Figure 6.7: (a)-(d) Simulated scanning tunneling microscopy (STM) images for soliton [(a) and (c)] and antisoliton [(b) and (d)] DWs at different sample biases. The rhombus in (a) represents the 1×1 unitcell. Sample biases are chosen to be -20 mV in (a) and (b), and -1.4 V in (c) and (d). An external field of 0.5 V/Åis applied perpendicular to the sheet in (a) and (b). Bright spots correspond to the upper buckled silicon atoms, and DWs reside along the center of the images.

reflects the kink states being localized on the topological DWs and exponentially decaying in the asymptotic region [125]. For the small bias of -20 mV, reducing (turning off) the applied electric field leads to the reduction (disappearance) of the attenuation, and the simulated images resemble those of $V_{bias} = -1.4$ V. Therefore, STM images under varying electric fields are signatures of the QVH effect in silicene, and STM should be useful for identifying the DWs and the associated kink states, thus providing direct evidence for the QVH effect.

6.5 Summary and Concluding Remarks

In summary, we have presented a first-principles study on the QVH effects in silicene. The buckled geometry of silicene allows the manifestation of the QVH effects through DWs. Electrons are confined to the DWs by applying a perpendicular electric field, forming gapless kink states. The kink states exhibit common features of the QVH chiral states such as the valley-polarization, valley Hall currents propagating oppositely for different valley indices, and the absence of backscattering. In particular, we have provided the first-principles confirmation of the chiral asymmetric index theorem [137, 132] which guarantees the number of kink states emerging on the DWs. We have also provided simulated STM images to show that STM experiments can directly observe the QVH effects in silicene. Our results suggest that the DWs may serve as robust conducting wires embedded in silicene and enable the realization of valleytronics [138] as a next-generation electronics in the silicon-based industry.

CHAPTER 7

Summary and conclusion

In this thesis, we have considered the defect-related electronic structure and properties of a metallic carbon nanotube (CNT), graphene, and silicene. First, we have shown that nontrivial quantum loop currents can be generated on a metallic CNT by introducing a Stone-Wales defect due to the quantum interference between a conducting channel and a defect state. The intensity of the loop current is found to be maximized at the energy $E_F = E_0$ where $G(E_0) = 1.5G_0$, at which the intensity of loop current is more than one order of magnitude greater than that of axial currents of a pristine CNT. It is also found that these loop currents abruptly change their direction as the energy of incident electrons passes through the dip position E_1 where $G(E_1) = 1.0G_0$. This feature is consistent with the fact that the transmission coefficient associated with the scattered channel abruptly changes its phase by 180° as the energy passes through the energy where a defect state resides. Having shown the first-principles evidence of loop current generation, we have suggested that the loop currents can induce a dipole-like magnetic field whose magnitude can

maximally become about 0.05 μ_B by 10 meV bias. Here μ_B represents the Bohr magneton. We have also suggested that the peculiar behaviors of the loop current at different energies can be used to generate an experimental signature of the loop currents. By temporally changing the Fermi energy of incident electrons via a time-modulating gate voltage, for example, one may generate oscillating magnetic fields. Although the hence generated magnetic flux is rather small to be directly measured using current magnetometer technologies, considering the fascinating progress in the related technology, we expect our finding can be observed in near future.

Second, we have shown that the structure of divacancy can transform from one reconstructed structure to another one under an electron beams of 80 keV. We have found that the transmission electron microscopy (TEM) experimental data generated by Girits el al. [2] have captured the dynamics of a divacancy. Motivated by the experiment we have shown that the microscopic process for the structural transformations. More specifically, we have shown that a divacancy can rotate and migrate via a series of Stone-Wales type of structural transformation. The detailed microscopic process of the 555-777 rotation and the 5-8-5 migration is revealed and the corresponding energy barriers are calculated to be 6.2 eV and 5.3 eV, respectively. Our finding may suggest that electron beam can induce dynamics of a divacancy, and ultimately shed lights on the possibility for a divacancy to be controlled via an appropriate kinetic energy of incident electrons.

Finally, we have investigated the possibility of the emergence of topologically protected zero modes by introducing a line defect in a silicene. Silicene is the silicon-version of graphene, a new 2D honeycomb lattice made of silicon atoms. Unlike graphene, silicene is expected to be stable only in its buckled geometry. By the

buckled geometry, here means that one of the two sublattices of the honeycomb lattice is vertically shifted from the other sublattice, so that the two sublattices are spatially separated. We have suggested that the buckling spontaneously breaks the reflection symmetry and thus the ground states of the buckled geometry should be doubly degenerate. If this is the case, it is highly likely that the two degenerate ground states may exist simultaneously in a single sheet and their boundary should be connected by a line defect. Here we have shown that the line defect (interface) should play a role of topological domain wall in the presence of an applied electric field supporting zero modes localized on the domain wall. The zero mode, named by us as kink states, with different valley indices propagate in the different directions along the domain wall, so that we expect they might be applied to generate valley-polarized currents. We have discussed the topological nature of the kink states by calculating the Berry curvature as well as valley-specific Hall conductivities. For a given valley index, the valley-specific Hall conductivities are turned out to have different signs in different buckled ground states. Thus, the difference between them plays a role of topological invariant whose absolute value corresponds to the number of kink states emerging on a single domain wall, and whose sign corresponds to the propagating direction of the kink state along the domain wall. The unique electronic property of silicene that we found may suggest that silicene can be a promising material for a valley-polarizer or valley-filter, thus help guide experimental efforts to realize valleytronics.

The defect-induced electronic properties and structures presented here, although they are only a few examples of selected materials, may suggest that defects should play important role to control the electronic properties of nanomaterials and pro-

duce fascinating opportunities for the occurrence of new interesting phenomena and applications.

Bibliography

[1] Hyoung Joon Choi and Jisoon Ihm. Ab initio pseudopotential method for the calculation of conductance in quantum wires. *Phys. Rev. B*, 59:2267–2275, Jan 1999.

[2] Çaḡlar Ö. Girit, Jannik C. Meyer, Rolf Erni, Marta D. Rossell, C. Kisielowski, Li Yang, Cheol-Hwan Park, M. F. Crommie, Marvin L. Cohen, Steven G. Louie, and A. Zettl. Graphene at the edge: Stability and dynamics. *Science*, 323(5922):1705–1708, 2009.

[3] Cheng-Cheng Liu, Hua Jiang, and Yugui Yao. Low-energy effective hamiltonian involving spin-orbit coupling in silicene and two-dimensional germanium and tin. *Phys. Rev. B*, 84:195430, Nov 2011.

[4] Neil W. Ashcroft and N. David Mermin. *Solid state physics*. Thomson Learning, Inc., USA, 1976.

[5] Sumio Iijima. Helical microtubules of graphitic carbon. *Nature*, 354(6348):56–58, Nov 1991.

[6] K. S. Novoselov, A. K. Geim, S. V. Morozov, D. Jiang, Y. Zhang, S. V. Dubonos, I. V. Grigorieva, and A. A. Firsov. Electric field effect in atomically thin carbon films. *Science*, 306(5696):666–669, 2004.

[7] K. S. Novoselov, A. K. Geim, S. V. Morozov, D. Jiang, M. I. Katsnelson, I. V. Grigorieva, S. V. Dubonos, and A. A. Firsov. Two-dimensional gas of massless dirac fermions in graphene. *Nature*, 438(7065):197–200, Nov 2005.

[8] Yuanbo Zhang, Yan-Wen Tan, Horst L. Stormer, and Philip Kim. Experimental observation of the quantum hall effect and berry's phase in graphene. *Nature*, 438(7065):201–204, Nov 2005.

[9] Adrian Bachtold, Christoph Strunk, Jean-Paul Salvetat, Jean-Marc Bonard, Laszlo Forro, Thomas Nussbaumer, and Christian Schonenberger. Aharonov-bohm oscillations in carbon nanotubes. *Nature*, 397(6721):673–675, Feb 1999.

[10] Stefan Frank, Philippe Poncharal, Z. L. Wang, and Walt A. de Heer. Carbon nanotube quantum resistors. *Science*, 280(5370):1744–1746, 1998.

[11] Sander J. Tans, Michel H. Devoret, Hongjie Dai, Andreas Thess, Richard E. Smalley, L. J. Geerligs, and Cees Dekker. Individual single-wall carbon nanotubes as quantum wires. *Nature*, 386(6624):474–477, Apr 1997.

[12] Marc Bockrath, David H. Cobden, Paul L. McEuen, Nasreen G. Chopra, A. Zettl, Andreas Thess, and R. E. Smalley. Single-electron transport in ropes of carbon nanotubes. *Science*, 275(5308):1922–1925, 1997.

[13] Ray H. Baughman, Changxing Cui, Anvar A. Zakhidov, Zafar Iqbal, Joseph N. Barisci, Geoff M. Spinks, Gordon G. Wallace, Alberto Mazzoldi, Danilo

De Rossi, Andrew G. Rinzler, Oliver Jaschinski, Siegmar Roth, and Miklos Kertesz. Carbon nanotube actuators. *Science*, 284(5418):1340–1344, 1999.

[14] Sander J. Tans, Alwin R. M. Verschueren, and Cees Dekker. Room-temperature transistor based on a single carbon nanotube. *Nature*, 393(6680):49–52, May 1998.

[15] Guangli Che, Brinda B. Lakshmi, Ellen R. Fisher, and Charles R. Martin. Carbon nanotubule membranes for electrochemical energy storage and production. *Nature*, 393(6683):346–349, May 1998.

[16] J. Li, C. Papadopoulos, J. M. Xu, and M. Moskovits. Highly-ordered carbon nanotube arrays for electronics applications. *Applied Physics Letters*, 75(3):367–369, 1999.

[17] S. V. Morozov, K. S. Novoselov, M. I. Katsnelson, F. Schedin, D. C. Elias, J. A. Jaszczak, and A. K. Geim. Giant intrinsic carrier mobilities in graphene and its bilayer. *Phys. Rev. Lett.*, 100:016602, Jan 2008.

[18] Jian-Hao Chen, Chaun Jang, Shudong Xiao, Masa Ishigami, and Michael S. Fuhrer. Intrinsic and extrinsic performance limits of graphene devices on sio2. *Nat Nano*, 3(4):206–209, Apr 2008.

[19] Alexander A. Balandin, Suchismita Ghosh, Wenzhong Bao, Irene Calizo, Desalegne Teweldebrhan, Feng Miao, and Chun Ning Lau. Superior thermal conductivity of single-layer graphene. *Nano Letters*, 8(3):902–907, 2008. PMID: 18284217.

[20] Changgu Lee, Xiaoding Wei, Jeffrey W. Kysar, and James Hone. Measurement of the elastic properties and intrinsic strength of monolayer graphene. *Science*, 321(5887):385–388, 2008.

[21] Kevin T. Chan, J. B. Neaton, and Marvin L. Cohen. First-principles study of metal adatom adsorption on graphene. *Phys. Rev. B*, 77:235430, Jun 2008.

[22] Patrick Vogt, Paola De Padova, Claudio Quaresima, Jose Avila, Emmanouil Frantzeskakis, Maria Carmen Asensio, Andrea Resta, Bénédicte Ealet, and Guy Le Lay. Silicene: Compelling experimental evidence for graphenelike two-dimensional silicon. *Phys. Rev. Lett.*, 108:155501, Apr 2012.

[23] Boubekeur Lalmi, Hamid Oughaddou, Hanna Enriquez, Abdelkader Kara, Sebastien Vizzini, Benidicte Ealet, and Bernard Aufray. Epitaxial growth of a silicene sheet. *Applied Physics Letters*, 97(22):223109, 2010.

[24] Baojie Feng, Zijing Ding, Sheng Meng, Yugui Yao, Xiaoyue He, Peng Cheng, Lan Chen, and Kehui Wu. Evidence of silicene in honeycomb structures of silicon on ag(111). *Nano Letters*, 12(7):3507–3511, 2012.

[25] Antoine Fleurence, Rainer Friedlein, Taisuke Ozaki, Hiroyuki Kawai, Ying Wang, and Yukiko Yamada-Takamura. Experimental evidence for epitaxial silicene on diboride thin films. *Phys. Rev. Lett.*, 108:245501, Jun 2012.

[26] Lan Chen, Cheng-Cheng Liu, Baojie Feng, Xiaoyue He, Peng Cheng, Zijing Ding, Sheng Meng, Yugui Yao, and Kehui Wu. Evidence for dirac fermions in a honeycomb lattice based on silicon. *Phys. Rev. Lett.*, 109:056804, Aug 2012.

[27] Chun-Liang Lin, Ryuichi Arafune, Kazuaki Kawahara, Mao Kanno, Noriyuki Tsukahara, Emi Minamitani, Yousoo Kim, Maki Kawai, and Noriaki Takagi. Substrate-induced symmetry breaking in silicene. *Phys. Rev. Lett.*, 110:076801, Feb 2013.

[28] Zeyuan Ni, Qihang Liu, Kechao Tang, Jiaxin Zheng, Jing Zhou, Rui Qin, Zhengxiang Gao, Dapeng Yu, and Jing Lu. Tunable bandgap in silicene and germanene. *Nano Letters*, 12(1):113–118, 2012.

[29] Motohiko Ezawa. Valley-polarized metals and quantum anomalous hall effect in silicene. *Phys. Rev. Lett.*, 109:055502, Aug 2012.

[30] Motohiko Ezawa. Photoinduced topological phase transition and a single dirac-cone state in silicene. *Phys. Rev. Lett.*, 110:026603, Jan 2013.

[31] Eduardo V. Castro, N. M. R. Peres, J. M. B. Lopes dos Santos, A. H. Castro Neto, and F. Guinea. Localized states at zigzag edges of bilayer graphene. *Phys. Rev. Lett.*, 100:026802, Jan 2008.

[32] Takahiro Fukui, Yasuhiro Hatsugai, and Hiroshi Suzuki. Chern numbers in discretized brillouin zone: Efficient method of computing (spin) hall conductances. *Journal of the Physical Society of Japan*, 74(6):1674–1677, 2005.

[33] S. Cahangirov, M. Topsakal, E. Aktürk, H. Şahin, and S. Ciraci. Two- and one-dimensional honeycomb structures of silicon and germanium. *Phys. Rev. Lett.*, 102:236804, Jun 2009.

[34] Richard M. Martin. *Electronic Structure: Basic Theory and Practical Methods*. Cambridge University Press, Cambridge, 2004.

[35] J. Kohanoff. *Electronic Structure Calculations for Solids and Molecules*. Cambridge University Press, Cambridge, 2006.

[36] R. G. Parr and G. Yang. *Density Functional Theory of Atoms and Molecules*. Oxford University Press, Oxford, 1989.

[37] P. Hohenberg and W. Kohn. Inhomogeneous Electron Gas. *Phys. Rev.*, 136:B864–B871, Nov 1964.

[38] W. Kohn and L. J. Sham. Self-Consistent Equations Including Exchange and Correlation Effects. *Phys. Rev.*, 140:A1133–A1138, Nov 1965.

[39] R. O. Jones and O. Gunnarsson. The density functional formalism, its applications and prospects. *Rev. Mod. Phys.*, 61:689–746, Jul 1989.

[40] J. P. Perdew and A. Zunger. *Phys. Rev. B*, 23:5048, 1981.

[41] D. M. Ceperley and B. J. Alder. Ground State of the Electron Gas by a Stochastic Method. *Phys. Rev. Lett.*, 45:566–569, Aug 1980.

[42] John P. Perdew, Kieron Burke, and Matthias Ernzerhof. Generalized gradient approximation made simple [phys. rev. lett. 77, 3865 (1996)]. *Phys. Rev. Lett.*, 78:1396–1396, Feb 1997.

[43] James C. Phillips. Energy-Band Interpolation Scheme Based on a Pseudopotential. *Phys. Rev.*, 112:685–695, Nov 1958.

[44] James C. Phillips and Leonard Kleinman. New Method for Calculating Wave Functions in Crystals and Molecules. *Phys. Rev.*, 116:287–294, Oct 1959.

[45] D. R. Hamann, M. Schlüter, and C. Chiang. Norm-Conserving Pseudopotentials. *Phys. Rev. Lett.*, 43:1494–1497, Nov 1979.

[46] N. Troullier and José Luriaas Martins. Efficient pseudopotentials for plane-wave calculations. *Phys. Rev. B*, 43:1993–2006, Jan 1991.

[47] Leonard Kleinman and D. M. Bylander. Efficacious Form for Model Pseudopotentials. *Phys. Rev. Lett.*, 48:1425–1428, May 1982.

[48] P. E. Blöchl. Projector augmented-wave method. *Phys. Rev. B*, 50:17953–17979, Dec 1994.

[49] G. Kresse and D. Joubert. From ultrasoft pseudopotentials to the projector augmented-wave method. *Phys. Rev. B*, 59:1758–1775, Jan 1999.

[50] Georg Kresse, Martijn Marsman, and Jürgen Furthmüller. VASP group. *http://cms.mpi.univie.ac.at/vasp*, 2011.

[51] Paolo Giannozzi, Stefano Baroni, Nicola Bonini, Matteo Calandra, Roberto Car, Carlo Cavazzoni, Davide Ceresoli, Guido L Chiarotti, and Matteo Cococcioni. QUANTUM ESPRESSO: a modular and open-source software project for quantum simulations of materials. *Journal of Physics: Condensed Matter*, 21(39):395502 (19pp), 2009.

[52] Josó M Soler, Emilio Artacho, Julian D Gale, Alberto García, Javier Junquera, Pablo Ordejón, and Daniel Sánchez-Portal. The siesta method for ab initio order- n materials simulation. *Journal of Physics: Condensed Matter*, 14(11):2745, 2002.

[53] B. J. van Wees, H. van Houten, C. W. J. Beenakker, J. G. Williamson, L. P. Kouwenhoven, D. van der Marel, and C. T. Foxon. Quantized conductance of point contacts in a two-dimensional electron gas. *Phys. Rev. Lett.*, 60:848–850, Feb 1988.

[54] J. L. Costa-Krämer, N. García, and H. Olin. Conductance quantization in bismuth nanowires at 4 k. *Phys. Rev. Lett.*, 78:4990–4993, Jun 1997.

[55] Hyoung Joon Choi. *Ph.D. thesis.* Seoul National University, 2000.

[56] R. Landauer. *Philos, Mag.*, 21:863, 1970.

[57] R. Landauer. *J. Phys.: Cond. Mater.*, 1:8099, 1989.

[58] D. S. Fisher and P. A. Lee. *Phys. Rev. B*, 23:6851, 1981.

[59] M. Büttiker, Y. Imry, R. Landauer, and S. Pinhas. *Phys. Rev. B*, 31:6207, 1985.

[60] Young-Woo Son. *Ph.D. thesis.* Seoul National University, 2004.

[61] C. L. Kane and E. J. Mele. Quantum spin hall effect in graphene. *Phys. Rev. Lett.*, 95:226801, Nov 2005.

[62] Yugui Yao, Leonard Kleinman, A. H. MacDonald, Jairo Sinova, T. Jungwirth, Ding-sheng Wang, Enge Wang, and Qian Niu. First principles calculation of anomalous hall conductivity in ferromagnetic bcc fe. *Phys. Rev. Lett.*, 92:037204, Jan 2004.

[63] Ryuichi Shindou and Ken-Ichiro Imura. Noncommutative geometry and non-abelian berry phase in the wave-packet dynamics of bloch electrons. *Nuclear Physics B*, 720(3):399 – 435, 2005.

[64] S. Datta. *Electronic Transport in Mesoscopic Systems*. Cambridge University Press, Cambridge, 1997.

[65] Shousuke Nakanishi and Masaru Tsukada. Quantum loop current in a C_{60} molecular bridge. *Phys. Rev. Lett.*, 87:126801, Aug 2001.

[66] Hong Liu. Induced magnetic moment in defected single-walled carbon nanotubes. *Nanotechnology*, 16(12):3001, 2005.

[67] Yi Liu and Hong Guo. Current distribution in b- and n-doped carbon nanotubes. *Phys. Rev. B*, 69:115401, Mar 2004.

[68] Jie-Yun Yan, Ping Zhang, Bo Sun, Hai-Zhou Lu, Zhigang Wang, Suqing Duan, and Xian-Geng Zhao. Quantum blockade and loop current induced by a single lattice defect in graphene nanoribbons. *Phys. Rev. B*, 79:115403, Mar 2009.

[69] Yanyang Zhang, Jiang-Ping Hu, B. A. Bernevig, X. R. Wang, X. C. Xie, and W. M. Liu. Quantum blockade and loop currents in graphene with topological defects. *Phys. Rev. B*, 78:155413, Oct 2008.

[70] N. Troullier and José Luriaas Martins. Efficient pseudopotentials for plane-wave calculations. *Phys. Rev. B*, 43:1993–2006, Jan 1991.

[71] Leonard Kleinman and D. M. Bylander. Efficacious form for model pseudopotentials. *Phys. Rev. Lett.*, 48:1425–1428, May 1982.

[72] Javier Junquera, Óscar Paz, Daniel Sánchez-Portal, and Emilio Artacho. Numerical atomic orbitals for linear-scaling calculations. *Phys. Rev. B*, 64:235111, Nov 2001.

[73] Hajime Matsumura and Tsuneya Ando. Conductance of carbon nanotubes with a stone–wales defect. *Journal of the Physical Society of Japan*, 70(9):2657–2665, 2001.

[74] Hua-Tong Yang, Linfeng Yang, Jiangwei Chen, and Jinming Dong. Antiresonance effect due to stone–wales defect in carbon nanotubes. *Physics Letters A*, 325:287 – 293, 2004.

[75] Hyoung Joon Choi, Jisoon Ihm, Steven G. Louie, and Marvin L. Cohen. Defects, quasibound states, and quantum conductance in metallic carbon nanotubes. *Phys. Rev. Lett.*, 84:2917–2920, Mar 2000.

[76] Changsheng Li, Langhui Wan, Yadong Wei, and Jian Wang. Definition of current density in the presence of a non-local potential. *Nanotechnology*, 19(15):155401, 2008.

[77] P. A. Orellana, F. Domínguez-Adame, I. Gómez, and M. L. Ladrón de Guevara. Transport through a quantum wire with a side quantum-dot array. *Phys. Rev. B*, 67:085321, Feb 2003.

[78] X. R. Wang, Yupeng Wang, and Z. Z. Sun. Antiresonance scattering at defect levels in the quantum conductance of a one-dimensional system. *Phys. Rev. B*, 65:193402, Apr 2002.

[79] G. Breit and E. Wigner. Capture of slow neutrons. *Phys. Rev.*, 49:519–531, Apr 1936.

[80] Tooru Taniguchi and Markus Büttiker. Friedel phases and phases of transmission amplitudes in quantum scattering systems. *Phys. Rev. B*, 60:13814–13823, Nov 1999.

[81] H.-W. Lee. Generic transmission zeros and in-phase resonances in time-reversal symmetric single channel transport. *Phys. Rev. Lett.*, 82:2358–2361, Mar 1999.

[82] Christian Degen. Nanoscale magnetometry: Microscopy with single spins. *Nat Nano*, 3(11):643–644, Nov 2008.

[83] Martin E. Huber, Nicholas C. Koshnick, Hendrik Bluhm, Leonard J. Archuleta, Tommy Azua, Per G. Bjornsson, Brian W. Gardner, Sean T. Halloran, Erik A. Lucero, and Kathryn A. Moler. Gradiometric micro-squid susceptometer for scanning measurements of mesoscopic samples. *Review of Scientific Instruments*, 79(5):053704, 2008.

[84] L. Hao, J. C. Macfarlane, J. C. Gallop, D. Cox, J. Beyer, D. Drung, and T. Schurig. Measurement and noise performance of nano-superconducting-quantum-interference devices fabricated by focused ion beam. *Applied Physics Letters*, 92(19):192507, 2008.

[85] D. Rugar, R. Budakian, H. J. Mamin, and B. W. Chui. Single spin detection by magnetic resonance force microscopy. *Nature*, 430(6997):329–332, July 2004.

[86] J. R. Maze, P. L. Stanwix, J. S. Hodges, S. Hong, J. M. Taylor, P. Cappellaro, L. Jiang, M. V. Gurudev Dutt, E. Togan, A. S. Zibrov, A. Yacoby, R. L. Walsworth, and M. D. Lukin. Nanoscale magnetic sensing with an individual electronic spin in diamond. *Nature*, 455(7213):644–647, Oct 2008.

[87] P. O. Lehtinen, A. S. Foster, A. Ayuela, A. Krasheninnikov, K. Nordlund, and R. M. Nieminen. Magnetic properties and diffusion of adatoms on a graphene sheet. *Phys. Rev. Lett.*, 91:017202, Jun 2003.

[88] Xinran Wang, Xiaolin Li, Li Zhang, Youngki Yoon, Peter K. Weber, Hailiang Wang, Jing Guo, and Hongjie Dai. N-doping of graphene through electrothermal reactions with ammonia. *Science*, 324(5928):768–771, 2009.

[89] C. Coletti, C. Riedl, D. S. Lee, B. Krauss, L. Patthey, K. von Klitzing, J. H. Smet, and U. Starke. Charge neutrality and band-gap tuning of epitaxial graphene on sic by molecular doping. *Phys. Rev. B*, 81:235401, Jun 2010.

[90] Owen C. Compton and SonBinh T. Nguyen. Graphene oxide, highly reduced graphene oxide, and graphene: Versatile building blocks for carbon-based materials. *Small*, 6(6):711–723, 2010.

[91] T. O. Wehling, K. S. Novoselov, S. V. Morozov, E. E. Vdovin, M. I. Katsnelson, A. K. Geim, and A. I. Lichtenstein. Molecular doping of graphene. *Nano Letters*, 8(1):173–177, 2008. PMID: 18085811.

[92] Hongtao Liu, Yunqi Liu, and Daoben Zhu. Chemical doping of graphene. *J. Mater. Chem.*, 21:3335–3345, 2011.

[93] F. Schedin, A. K. Geim, S. V. Morozov, E. W. Hill, P. Blake, M. I. Katsnelson, and K. S. Novoselov. Detection of individual gas molecules adsorbed on graphene. *Nat Mater*, 6(9):652–655, Sep 2007.

[94] D W Boukhvalov and M I Katsnelson. Chemical functionalization of graphene. *Journal of Physics: Condensed Matter*, 21(34):344205, 2009.

[95] S. Gowtham, Ralph H. Scheicher, Rajeev Ahuja, Ravindra Pandey, and Shashi P. Karna. Physisorption of nucleobases on graphene: Density-functional calculations. *Phys. Rev. B*, 76:033401, Jul 2007.

[96] O Lehtinen, J Kotakoski, A V Krasheninnikov, and J Keinonen. Cutting and controlled modification of graphene with ion beams. *Nanotechnology*, 22(17):175306, 2011.

[97] A. V. Krasheninnikov and F. Banhart. Engineering of nanostructured carbon materials with electron or ion beams. *Nat Mater*, 6(10):723–733, Oct 2007.

[98] Florian Banhart, Jani Kotakoski, and Arkady V. Krasheninnikov. Structural defects in graphene. *ACS Nano*, 5(1):26–41, Nov 2010.

[99] Ayako Hashimoto, Kazu Suenaga, Alexandre Gloter, Koki Urita, and Sumio Iijima. Direct evidence for atomic defects in graphene layers. *Nature*, 430(7002):870–873, Aug 2004.

[100] Ovidiu Cretu, Arkady V. Krasheninnikov, Julio A. Rodríguez-Manzo, Litao Sun, Risto M. Nieminen, and Florian Banhart. Migration and localization of metal atoms on strained graphene. *Phys. Rev. Lett.*, 105:196102, Nov 2010.

[101] Mineo Saito, Kazuaki Yamashita, and Tatsuki Oda. Magic numbers of graphene multivacancies. *Japanese Journal of Applied Physics*, 46(47):L1185–L1187, 2007.

[102] Gun-Do Lee, C. Z. Wang, Euijoon Yoon, Nong-Moon Hwang, Doh-Yeon Kim, and K. M. Ho. Diffusion, coalescence, and reconstruction of vacancy defects in graphene layers. *Phys. Rev. Lett.*, 95:205501, Nov 2005.

[103] A.V. Krasheninnikov, P.O. Lehtinen, A.S. Foster, and R.M. Nieminen. Bending the rules: Contrasting vacancy energetics and migration in graphite and carbon nanotubes. *Chemical Physics Letters*, 418(1 - 3):132 – 136, 2006.

[104] J. Kotakoski, A. V. Krasheninnikov, U. Kaiser, and J. C. Meyer. From point defects in graphene to two-dimensional amorphous carbon. *Phys. Rev. Lett.*, 106:105505, Mar 2011.

[105] G. Kresse and J. Furthmüller. Efficiency of ab-initio total energy calculations for metals and semiconductors using a plane-wave basis set. *Computational Materials Science*, 6(1):15 – 50, 1996.

[106] P. E. Blöchl. Projector augmented-wave method. *Phys. Rev. B*, 50:17953–17979, Dec 1994.

[107] Brian W. Smith and David E. Luzzi. Electron irradiation effects in single wall carbon nanotubes. *Journal of Applied Physics*, 90(7):3509–3515, 2001.

[108] Cristina Goómez-Navarro, Jannik C. Meyer, Ravi S. Sundaram, Andrey Chuvilin, Simon Kurasch, Marko Burghard, Klaus Kern, and Ute Kaiser.

Atomic structure of reduced graphene oxide. *Nano Letters*, 10(4):1144–1148, 2010. PMID: 20199057.

[109] Gun-Do Lee, C. Z. Wang, Euijoon Yoon, Nong-Moon Hwang, and K. M. Ho. Reconstruction and evaporation at graphene nanoribbon edges. *Phys. Rev. B*, 81:195419, May 2010.

[110] N. D. Drummond, V. Zólyomi, and V. I. Fal'ko. Electrically tunable band gap in silicene. *Phys. Rev. B*, 85:075423, Feb 2012.

[111] Abdelkader Kara, Hanna Enriquez, Ari P. Seitsonen, L.C. Lew Yan Voon, Sébastien Vizzini, Bernard Aufray, and Hamid Oughaddou. A review on silicene - new candidate for electronics. *Surface Science Reports*, 67(1):1 – 18, 2012.

[112] Paola De Padova, Osamu Kubo, Bruno Olivieri, Claudio Quaresima, Tomonobu Nakayama, Masakazu Aono, and Guy Le Lay. Multilayer silicene nanoribbons. *Nano Letters*, 12(11):5500–5503, 2012.

[113] B. Andrei Bernevig, Taylor L. Hughes, and Shou-Cheng Zhang. Quantum spin hall effect and topological phase transition in hgte quantum wells. *Science*, 314(5806):1757–1761, 2006.

[114] Cheng-Cheng Liu, Wanxiang Feng, and Yugui Yao. Quantum spin hall effect in silicene and two-dimensional germanium. *Phys. Rev. Lett.*, 107:076802, Aug 2011.

[115] Di Xiao, Wang Yao, and Qian Niu. Valley-contrasting physics in graphene: Magnetic moment and topological transport. *Phys. Rev. Lett.*, 99:236809, Dec 2007.

[116] Fan Zhang, Jeil Jung, Gregory A. Fiete, Qian Niu, and Allan H. MacDonald. Spontaneous quantum hall states in chirally stacked few-layer graphene systems. *Phys. Rev. Lett.*, 106:156801, Apr 2011.

[117] Wang Yao, Shengyuan A. Yang, and Qian Niu. Edge states in graphene: From gapped flat-band to gapless chiral modes. *Phys. Rev. Lett.*, 102:096801, Mar 2009.

[118] Wang Yao, Di Xiao, and Qian Niu. Valley-dependent optoelectronics from inversion symmetry breaking. *Phys. Rev. B*, 77:235406, Jun 2008.

[119] Motohiko Ezawa. A topological insulator and helical zero mode in silicene under an inhomogeneous electric field. *New Journal of Physics*, 14(3):033003, 2012.

[120] Motohiko Ezawa. Spin-valley optical selection rule and strong circular dichroism in silicene. *Phys. Rev. B*, 86:161407, Oct 2012.

[121] M. Tahir and U. Schwingenschlögl. Valley polarized quantum hall effect and topological insulator phase transitions in silicene. *Sci. Rep.*, 3, Jan 2013.

[122] A. R. Wright, 2012.

[123] Xiao Li, Zhenhua Qiao, Jeil Jung, and Qian Niu. Unbalanced edge modes and topological phase transition in gated trilayer graphene. *Phys. Rev. B*, 85:201404, May 2012.

[124] Jian Li, Ivar Martin, Markus Buttiker, and Alberto F. Morpurgo. Topological origin of subgap conductance in insulating bilayer graphene. *Nat Phys*, 7(1):38–42, Jan 2011.

[125] Ivar Martin, Ya. M. Blanter, and A. F. Morpurgo. Topological confinement in bilayer graphene. *Phys. Rev. Lett.*, 100:036804, Jan 2008.

[126] G. W. Semenoff, V. Semenoff, and Fei Zhou. Domain walls in gapped graphene. *Phys. Rev. Lett.*, 101:087204, Aug 2008.

[127] Jeil Jung, Fan Zhang, Zhenhua Qiao, and Allan H. MacDonald. Valley-hall kink and edge states in multilayer graphene. *Phys. Rev. B*, 84:075418, Aug 2011.

[128] Zhenhua Qiao, Jeil Jung, Qian Niu, and Allan H. MacDonald. Electronic highways in bilayer graphene. *Nano Letters*, 11(8):3453–3459, 2011.

[129] Jeil Jung, Zhenhua Qiao, Qian Niu, and Allan H. MacDonald. Transport properties of graphene nanoroads in boron nitride sheets. *Nano Letters*, 12(6):2936–2940, 2012.

[130] Abolhassan Vaezi, Yufeng Liang, Darryl H. Ngai, Li Yang, and Eun-Ah Kim. Topological kink states at a tilt boundary in gated multi-layer graphene, 2013.

[131] Fan Zhang, A. H. MacDonald, and E. J. Mele. Valley chern numbers and boundary modes in gapped bilayer graphene, 2013.

[132] Jian Li, Ivar Martin, Markus Büttiker, and Alberto F Morpurgo. Marginal topological properties of graphene: a comparison with topological insulators. *Physica Scripta*, 2012(T146):014021, 2012.

[133] W. P. Su, J. R. Schrieffer, and A. J. Heeger. Solitons in polyacetylene. *Phys. Rev. Lett.*, 42:1698–1701, Jun 1979.

[134] G. Kresse and J. Furthmüller. Efficient iterative schemes for *ab initio* total-energy calculations using a plane-wave basis set. *Phys. Rev. B*, 54:11169–11186, Oct 1996.

[135] D. M. Ceperley and B. J. Alder. Ground state of the electron gas by a stochastic method. *Phys. Rev. Lett.*, 45:566–569, Aug 1980.

[136] D.-B. Zhang, E. Akatyeva, and T. Dumitrică. Bending ultrathin graphene at the margins of continuum mechanics. *Phys. Rev. Lett.*, 106:255503, Jun 2011.

[137] Grigory E. Volovik. *The Universe in a Helium Droplet.* Oxford University Press, USA, 2003.

[138] D. Gunlycke and C. T. White. Graphene valley filter using a line defect. *Phys. Rev. Lett.*, 106:136806, Mar 2011.

국문초록

지난 십 년 동안 우리는 탄소나노튜브나 그래핀 같은 벌집격자구조계에 대한 전기적 성질을 이해에 있어 큰 발전을 목격해왔다. 이러한 물질을 이해하고 실질적인 장치로의 응용을 위한 엄청난 노력을 기울여온 터다. 그러한 노력을 통해 이제는 탄소나노튜브나 그래핀이 미래의 전자 기술을 위해 가장 중요한 물질로 손꼽히고 있는 상황이다. 그간의 연구 성과를 고려해볼 때, 이러한 시스템들이 여전히 새로운 현상을 드러냄으로써 계속해서 우리의 이목을 집중시키고 있다는 사실은 놀라운 일이다. 특히, 이러한 시스템에 결정 결함이 포함된 경우 좀 더 흥미로운 특징을 드러낸다. 이들 물성은 결함이 존재함에 의해 심각하게 바뀔 수 있고, 그 결과로 결함이 없는 시스템에서는 예상하지 못한 새로운 현상을 기대할 수 있는 것이다. 이것은 다양한 물리적 현상의 발현을 위한 새로운 기회를 제공하고, 이러한 시스템의 응용의 범위를 확장하는 결과를 가져올 수 있다. 본 학위논문에서는 탄소나노튜브, 그래핀, 그리고 실리신을 아우르는 벌집격자구조계 내의 결함으로 유도되는 전자구조와 전기적 성질에 대한 제일원리연구와 분석을 제시한다.

첫째로, 우리는 간단하게 그래핀과 실리신의 기본적인 전기적 성질과 이 연구에서 사용한 컴퓨터를 이용한 계산 방법에 대한 짧을 리뷰를 한 후, 스톤-웰스 결함을 포함한 금속성 탄소나노튜브의 전자수송특성을 살펴볼 것이다. 산란-상태 접근법 [1]을 기반으로 한 제일원리 전자수송 계산 방법을 이용해 우리는 스톤-웰스 결함을

집어 넣음으로써 에돌이 전류가 발생할 수 있음을 보인다. 에돌이 전하의 에너지에 따른 행동특성에 대해 조사를 통해 (1) 에돌이 전류의 세기가 전기전도도가 1.5 페르미 에너지에서 최고치를 갖는 다는 점, (2) 에돌이 전류의 세기가 전기전도도가 1.0 G_0가 되는 페르미 에너지에서 완전히 소멸한다는 점, 그리고 (3) 에돌이 전류의 방향이 페르미 에너지가 전기전도도 최저점을 지나면서 바뀐다는 점을 보인다. 이런 새로운 발견의 원인에 대한 토의를 통해 이것이 하나의 전도 채널과 결함 상태의 간섭에 의한 일반 적인 현상임을 밝힌다. 우리는 또한 유도 자기장을 계산함으로써 이러한 현상의 실험적 표징에 대해서도 고려한다. 우리는 시간에 따라 변하는 게이트 전압을 통해 시간적으로 진동하는 쌍극자 자기장을 유도할 수 있을 것으로 예상한다.

다음으로 우리는 쌍격자 빈자리를 포함한 그래핀의 전자구조가 원자 구조에 미치는 영향을 고려한다. 쌍격자 빈자리는 세 개의 오각형-세 개의 7각형, 혹은 오각형-팔각형-오각형과 같은 다양한 형태의 재건된 원자 구조를 가지는 것으로 알려진 그래핀에서 가장 흔하게 관찰되는 결함이다. 참고 문헌 [2]에 개재된 투과 전자 현미경 사진으로부터 우리는 이 쌍격자 빈자리가 80 keV의 전자 빔으로부터 운동에너지를 받아 하나의 재건 구조로부터 다른 재건 구조로 바뀌는 현상을 발견했다. 이러한 발견을 동기로 우리는 범밀도함수를 기반으로 격자 빈자리를 포함한 그래핀의 전자구조계산을 수행했다. 우리의 계산에 따르면 하나의 구조에서 다른 구조로 구조변환을 하는데 필요한 에너지가 전자 빔으로부터 받을 수 있는 에너지의 최댓값보다 작다. 또한 구조 변환의 미시적인 과정이 일렬의 스톤-웰즈 변환의 시리즈로 구성된 경우가 에너지적으로 선호된다.우리 결과에 따르면, 오각형-칠각형-칠각형-오각형 재건 구조가 구조 변환 중간의 구조로 나와 구조 변환에 필요한 에너지를 낮추는 역할을 할 것으로 예상된다.

마지막으로, 우리는 선형 결함을 가진 실리신을 고려한다. 실리신은 실리콘으로

만든 이차원 벌집격자구조이다. 그래핀과 다르게 평면 구조의 실리신은 불안정하고, 이러한 불안정성은 좌굴을 통해 해소된다. 이러한 좌굴은 시리신 평면에 대한 반사대칭을 자발적으로 깬다. 이러한 자발적 대칭성 붕괴 때문에 실리신의 바닥 상태 원자 구조는 이중으로 축퇴된다. 본 졸업논문의 마지막 주제는 이러한 축퇴된 바닥 원자 상태 사이를 잇는 인터페이스 구조의 전자구조 고려한다. 이러한 인터페이스 구조에 수직 전기장을 걸 경우 위상학적으로 보호된 제로 모드를 발현함을 보인다. 베리 곡률과 벨리에 국한된 홀 전기 전도성 계산을 통해 이러한 제로 모드의 위상학적 근원에 대해 토의한다. 또한 제일원리계산을 통해 얻은 모의 주사현미경실험을 바탕으로 이러한 제로 모드의 발현을 측정할 만한 실험에 대해서 토의한다. 우리의 결과가 실리신에서 위상학적인 현상을 관찰하는데 도움이 될 것으로 예상한다.

주요어 : 범밀도함수이론, 탄소나노튜브, 그래핀, 실리신, 에돌이전류, 자기 쌍극자, 전하수송, 스톤-웰스 결함, 양자 간섭, 쌍격자 빈자리, 구조 변환, 스톤-웰즈 변환, 투과 전자 현미경, 양자 벨리 홀 효과, 솔리톤, 위상학적 구역벽 제로 모드, 주사현미경

학번 : 2006-22901

감사의 글

무엇보다 바쁘신 와중에도 제 학위 논문의 부족한 부분을 세밀하게 지적해 주신 유재준 심사의원장님, 최석봉 심사의원님, 유병덕 심사의원님, 박철환 심사의원님께 감사 드립니다. 세계 최고 수준의 교육환경을 만들기 위해 항상 노력해주시는 서울대학교 물리학과의 모든 교수님께도 진심으로 감사 드립니다.

지난 7년간 물심 양면으로 지원해주시고 지도와 편달을 아끼지 않아주셨던 임지순 선생님께 머리 숙여 깊이 감사 드립니다. 선생님의 풍부하고 다양한 연구 선험과 선견 덕분에 한 없이 부족한 제가 학위 과정을 마칠 수 있었습니다. 어리석은 저를 인내로 이끌어 주셔서 감사합니다. 매 그룹미팅 시간 마다 날카로운 질문으로 물리적으로 생각하는 방법을 알려주신 유재준 선생님께도 고개 숙여 깊은 감사의 뜻 전합니다. 선생님의 폭넓은 물리학 지식과 학문적 태도에 깊은 감명 받았습니다. 최형준 교수님께도 잊지 못할 많은 것들을 배웠습니다. 연세대에 오가며 최형준 교수님으로부터 듣고 배운 것들이 지금까지도 큰 도움이 되고 있습니다. 감사합니다. 첫 논문이 나오기까지 많은 지도 편달 아끼지 않아주신 이건도 교수님께 깊은 감사 드립니다. 항상 밝은 표정으로 이야기 많이 해주신 박철환 교수님께도 감사의 말씀 전하고 싶습니다. 학부 때부터 오랜 시간 관심 가져주시고, 지도 편달을 잊지 않아주신 이준규 교수님께도 이 자리를 빌어 깊은 감사의 말씀 전하고 싶습니다. 연구실 후배란 이유로 학회나 해외에서 친절하게 챙겨주신 연구실 모든 졸업생 선

배님들께도 모두 감사 드립니다.

학위 과정을 통틀어 선배님들과 후배님들, 동기님들에게도 많은 도움을 받았습니다. 항상 진지한 자세로 열심히 토론해주신 진호섭 선배님, 어깨 넘어 학문하는 자세란 이런 것이다 알려주신 이훈경 선배님, 항상 성실하고 유쾌하셨던 최운이 선배님, 늘 밝은 표정으로 맞아주신 정병욱 박사님, 열정적인 자세로 성실히 연구하신 김승철 선배님, 여러모로 많은 힘이 되어 주시고 계시는 이준희 선배님, 프로그램 쓰는 방법을 가장 많이 알려주고, 연구실에 처음 들어와 지금까지도 계속 큰 도움을 주고 계시는 학부 동기 임진오 선배님, 명확한 개념으로 늘 좋은 토론 상대가 되어준 학부 동기 박창원 선배님, 힘든 외국 생활에도 항상 즐겁게 토론하고 연구해준 쿠옹 선배님, 연구실 생활에 큰 도움이 돼 준 차문현 선배님, 컴퓨터 관리하며 도움을 주신 정호균 선배님, 힘든 여건에서도 늘 진지한 학문적 태도를 유지하시며 큰 귀감이 되어주시는 박재현 선배님, 특유의 친화력으로 늘 좋은 연구실 분위기를 조성해주신 김지연 선배님, 운동, 연구, 생활 전반에 걸쳐 아직까지도 많은 도움 주고 계시는 김충현 선배님, 항상 편안하게 질문 받아주는 김흥식 선배님께도 고개 숙여 깊이 감사 드립니다. 함께 운동도하고, 밥먹고, 연구하며 연구실 생활을 아름답게 장식해준 연구실 식구들, 근수형, 남욱이형, 철이, 록연이, 재현이, 예리, 민성, 정운, 동욱 후배님들께도 깊은 감사 드립니다. 덕분에 연구실 생활 즐거웠습니다. 함께 식사하며 즐겁게 이야기 나누던 종현이, 진영이, 승욱이, 102후배님들에게도 고맙단 말 전하고 싶습니다. 열정과 인내와 노력의 높은 경지를 몸소 보여줬던 나의 학부 동기들, 선배님들, 후배님들 여러분들이 보여준 높은 스탠더드가 늘 제 인내의 원천이 되고 있습니다. 감사합니다.

힘든 상황에도 불구하고 바르게 키워주시고 사랑해주신 어머니, 가족 위해 큰 희생하신 아버지, 굳건하게 지탱해준 형님께 제가 드릴 수 있는 가장 큰 감사의 마음 전합니다. 감사합니다.